



VCU

Virginia Commonwealth University
VCU Scholars Compass

Theses and Dissertations

Graduate School

2022

DNA CONDENSATION STATE REGULATES NUCLEAR LAMINA STRAIN AND CELLULAR ADAPTATION TO PHYSIOLOGICAL FORCES

Brooke E. Danielsson

Follow this and additional works at: <https://scholarscompass.vcu.edu/etd>



Part of the [Molecular, Cellular, and Tissue Engineering Commons](#)

© The Author

Downloaded from

<https://scholarscompass.vcu.edu/etd/6881>

This Dissertation is brought to you for free and open access by the Graduate School at VCU Scholars Compass. It has been accepted for inclusion in Theses and Dissertations by an authorized administrator of VCU Scholars Compass. For more information, please contact libcompass@vcu.edu.

© Brooke Danielsson 2022
All Rights Reserved

DNA CONDENSATION STATE REGULATES NUCLEAR LAMINA STRAIN AND
CELLULAR ADAPTATION TO PHYSIOLOGICAL FORCES

A dissertation submitted in partial fulfillment of the requirement for the degree of Doctor of
Philosophy in Biomedical Engineering at Virginia Commonwealth University.

By

Brooke Danielsson
B.S., New York Institute of Technology, 2016

Director: Daniel Conway, Ph.D.
Associate Professor, Biomedical Engineering

Virginia Commonwealth University
Richmond, Virginia
March 29, 2022

*To James: my husband and greatest friend
Thank you for your endless support and constant encouragement through this adventure and
always.*

ACKNOWLEDGMENTS

The completion of my PhD could not have been possible without the help and support of several people who I wish to acknowledge.

To Dr. Daniel Conway—PhD Thesis Advisor

I am forever grateful to have you as my mentor and friend. Thank you for always allowing me to be myself, and for helping me grow into a better scientist and person. You are the best teacher I have ever had. I hope you know how much I appreciate all you have done to guide me, both in my career and in life.

To Dr. Kris Dahl—PhD Thesis Committee Member

Thank you for all the time you have spent mentoring me on my projects and career. I greatly admire your perspective and wisdom. Every meeting with you is a fun one and I always learn something new. I hope to be as smart and cool as you one day.

To Dr. Teemu Ihalainen—PhD Thesis Committee Member

I have really enjoyed working together on the lamin sensor project the last two years. You are one of the nicest people I have met in academia and have very clever ideas. Thank you for the support and kindness you have shown me. I hope to work on more projects together in the future.

To Dr. Rebecca Heise—PhD Thesis Committee Member

Thank you for your mentorship and for always being there whenever I need to talk. I am so grateful for your support and encouragement both personally and academically.

To Dr. Andrew Stephens—PhD Thesis Committee Member

Thank you for sharing your knowledge and providing me guidance on my projects. Your feedback makes me think harder and grow as a scientist.

To Dr. Christopher Lemmon—PhD Thesis Committee Member

If it were not for our first meeting on October 19, 2017, I am not sure where I would be right now. You convinced me to attend VCU, get a PhD, and reach out to a mentor you thought I would be a perfect fit for (Dr. Conway). I think back to that day a lot and appreciate all your encouragement, support, and positivity.

To Conway Lab Members

I could not have asked for a better working environment. I have met lifelong friends during my time in Conway Lab. Thank you to all the Conway Lab members, both past and present, for the support, experimental and technical help, and thoughtful discussions. I will always remember all the fun times we have had together both in and outside of the lab.

To Hannah Peters—Conway Lab Undergrad Research Assistant

Thank you for all your hard work and assistance for 3 years. I hope I taught you as much as you taught me. I am so proud of what you have achieved and know you will make an amazing medical doctor. Also, thank you for all your support outside of the lab—my entire family loves you so much!

To Jolene Cabe—Conway Lab Manager and Friend

I think I can speak on behalf of all Conway Lab members in saying we are beyond fortunate to have you. Thank you for making the lab run smoothly and your immense help with experiments. You have become a great friend and I will miss you.

To Katie Tieu—Conway Lab PhD Student and Friend

If I were to write down everything you have done for me throughout the last 4 years it would exceed the page limits. So, in summary, I am extremely thankful for you and know that my PhD experience would have been 100x harder without you. I am not sure what I am going to do without you, so maybe you should join me at Yale?

To Tracy Tarlton—Mom

Thank you for showing me, by your example, the definition of hard work. I cannot thank you enough for all the help you have provided so that I could pursue my career while also being a mom. James, James Patrick, and I are beyond blessed to have you.

To James Danielsson—Husband and Baby-daddy

Thank you for showing me so much patience, love, and support every day. You have been my rock and #1 supporter since the day I met you almost 10 years ago. Thank you for all the late nights and weekends you have spent in lab with me so that I could work and we could still be together. You are the most incredible husband and dad, and I could not have done it without you. I love you beyond words.

The work presented in this dissertation was supported in part by the National Science Foundation's Graduate Research Fellowship (to B.D.), National Science Foundation CAREER award CMMI 1653299 (to D.C.), and National Institute of Health R35 GM119617 (to D.C.). Microscopy was performed at VCU's Nanomaterials Characterization Core, as well as VCU's Microscopy Facility, supported, in part, by funding from NIH-NCI Cancer Center Support Grant P30 CA016059. I would like to acknowledge the assistance from Dr. Carl Mayer from the Nanomaterials Characterization Core at Virginia Commonwealth University. I would also like to acknowledge the Koerner Family Foundation for providing me with \$10,000 in stipend support.

TABLE OF CONTENTS

ACKNOWLEDGMENTS	3
LIST OF FIGURES	8
GLOSSARY	11
ABSTRACT	13
CHAPTER 1: INTRODUCTION.....	16
CHAPTER 2: BACKGROUND.....	19
CHAPTER 3: LAMIN MICROAGGREGATES LEAD TO ALTERED MECHANOTRANSMISSION IN PROGERIN-EXPRESSING CELLS	28
3.1. RATIONALE	28
3.2. METHODS.....	30
3.3. RESULTS.....	32
3.4. DISCUSSION.....	45
CHAPTER 4: PROGERIN-EXPRESSING ENDOTHELIAL CELLS ARE UNABLE TO ADAPT TO SHEAR STRESS	50
4.1. RATIONALE	50
4.2. METHODS.....	52
4.3. RESULTS.....	55
4.4. DISCUSSION.....	68
CHAPTER 5: CHROMATIN CONDENSATION REGULATES ENDOTHELIAL CELL ADAPTATION TO SHEAR STRESS.....	72
5.1. RATIONALE	72
5.2. METHODS.....	74
5.3. RESULTS.....	79
5.4. DISCUSSION.....	93
CHAPTER 6: NUCLEAR LAMINA STRAIN STATES REVEALED BY INTERMOLECULAR FORCE BIOSENSOR	98
6.1. RATIONALE	98
6.2. METHODS.....	99
6.3. RESULTS.....	108
CHAPTER 7: CONCLUSIONS.....	128
REFERENCES	131

LIST OF FIGURES

Figure 1: The structure of the eukaryotic nucleus	22
Figure 2: Post-translational modification to lamin A processing	25
Figure 3: Traditional force sensor design	26
Figure 4: Punctate inclusions in progerin-expressing nuclei.....	33
Figure 5: Western blot of lamin A/C overexpression and HA-progerin expression	34
Figure 6: Comparison of actin fiber organization of HGPS patient cells and HA-Progerin model system	34
Figure 7: Punctate inclusions in progerin patient fibroblast nuclei	35
Figure 8: Strain on an inclusion of increased stiffness causes a line of increased stress normal to the imposed strain.....	36
Figure 9: Simulations for measuring peak midline stress as a function of inclusion size	37
Figure 10: Confocal fluorescence microscopy confocal sections for cells patterned on lines	38
Figure 11: Methodology of measuring the angle and length of wrinkles.....	40
Figure 12: Formation of wrinkles for cells under one-dimensional confinement	41
Figure 13: Wrinkle comparison on 40 μm stripes versus 20 μm stripes	42
Figure 14: HGPS patient fibroblasts do not align under uniaxial stretch.....	44
Figure 15: Model of nuclear lamina under force	48
Figure 16: Progerin expression causes cell loss in HUVECs under laminar shear stress	58
Figure 17: Laminar shear stress causes nuclear envelope disruption in Progerin-expressing HUVECs.....	61
Figure 18: Lonafarnib rescues cell loss and nuclear envelope disruptions in progerin-expressing HUVECs under shear stress	64

Figure 19: Methylstat reduces cell loss in Progerin-expressing HUVECs and ZMPSTE24 KD cells under shear stress.	66
Figure 20: Prealignment of Progerin-Expressing HUVECS prevents cell loss under shear stress	67
Figure 21: Epigenetic Modifications in Response to Fluid Shear Stress in vitro.....	82
Figure 22: Epigenetic Modifications in Response to Fluid Shear Stress in vivo.	85
Figure 23: Chromatin decondensation increases the rate of EC alignment to shear stress.	88
Figure 24: VEGF treatment increases chromatin decondensation and increases the rate of EC alignment to shear stress.....	90
Figure 25: Changes in chromatin condensation affect shear stress induced DNA damage	93
Figure 26: Development and characterization of the FRET based lamin A/C strain sensor.....	110
Figure 27: Fluorescence recovery after photobleaching (FRAP) experiments of Lamin-SS and Lamin-SS-T binding to nuclear lamina	112
Figure 28: Schematic representation of the simulated FRAP experiment and reactions	114
Figure 29: Lamin-SS, Lamin-histone-SS and Lamin-histone-SS-T sensor distribution and apparent FRET efficiency in LMNA KO cells.....	116
Figure 30: Effect of hyper-osmotic conditions on nuclear morphology and volume.....	117
Figure 31: Development and characterization of the FRET based lamin A/C - histone H2A strain sensor	119
Figure 32: The effect of cellular force transduction and chromatin organization on lamin A/C strain	121
Figure 33: The effect of actin cytoskeleton disruption on Lamin-SS FRET	123
Figure 34: Nuclear lamina organization after chromatin relaxation.....	124

Figure 35: Fluorescence recovery after photobleaching (FRAP) experiments of Lamin-SS after
TSA treatment125

Figure 36: Nuclear lamina organization after chromatin condensation126

GLOSSARY

Key Words

Nucleus, Mechanobiology, Nuclear lamina, Chromatin condensation, Hutchinson Gilford Progeria Syndrome, Fluid shear stress, Progerin, Biosensors, FRET

Abbreviations

EC	Endothelial Cells
HUVEC	Human Umbilical Vein Endothelial Cells
vSMCs	Vascular Smooth Muscle Cells
MDCK	Madin-Darby Canine Kidney Cells
MSC	Mesenchymal Stem Cells
KD	Knockdown
Lamin OE	Lamin A Over- Expression
LA	Lamin A
LA/C	Lamin A/C
HGPS	Hutchinson-Gilford Progeria Syndrome
DN-KASH	Dominant Negative Nesprin KASH
LINC	Linker of Nucleoskeleton and Cytoskeleton
TSmold	Tension Sensor Module
PDMS	Polydimethylsiloxane
PBS	Phosphate Buffered Solution
FSS	Fluid Shear Stress

LSS	Laminar Shear Stress
OSS	Oscillatory Shear Stress
TSA	Trichostatin A
MET	Methylstat
VEGF	Vascular Endothelial Growth Factor
EMT	Epithelial-Mesenchymal Transition
TGF β 1	Transforming Growth Factor Beta-1
H3K9ac	Acetylation at the 9 th lysine residue of histone 3
H3K27me ₃	Tri-methylation at the 27 th lysine residue of histone 3
H3K9me ₃	Tri-methylation at the 9 th lysine residue of histone 3
LSM	Laser scanning microscope
FRET	Förster Resonance Energy Transfer
FRAP	Fluorescence Recovery After Photobleaching
FLIM	Flourescence Lifetime Imaging Microscopy

ABSTRACT

DNA CONDENSATION STATE REGULATES NUCLEAR LAMINA TENSION AND CELLULAR ADAPTATION TO PHYSIOLOGICAL FORCES

By: Brooke Danielsson

A Dissertation submitted in partial fulfillment of the requirements for the degree of Doctor of
Philosophy at Virginia Commonwealth University.

Virginia Commonwealth University, 2022

Director: Daniel Conway, Ph.D.
Associate Professor, Department of Biomedical Engineering

The nucleus is the largest and stiffest organelle and is exposed to mechanical forces transmitted through the cytoskeleton from outside the cell, as well as from forces generation within the cell. In recent years, the nucleus has been proposed to act as a cellular mechanosensor, with changes to nuclear shape and architecture playing an important role in how the cell responds to physiological forces. Aberrant forms of the nuclear envelope protein lamin A/C, as well as epigenetic modifications to chromatin, has been shown to modify nuclear stiffness and viscosity, therefore effecting nuclear mechanics and mechanotransduction. Altered nuclear mechanics is associated with many human diseases, including heart disease, muscle dystrophy, progeria, and cancer. My PhD work explores how changes to the nuclear lamina protein lamin A/C, as well as changes to chromatin condensation, effects endothelial cell adaptation to fluid shear stress (FSS). In addition, I developed a novel lamin A/C intermolecular force sensor to

better understand if the nuclear lamina experiences force and if so, identify the factors contributing to it.

To better understand how changes to nuclear architecture effect cellular response to force we perturbed nuclear structures lamin A/C, progerin, and DNA condensation, and analyzed the mechanotransmission changes in cells under external forces. We show endothelial cells (EC) expressing progerin do not align properly with patterning, nor do they adapt to FSS. EC with lamin A/C overexpression had stalled cell adaptation to FSS as well. In addition, fibroblasts expressing progerin do not align properly to applied cyclic force. We show that progerin microaggregate inclusions in the nuclear lamina lead to cellular and multicellular dysfunction. This work shows that the integrity of the nuclear lamina is crucial for proper cell adaptation to cyclic stretch and shear stress.

How changes to DNA condensation effect endothelial cell alignment upon application of FSS is not well studied. Using both *in vitro* and *in vivo* models of EC adaptation to FSS, we observed an increase in histone acetylation and a decrease in histone methylation in EC adapted to flow as compared to static. Using small molecule drugs, as well as VEGF, to change chromatin condensation, we show that decreasing chromatin condensation enables cells to more quickly align to FSS, whereas increasing chromatin condensation inhibited alignment. Additionally, we show data that changes in chromatin condensation can also prevent or increase DNA damage, as measured by phosphorylation of γ H2AX. Taken together these results indicate that chromatin condensation, and potentially by extension nuclear stiffness, is an important aspect of EC adaptation to FSS.

To determine if lamin A/C experiences direct mechanical force, we developed a technique to measure forces on the nuclear lamina using a lamin a/c strain sensor in Madin-Darby Canine Kidney Cells (MDCK). Correct localization was confirmed by comparing the sensor to lamin A/C immunofluorescent staining. Osmotic shrinking and swelling experiments were also performed to confirm the efficiency of the strain sensor. Using FRET, we saw that strain in the lamin A/C meshwork was heterogeneous, both cell to cell and also within individual cells. Cytochalasin D, ROCK inhibitor, and DN-KASH experiments were performed to determine actin's role of applying force on the lamina. We saw a decrease in strain on the lamina when actin filaments were disrupted. Additionally, treatment with Trichostatin A, to decondense chromatin and Methylstat, to condense chromatin, increased and decreased FRET, respectively, suggesting that lamin A/C strain is also proportional to chromatin stiffness. Taken together, this data shows that the nuclear lamina experiences force, and this force is influenced by both external (actomyosin) and internal (chromatin) changes. This novel technical innovation is a tool that will aid several studies in nuclear mechanobiology.

CHAPTER 1: INTRODUCTION

1.1 RATIONALE

The nucleus is the largest and stiffest organelle and is exposed to mechanical forces transmitted through the cytoskeleton from outside the cell, as well as from forces generation within the cell (1). In recent years, the nucleus has been proposed to act as a cellular mechanosensor (2, 3), with changes to nuclear shape and architecture playing an important role in how the cell responds to physiological forces. Although most research has been focused on the nuclear lamina, it is now broadly accepted that chromatin condensation contributes to nuclear rigidity (4, 5). Aberrant forms of the nuclear envelope protein lamin A, as well as epigenetic modifications to chromatin, has been shown to modify nuclear stiffness and viscosity, therefore effecting nuclear mechanics and mechanotransduction (6). Altered nuclear mechanics is associated with many human diseases, including heart disease, muscle dystrophy, progeria, and cancer (7).

The overall goals of this PhD dissertation are to 1) provide insight into the role chromatin condensation and the nuclear lamina have in nuclear adaptation and response to fluid shear stress and 2) better understand if and how the nuclear lamina directly experiences force.

1.2 OBJECTIVES

Modifications to the nuclear lamina and chromatin alters endothelial cell adaptation under shear stress. Blood vessels are under constant mechanical loading from blood pressure and flow. Endothelial cells (EC), which line the interior of blood vessels, are exposed to fluid stress via the frictional drag caused by blood flow. When vasculature is unable to responds to these forces, EC homeostasis is disrupted, leading to cardiovascular disease such as atherosclerosis. In healthy EC, the nucleus and actin filaments undergo remodeling to become

oriented with the direction of flow. However, in EC dysfunction, remodeling is not seen, and the actin fibers are randomly oriented, leading to inflammation. In this study we aimed to better understand how changes to the nuclear lamina, caused by overexpression of lamin a/c and progerin (chapter 4), as well as changes to DNA, by condensation and de-condensation, affect the endothelial cell response to physiological levels of shear stress (chapter 5). We sought to establish the role these nuclear structures have in EC adaptation and its implications in cardiovascular disease. Through this work, the nucleus' response and adaptation to mechanical force was investigated (chapter 3-5). We observed that cells expressing progerin have stiffened inclusions and altered mechanotransmission to the nucleus (chapter 3). We showed that EC with decondensed DNA align faster under laminar shear stress than condensed DNA or wildtype (chapter 5). Furthermore, nuclear adaptation was stalled in progerin-expressing EC, as well as EC with lamin A overexpression (chapter 4). Our results provide a framework for understanding the differential effects of chromatin and lamin A in EC nuclear mechanics and their alterations in the cardiovascular system.

Identifying the balance of forces between chromatin and actin in generating strain on the nuclear lamina. It is widely established that the nuclear lamina plays a significant role in mechanotransmission for the nucleus but the mechanism in which the lamina directly experiences force has not been well characterized(8–11). In this study we aimed to establish whether or not the nuclear lamina is under mechanical strain, and if so, what is mediating that strain. We have developed a novel technique to measure forces on the nuclear lamina using a Lamin A TSmob in Madin-Darby Canine Kidney Cells (MDCK). Using this sensor, we investigated the cellular factors that contribute to nuclear lamina forces, as well as determined

how physiological processes (cell cycle, EMT) regulate lamin A/C forces (chapter 6). Our results showed that chromatin decondensation reduces strain on the nuclear lamina and that cells arrested in the G1 phase of the cell cycle (after the cell enlarges and before the DNA duplicates) also have reduced nuclear lamina strain. The development of the novel filamentous sensor allowed us to gain a better understanding of the mechanical forces at the nuclear lamina which govern its adaptability and elasticity. This innovative technological approach will allow outstanding questions in the rapidly growing field of nuclear mechanotransduction to be answered.

CHAPTER 2: BACKGROUND

Nuclear mechanobiology is a specialized field focusing on how the cell's nucleus adapts and responds to externally and internally-applied forces. My PhD thesis focuses on how changes to nuclear structures effects cellular adaptation to force. In this chapter I describe several key topics of background information pertaining to my work.

Mechanostranduction

The mechanisms in which cells adapt and regulate mechanical stress are detrimental to cell survival. Cellular behavior is continuously affected by its microenvironmental and related forces through the process of mechanotransduction, in which mechanical stimuli is rapidly converted into biochemical responses (12). Mechanotransduction plays a critical role in cell and tissue differentiation, maintenance, and disease. For example, in the adaptation of bones and muscle to exercise or the alignment of endothelial cells to fluid shear stress (13). It has been accepted by a number of studies (14–16) that the nucleus acts as a mechanosensing element, and when under force, can induce changes in nuclear envelope structure, chromatin organization, and gene expression—which then drives downstream cellular responses (17, 18). Physical connections between the cytoskeleton and the nuclear envelope provide a mechanism to transmit extracellular and cytoskeletal forces to the nucleus that is critical for nuclear mechanotransduction.

The Structure of the Eukaryotic Nucleus

The cell nucleus is typically spheroidal or ellipsoid. However, due to changes in expression of structural and binding proteins some specialized cells undergo dramatic changes in

nuclear shape during differentiation and maturation. The structure of the nucleus can be seen in **Figure 1**. The nuclear envelope (NE) is composed of two phospholipid bilayer membranes: the inner nuclear membrane (INM), to which the nuclear lamina is attached, and the outer nuclear membrane (ONM), which is contiguous with the endoplasmic reticulum (ER). Separating the INM from the ONM is a perinuclear space which is about 30-50nm wide. The nuclear envelope serves as a protective membrane for the genome as well as a bidirectional communication system through the nuclear pore complexes (NPC) between the nucleus interior and cytoplasm of the cell(1–3). The NE has been shown to be elastic(19), dynamic, and highly adaptable by changing composition during cell differentiation, deforms in response to mechanical challenges, and can be repaired upon rupture (20). The nucleus is mechanically tethered to the extracellular environment, adhesion receptors, and the contractile cytoskeleton through adaptor-protein-mediated interactions at the nuclear envelope, known as the LINC complex (Linker of Nucleoskeleton and Cytoskeleton). The LINC complex is formed by the interaction of nesprins and SUN proteins at the nuclear envelope(21). The nuclear lamina, which underlies the NE, is composed of a dense meshwork of intermediate filament proteins called lamins and lamin-associated proteins (22, 23). These lamin binding proteins help connect the lamina to the INM and connect lamins to chromatin structures and gene regulatory components. Nuclear lamins are divided into A and B subtypes. lamins A and C are derived from the *LMNA* gene by alternative splicing, whereas lamins B1 and B2 are derived from two separate genes *LMNB1* and *LMNB2*. The B type lamins are expressed in every cell, whereas A type lamins is developmentally regulated (24) with high expression levels in skeletal and cardiac muscle(25, 26). The nuclear lamina plays a critical role in the maintenance of nuclear architecture and stability, genome organization and function (including chromatin organization, DNA replication, transcription, and

repair) as well as the assembly and disassembly of the nucleus during cell division (27–29). Defects in the A-type lamins cause a broad spectrum of tissue-specific and systemic diseases referred to as laminopathies. Disease manifestations include muscular dystrophies, lipodystrophies and the premature aging syndrome Hutchinson-Gilford Progeria (HGPS).

The nucleus contains DNA that is wrapped around histones which are organized into higher-order structures—categorized as either open, transcriptionally active euchromatin or condensed, inactive heterochromatin. Whereas euchromatin is often located at the nuclear interior, heterochromatin exists at the nuclear periphery and interacts with the nuclear lamina in Lamin-associated domains (LADs)(30, 31) and via Lamin-associated protein 2 (LAP2) and its binding partner, barrier to autointegration factor (BAF)(32–34). These interactions may directly affect chromatin organization, nuclear mechanotransduction, and gene expression.

The cell cytoskeleton is made up of actin (provides contractile forces), microtubules (bears compression to form a network allowing organelles and proteins to move throughout the cell), and intermediate filaments (provides structural reinforcement). These structural features act together to provide cell shape, support and mechanical integrity and are necessary for cell motility and division. The cytoskeleton has complex viscoelastic properties and is known to actively participate in transmitting force to the nucleus.

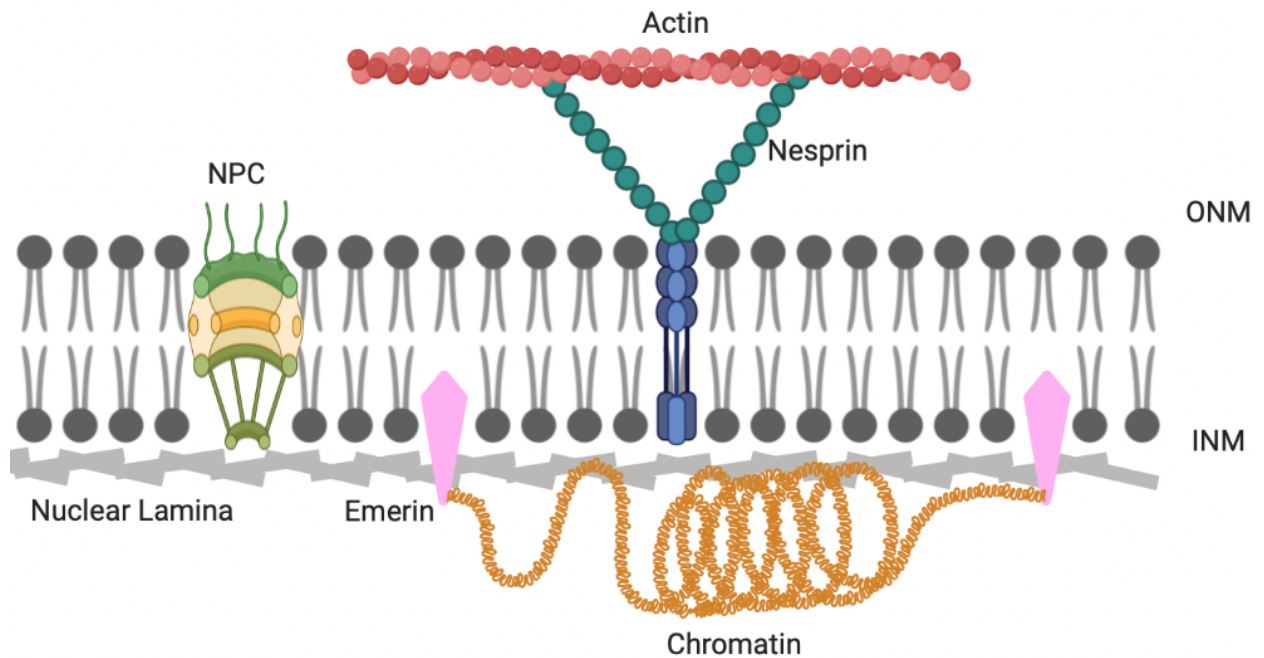


Figure 1: The structure of the eukaryotic nucleus.

Nuclear Lamins and Chromatin in Nuclear Mechanostratduction

The LINC complex allows for the transfer of force from the cell’s cytoskeleton to the nucleus. The identified mechanisms in which the nucleus responds to force is a) nuclear membrane and pore stretching b) protein phosphorylation and conformational changes c) chromatin modification. My PhD work has focused on how two structural properties of the nucleus respond to force: lamin A/C and chromatin.

It has been long thought that the nuclear lamina is the major player in nuclear mechanical response —the way in which the cell nucleus deforms and reacts to external forces(35, 36)—but recently chromatin condensation has been named as an important contributor as well. It has been shown that chromatin structures have a viscous flow and will deform plastically under high

mechanical strain, whereas the nuclear lamina stretches elastically and will recover. In 2017 *Stephens et al* showed through micromanipulation of isolated nuclei that chromatin governs the nuclear response to small extensions ($<3 \mu\text{m}$), whereas lamin A/C levels respond to large extensions (37). In addition, euchromatin and heterochromatin levels can modulate nuclear stiffness in dependent of lamins. The rheological character of the nucleus is thus set largely by nucleoplasm/chromatin, whereas the extent of deformation is modulated by the lamina (38).

The research done in chapters 3-5 studies how modulating the nuclear lamina, as well as chromatin condensation, affects cellular adaptation to fluid shear stress. Healthy endothelial cell monolayers exposed to fluid shear stress respond to the force by the elongation of their nuclei and rearranged actin fibers in the direction of flow. I explore if a change in nuclear structure effects this adaptation to force. This work provides insight into the how changes in nuclear lamins (through overexpression of lamin A/C as well as using a Hutchinson-Gilford Progeria Syndrome disease model) and chromatin condensation effects cellular and nuclear response in a physiological model.

Diseases related to Altered Nuclear Mechanics

Characterizing the mechanical properties of the cell's nucleus is an important factor for understanding the function and behavior of normal and disease cells. Alterations of nuclear mechanics and structures are hallmarks of several human diseases such as premature aging seen in Hutchinson-Gilford Progeria Syndrome (HGPS), Emery-Dreifuss Muscular Dystrophy (EDMD), cancer, and several heart diseases including cardiomyopathy and atherosclerosis(39, 40). Altered nuclear envelope elasticity may also affect force transmission from the cytoskeleton

to the nucleus as well as how forces are sensed within the nucleus, thereby modulating the response of mechanosensitive genes.

The work done in chapter 3 and 4 focus on the altered nuclear mechanotransmission (defined as the transmission of mechanical forces through cellular components, which in this research we focus on the transmission along actin stress fibers), in a HGPS model. HGPS, often called Progeria, is a rare premature aging disease found in children and caused by a single-point mutation in the LMNA gene, resulting in a truncated and farnesylated form of lamin A called progerin (**Figure 2**). The mutant accumulates at the nuclear periphery, altering the nuclear lamina structure, and leads to several downstream nuclear defects, including: abnormal nuclear morphology, increased nuclear stiffness, redistribution of heterochromatin, modified nuclear pore structure, alterations in gene expression and nuclear structural instability (41–46). Vascular studies are of particular interest because progerin is most pronounced in force-responsive tissues, such as cardiovascular tissues. Patients with progeria typically die from atherosclerosis or stroke. Surprisingly there are limited studies characterizing the endothelial cell dysfunction in progerin-expressing cells. The work described herein will fill these gaps and provide a better understanding of the diseased endothelium in relation to its response to force.

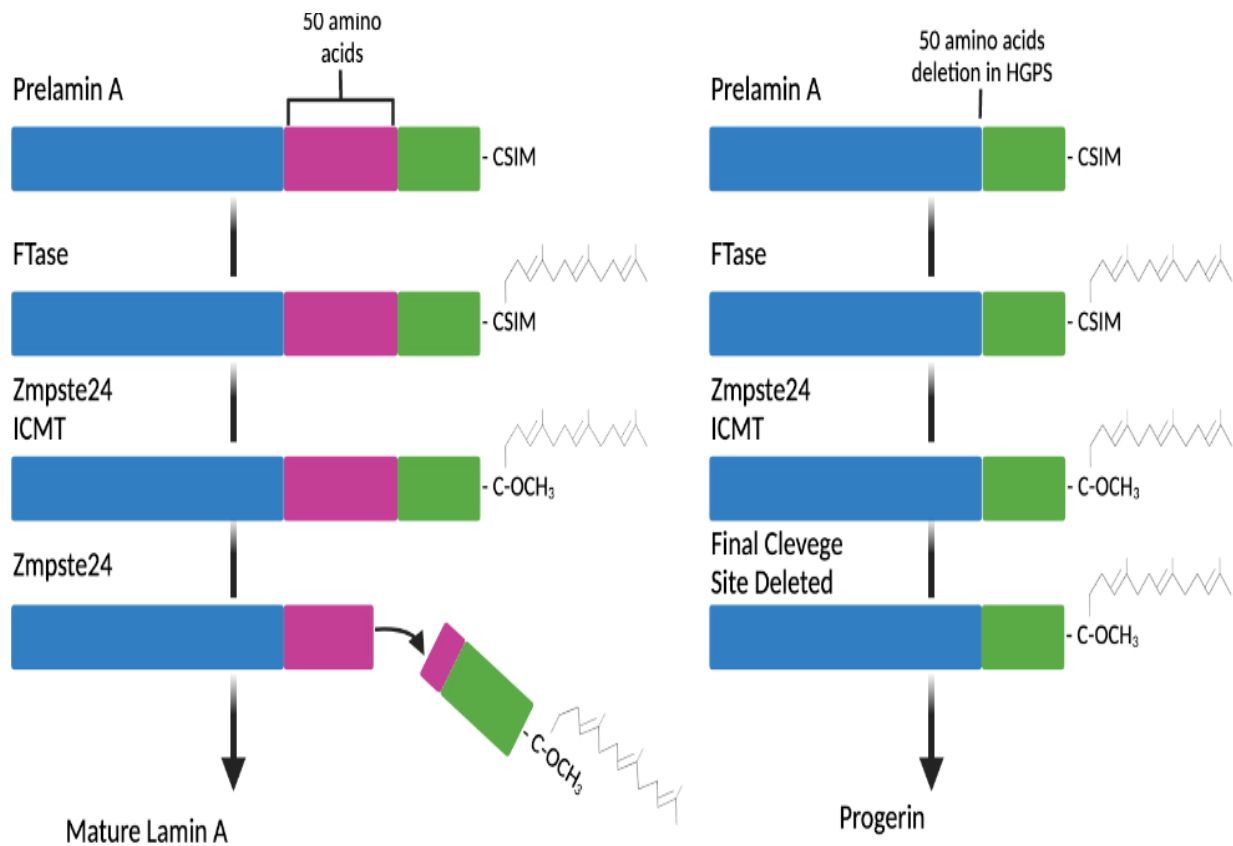


Figure 2: Post-translational modification for lamin A processing.

Biosensors

The development of genetically encoded molecular force sensors allows for the quantification of tension or strain on desired proteins in living cells. The basic principles of force sensors is centered around a tension sensor module (TSMOD) that uses Förster resonance energy transfer (FRET) to analyze changes in force(47–49). Traditionally, TSMOD comprises two FRET fluorophores, separated by a linker peptide that reversibly extends when under mechanical force, leading to an increase in fluorophore separation distance and a decrease in FRET efficiency (Figure 3).

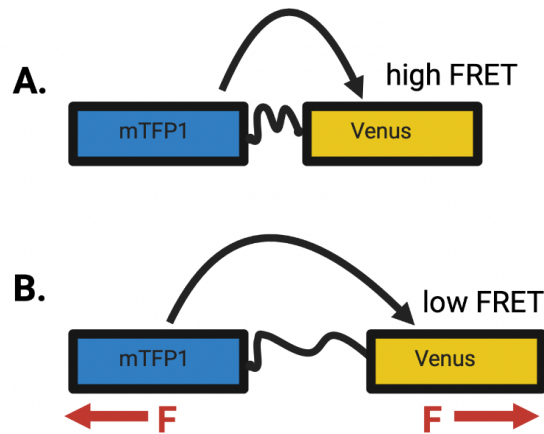


Figure 3: Traditional force sensor design. (A) The tension sensor module (TSMOD) structure with two fluorophores separated by a flagelliform linker sequence. (B) Upon an applied force, the elastic linker extends, causing a decrease in FRET efficiency (F denotes force).

The work in Chapter 6 describes a novel technical approach to estimate mechanical strain on the nuclear lamina protein lamin A/C using a FRET-based sensor. Rather than inserting the TSMOD directly into the protein of interest like how other biosensors are made (49–51), we chose an indirect approach to measure the strain between the filaments. This was done by placing an existing lamin A/C nanobody on each side of TSMOD to avoid disruption of the filament assembly (52, 53). Significant insights were gained using the strain sensor to determine the factors responsible for strain on or within the nuclear lamina.

There are several important questions in the field of nuclear mechanobiology my PhD work has answered. Many have studied how changes to nuclear structures affect cellular response to applied forces, but my work is unique in that I am the first to show these altered cellular responses in a shear stress model. I have identified that changes to the nuclear lamina affect mechanotransmission to the nucleus (chapter 3) and effects cellular adaptation to force (chapter 4). In recent years chromatin's contribution to cellular adaptation has been explored. In

chapter 5 I detail how changes in DNA condensation state directly impacts endothelial cell remodeling upon applied shear stress. Arguably my biggest contribution to the field has been my work showing that the nuclear lamina is under strain, confirmed using a newly designed FRET force sensor (chapter 6).

CHAPTER 3: LAMIN MICROAGGREGATES LEAD TO ALTERED MECHANOTRANSMISSION IN PROGERIN-EXPRESSING CELLS

Danielsson, B.E., Tieu, K.V., Bathula, K., Armiger, T.J., Vellala, P.S., Taylor, R.E., Dahl, K.N., Conway, D.E. 2020. Lamin microaggregates lead to altered mechanotransmission in progerin-expressing cells. Nucleus. DOI: 10.1080/19491034.2020.1802906

3.1. RATIONALE

Increasingly detailed structural analysis of the nuclear lamina has emerged showing filament size(54, 55), disparate network localization with the nuclear membrane(56) and nuclear pore association(57). Mutations of *LMNA*, which codes for A-type lamins, cause numerous diseases impacting different tissue types depending on the mutation. However, the increasingly accurate information on lamin architecture is not necessarily coupled with a better understanding of how altered lamina structure relates to cellular and tissue level dysfunction. This disconnect between molecular assemblies and cellular dysfunction prevents a full characterization of disease pathologies and movement toward treatment and therapy options.

Hutchinson-Gilford progeria syndrome (HGPS) is a rare premature aging disease in children(58) caused by an autosomal dominant mutation in the *LMNA* gene. The mutation results in an alternate splicing of exon 11 leading to a loss of 50 amino acids in the tail domain(59). This altered splicing occurs at extremely low but perceivable levels in wildtype cells as well, leading to a similar cellular phenotype in aged cells(41, 42, 44). This splice variant of *LMNA* associated with HGPS is called progerin or $\Delta 50$ lamin A and retains a C-terminal farnesylation and carboxymethylation that mature lamin A loses during processing(60). Ultimately, progerin expression leads to an accumulation of structural proteins in the lamina (progerin plus the retention of other lamins), altered nuclear shape, redistribution of heterochromatin, modified

nuclear pore structure, alterations in gene expression and nuclear structural instability(43, 45, 61).

Important to this study, progerin expression changes both nuclear lamina mechanics and nuclear shape. Progerin-expressing cells have altered nuclear morphologies that have been described as blebs, wrinkles or folds(62, 63). Progerin expression and HGPS are associated with increased lamina stiffness. It is unclear how an increase in a structural protein and a stiffening of the lamina could lead to the blebbed nuclear lamina, which is seemingly related to lamina fragility. Our studies and others have observed the formation of microaggregates of progerin within the lamina(64–66).The goal of this study is to show the mechanical impacts of stiffened inclusions of progerin microaggregates and how these ultimately manifest in cells as mechanical dysfunction of the nuclear lamina. We aim to link the overaccumulation of progerin associated with HGPS to ultrastructure changes in the nuclear lamina and dysfunction in cells under force. Thus, changes in lamina structure could explain cellular and tissue level disease. We investigate strains in cells under confinement and cells under external forces. In considering our data and models correlating the formation of microaggregates of progerin to altered force propagation through the nucleus. We also show that cells expressing progerin do not align properly to external patterning or force cues, suggesting altered nuclear microstructure may impact cytoskeletal force transmission through the cell. These combined structural effects may have important functional consequences in HGPS and highlight the benefit of applying physical models to study biological systems to determine aspects of disease states.

3.2. METHODS

Cell Culture and Transfection

For HUVEC studies, primary HUVEC (pooled, passages 3–5, Lonza, Basel, Switzerland) were grown in EGM-2 medium (Lonza, Basel, Switzerland). To express progerin in HUVEC an adenovirus was developed to express HA-tagged progerin (HA-progerin was a gift of Bryce Paschal(67); adenovirus was prepared by Vector Biolabs, Malvern PA). The lowest level of adenovirus that infected nearly 100% of cells was used. To overexpress wild-type lamin A in HUVEC, lamin A adenovirus (based on RefSeq BC014507) was purchased from Vector Biolabs and used at an identical titer level as progerin. Western blots of lamin and progerin levels in HUVEC are shown in **Figure 5**. For actin depolymerization studies, latrunculin A (Tocris, Bristol, United Kingdom) was added at 10 μ M for reported times before cell fixation and labeling.

For fibroblasts studies, primary human dermal fibroblasts were cultured under 5% CO₂ in DMEM (Thermofisher) supplemented with 15% FBS (Thermofisher). The primary fibroblast cell lines used in our studies included AG06299 (normal) and AG11513 F (HGPS patient with mutation in exon 11 of LMNA gene), obtained from NIA Aging Cell Repository, Coriell Institute.

Micropatterning

HUVECs were seeded on micropatterned lines of width 20 or 40 μ m, as previously described(68). Briefly, the stamps used to micropattern fibronectin lines of 20 or 40 μ m were made with polydimethylsiloxane (PDMS). Stamps were coated with fibronectin and were pressed onto a prepared coverslip. Once stamped, the coverslips were washed and treated with

Pluronic F-127 to limit cell adhesion to only the fibronectin lines. Cells were then seeded onto the coverslip.

Cell stretching

Fibroblasts cells were seeded onto UniFlex culture plates (FLEXCELL International Corporation, NC) coated with 60 ng/mL of Fibronectin (Sigma). The cells were exposed to uniaxial stretch, using the FlexCell 5000 (FLEXCELL International Corporation, NC) with 10% strain and frequency of 0.5 Hz for 24 hours.

Cell Fixation, Immunocytochemistry Labeling and Western Blotting

Cells were fixed using 4% formaldehyde in phosphate buffered saline (PBS) and permeabilized using 0.2% Triton X-100 in PBS. For fluorescence microscopy experiments, cells were stained with 0.1 µg/mL Hoechst 33342 (ThermoFisher, Waltham, MA, USA) for DNA staining. HUVECs were stained with anti-lamin A/C antibody (cat # sc-7292, Santa Cruz Biotechnology, Dallas, TX, USA) for control cells or anti-HA antibody (cat # 901501, Biologend, San Diego, CA, USA) for progerin-expressing cells with an Alexa Fluor 488 fluorescent secondary (cat # A-21202, ThermoFisher, Waltham, MA, USA). HUVECs were also stained with rhodamine phalloidin (cat # PHDR1, Cytoskeleton, Denver, CO, USA). The same antibodies were used for Western Blotting quantification of overexpression.

Imaging and Analysis

Fibroblast cells were imaged using a Zeiss 710 LSM confocal at 20x and 63x and 1.4NA. Fixed HUVEC cells were imaged on a Nikon Eclipse TS100-F widefield fluorescence microscope with a 50x (1.4NA) oil immersion oil objective. Live HUVEC cells were imaged on a Leica DMI6000 inverted microscope using a 63x (1.4 NA) oil immersion objective. During

imaging, the entire microscope environment was regulated by a Pecon live-cell imaging chamber heated to 37°C. Images were processed using ImageJ. Alignment was done for more than 100 cells per condition, multiple fields of view, random sampling per field of view using the angle tool. Manual angle analysis using the angle tool was preferred to avoid biasing for artificially bright actin stress fibers of other structures. Methodologies for wrinkle analysis are presented in **Figure 11** (for data in **Figure 12**). Again, 100 cells were considered but, in some cases, only 20% of cells had wrinkles, but some cells had numerous wrinkles.

Simulations of inclusions

All modeling was completed in Comsol Multiphysics 5.3 using the two-dimensional (2D) plane stress module. The lamina was modeled as a uniform 2D elastic material with elastic modulus of 50 kPa. We chose this number based on Vaziri and Mofrad (69) with updates based on a new understanding of lamina thickness to be 10–100 nm based on super-resolution microscopy(55, 56); although scaling neglects the need for an absolute stiffness. Circular inclusions were modeled as linear elastic materials within the lamina. For this study, we approximated an infinite sheet by modeling a 4 μm by 4 μm square region of the membrane with a small inclusion ranging from 0.05 μm to 0.4 μm in diameter with varying stiffnesses. Unconfined 25% uniaxial strain in the x-direction (aside constraint holding the midline at $y = 0$) with Poisson ratio $\nu = 0.49$ resulted in a stiffness profile around the $y = 0$ axis. Von Mises stresses are shown and peak midline stresses are reported.

3.3. RESULTS

Progerin-expressing cells often show punctate inclusions or aggregates

Similar to other studies(64–66), we consistently observe punctate inclusions of progerin in cells overexpressing progerin, which are not observed in lamin A overexpressing cells or control cells (**Figure 4**). Densitometry analysis of Western blots (**Figure 5**) shows that lamin A overexpressing cells have 2.5x the lamin A compared with control cells; HA-progerin shows a 3x increase in A-type lamins with 2.5x of that increase from the HA-progerin. These aggregates at the nuclear lamina could be due to the altered stability of the tail domain of the progerin mutant compared to the wildtype(70), hydrophobic aggregation of the farnesyl tail of individual proteins within filaments, associations of the tail domains to specific regions of the inner nuclear membrane, or a combination of all of these(71). We did not observe any large differences in actin organization with overexpression of progerin nor in patient cells (**Figure 6**). These aggregates are observed (and likely exaggerated) in overexpressing cells, but regions of domain formation are also observed in patient cells (**Figure 7**)(41).

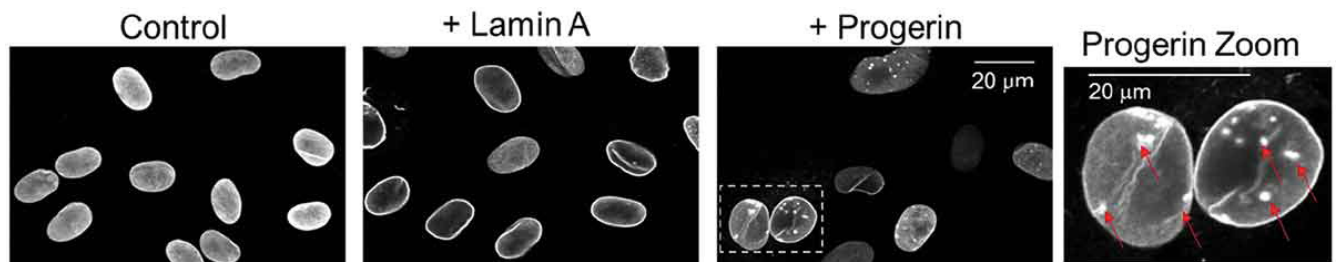


Figure 4: Punctate inclusions in progerin-expressing nuclei. Confocal images of HUVECs labeled via immunocytochemistry for endogenous LA/C, overexpressed LA and HA-tagged progerin. Control and LA cells show uniform equatorial labeling with some wrinkles due to actin fibers whereas progerin-expressing nuclei show punctate inclusions (arrows). The z-resolution for the lamin channel (488 nm) was chosen at 1.0 µm, so folds and puncta of the nuclear face may appear in the same confocal frame as the midline edge.

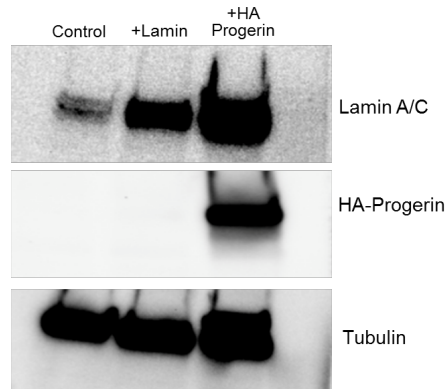


Figure 5: Western blot of lamin A/C overexpression and HA-progerin expression in HUVEC to determine approximate protein levels from adenovirus.

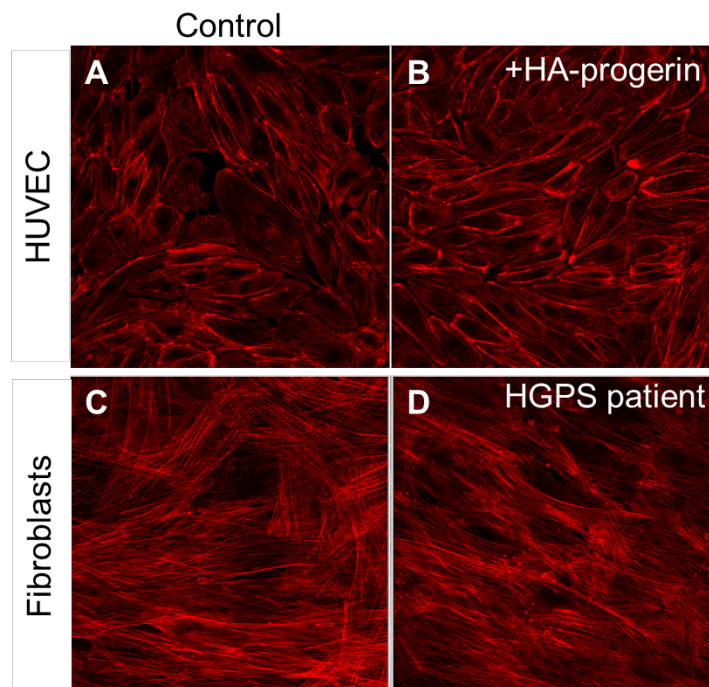


Figure 6: Comparison of actin fiber organization of HGPS patient cells and HA-Progerin model system. (A) Control HUVEC. (B) HA-Progerin HUVEC. (C) Control Fibroblasts. (D) HGPS-Patient Fibroblasts. We did not observe any differences in actin organization with

progerin expression compared to control cells. Furthermore, there were no observed differences between progerin expression in HUVEC to HGPS patient fibroblasts.

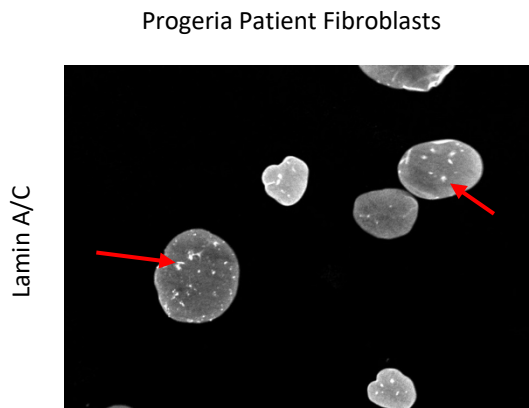


Figure 7: Punctate inclusions in progerin patient fibroblast nuclei. Progeria patient fibroblasts stained with Lamin A/C and imaged with Zeiss confocal microscope. The same microaggregates are observed (arrows) in patient cells as they are seen in model system of HA-progerin.

Simulations of stiffened inclusions show stress fields consistent with wrinkling

To consider the consequence from aggregation of stiffening elements, we utilized a simulation to consider a stiffened region within the lamina, most simplistically modeled as a 2D continuum. We approximated the stiffness of the lamina (50 kPa, see Methods), added a stiffened inclusion within the uniform field (black circle), and then uniaxially strained in the x-direction and pinned along the black line at $y = 0$ (**Figure 8**). We then tracked the peak stress along the midline outside of the inclusion. High stresses in deviation from the bulk would lead to asymmetries that could initiate out of plane bending. Importantly, we found that the size of the inclusion (from 50 to 400 nm) did not influence the peak midline stress (**Figure 9**). However, the ratio of stiffness of the inclusion to the material led to greater midline stresses, as expected

(Figure 8). Thus, we suggest that the presence of stiffened inclusions leads to larger-scale stress features in the bulk of materials under strain. This continuum simulation shows the initiation of stresses, but it is important to state that any further analysis of instabilities or out-of-plane bending should be considered in a course-grained filamentous model.

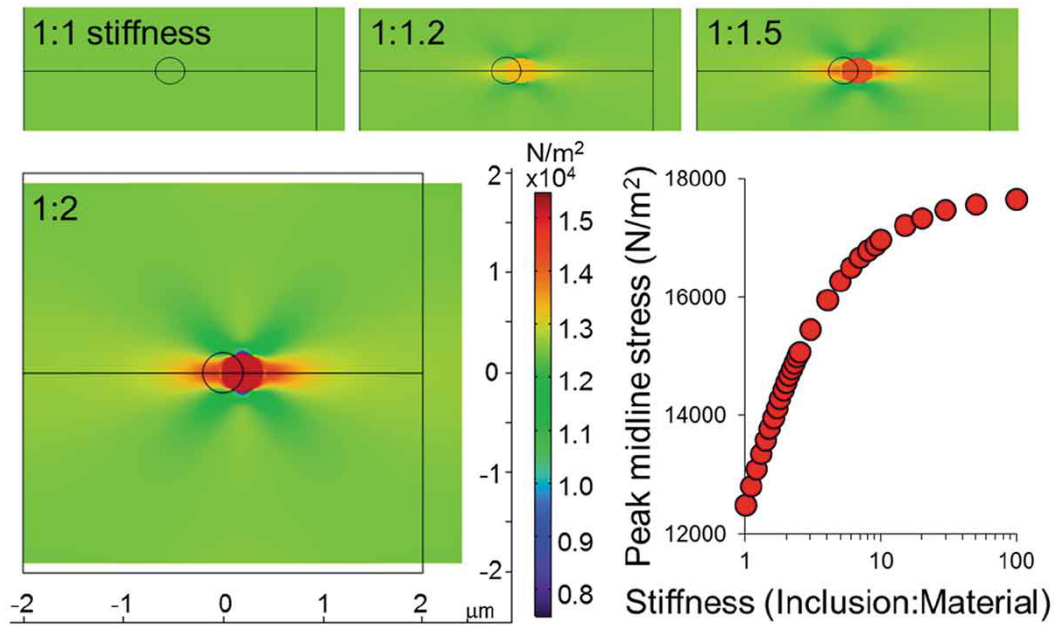


Figure 8: Strain on an inclusion of increased stiffness causes a line of increased stress normal to the imposed strain. Comsol simulation of a homogeneous structure with a stiffened inclusion is compressed in y and dilates in x. The resulting von Mises stiffness profile is shown for increasing inclusion stiffnesses (1, 1.2, 1.5 and 2x as stiff as the background material). The peak midline stress in the x-direction outside of the inclusion is plotted as a function of stiffness ratio.

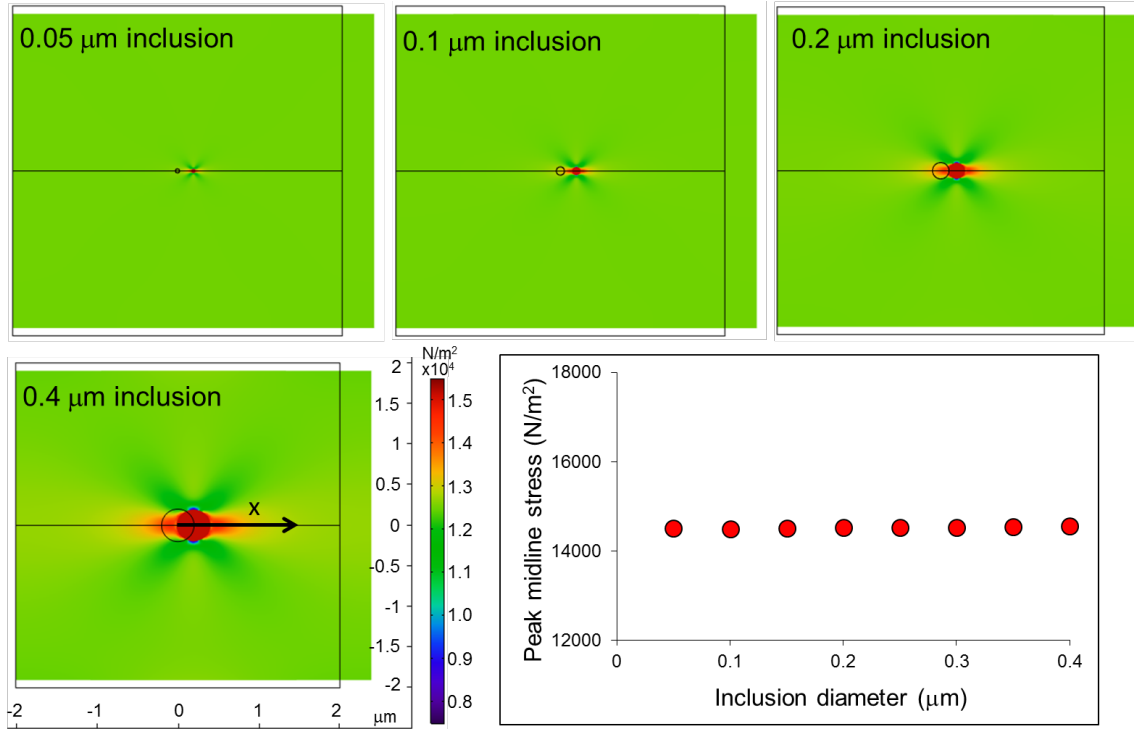


Figure 9: Simulations for measuring peak midline stress as a function of inclusion size.

Changes in size of an inclusion (1:2 inclusion:material stiffness) shown as 50, 100, 200 and 400 nm in a 4 μm by 4 μm square matching the stiffness of the nuclear lamina (50 kPa). The inclusion causes a midline stress along the x-axis, and the peak midline stress is independent of the inclusion size.

Endothelial cells confined to one-dimensional patterns show differential lamina deformation

To examine the role of extracellular perturbation on nuclear lamina reorganization, we considered how cells respond to growth on patterns. Endothelial cells were grown on patterned lines of 20 μm or 40 μm in order to ascertain the extent of deformation of the lamina network under cell confinement. Previously, patterning on lines of this thickness has been shown to exert

forces on the nucleus from the cytoskeleton(68, 72, 73). On 20 μm lines, nuclei are oblate and orient in the direction of the actin filaments. This orientation has been shown to be a direct function of the cellular confinement to patterning (24). There are some folds in control lamina, but these coincide with actin filament structures (**Figure 10(a–d)**). Progerin-expressing cells show numerous folds and wrinkles in the nuclear lamina, but these dysmorphic structures do not align or co-register with confocal actin filament structures at a similar plane (**Figure 10(e–h)**).

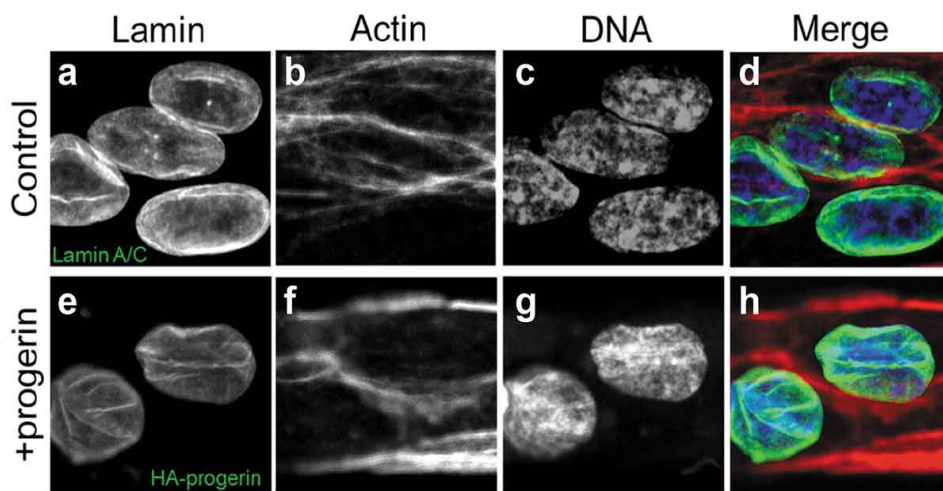


Figure 10: Confocal fluorescence microscopy confocal sections for cells patterned on lines.

Fixed HUVECs were stained for Lamin (control) or HA (Progeria), and all cells were also stained for actin (phalloidin) and DNA (Hoechst 33342). **(a)** Lamin A/C (control) stained with a lamin A/C antibody. **(b)** Control cell stained for actin to check the orientation of folds against the filament structures. **(c)** Lamin A control cells with Hoescht staining for DNA. **(d)** Merge of the lamin and actin channels shows nuclear alignment with the stripes and lamin folds coincident with the actin filaments. **(e)** Progerin-expressing cells stained with anti-HA to label HA-progerin express more wrinkles. **(f)** Progerin-expressing cells stained for actin to show the orientation of folds against the filament structures. **(g)** Progerin-expressing cells with Hoescht 33342 staining

for DNA. (h) Merge of the lamin and actin shows lamin folds distinct from actin filaments. For both conditions the z-resolution for the lamin channel (488 nm) was chosen at 3.5 μm , actin channel (561 nm) 1.9 μm and DNA channel (405 nm) 1.3 μm .

We quantified the dysmorphic structures or wrinkles observed in the lamina, visualized in **Figure 10** along the length of the nucleus and compared them to the orientation of the nucleus (see schematic in **Figure 11A**). Note that z-resolution of lamins was 3.5 μm – larger than normal confocal sections – to allow full visualization along the length of the nuclear lamina wrinkle. Earlier studies have suggested that cells under extreme loading conditions or, in this case, confinement may propagate wrinkle or fissure formations (25). Lamin networks that are healthy have been found to deform uniformly under similar conditions (24). For cells patterned on 20 μm stripes, wrinkles observed in the lamina (seen in **Figure 10**) were not statistically different for control and progerin-expressing endothelial cells (**Figure 12(a)**). As an additional control, we also overexpressed wild-type lamin A in cells to ensure that the results were from progerin expression and not from either increased lamin A or from viral treatment. Levels of exogenous lamin A, measured from confocal immunocytochemistry, were $204 \pm 43\%$ higher compared to wildtype cells. Endothelial cells grown on wider, 40 μm stripes without progerin did not show any wrinkles whereas progerin-expressing cells had wrinkles statistically similar to cells without progerin grown on 20 μm stripes (**Figure 13(a)**).

In cells on 20 μm stripes, we also considered the orientation of the wrinkles (**Figure 13(b)**). Our data indicate that the most deformations in control nuclear lamina structures lie in the direction of the primary orientation of the cells with more than half at 0–20° (**Figure 12(b)**). This agrees with the organized actin cytoskeleton visible along the length of the stripes visible in the overlays (**Figure 6**). Conversely, progerin-expressing cells displayed angles ranging from

40° to 90° for many of these folds. For progerin-expressing cells on 40 μm stripes, there is an increased number of wrinkle formations in the range of 80–90°, which is nearly normal to the applied force from the actin cytoskeleton (**Figure 13(b)**).

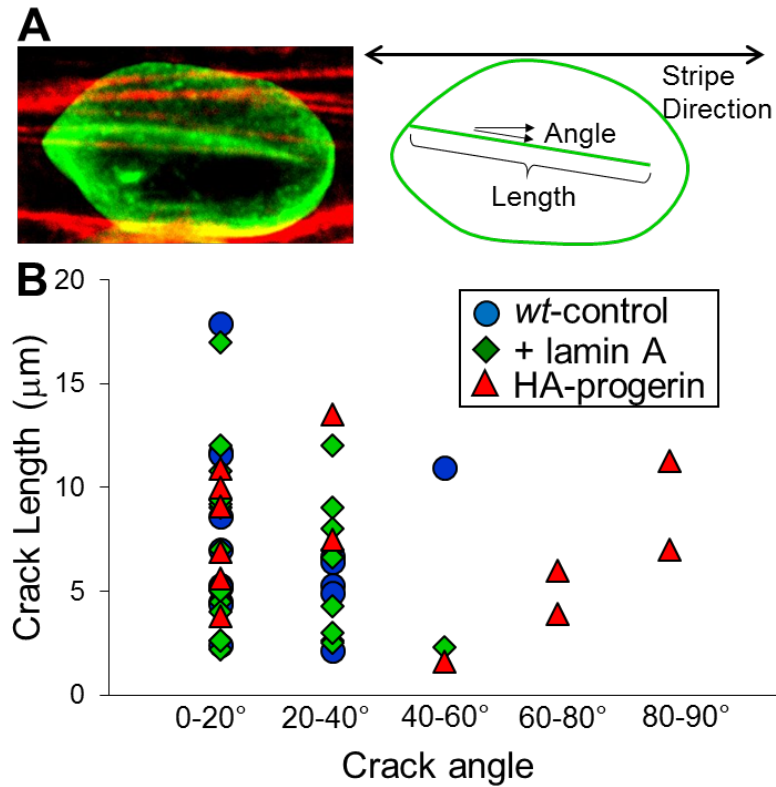


Figure 11: Methodology of measuring the angle and length of wrinkles. (A) We measure the length of the wrinkle or crack and the angle of the wrinkle with respect to the actin patterned stripe. **(B)** Comparison of crack length versus crack angle shows no particular correlation.

To compare control versus progerin-expressing cells, we considered cells on 20 μm stripes and quantified the wrinkles in the nuclei. In cells confined on the stripes, we depolymerized actin using latrunculin A, fixed cells at increasing time, and imaged the nuclear lamina in control and HA-progerin expressing cells. The actin depolymerized within a minute as expected but the wrinkles in nuclei took some time to be removed, likely based on the stiff mechanics of the nucleus. We plotted the length of wrinkles versus time after actin depolymerization treatment to determine if there was a difference in the loss of wrinkles. From the plot (**Figure 12(c)**), the wrinkle loss from both cases can be modeled as an exponential decay. Fits of exponential decay of control and HA-progerin are shown in **Figure 12(c)**; progerin-expressing cells show a slower loss of wrinkles on a timescale of 111 min versus 45 min control cells. Exogenous-lamin A expressing cells are statistically similar to control at 0 and 60 min (**Figure 12(d)**).

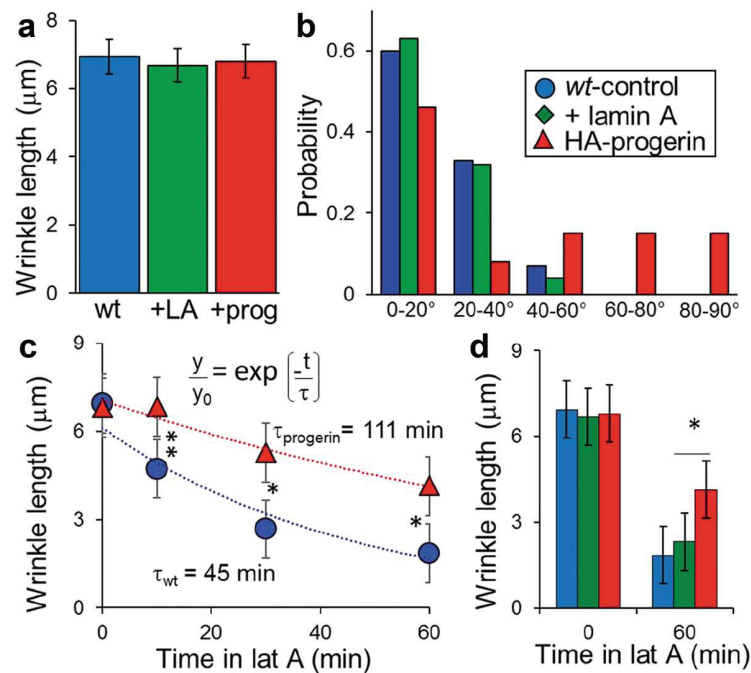


Figure 12: Formation of wrinkles for cells under one-dimensional confinement. (a) Length of deformations or wrinkles for control, exogenous lamin A or HA-progerin expressing

endothelial cells cultured on 20 μm diameter stripes. **(b)** On 20 μm diameter stripes, wrinkles in control cells and exogenous lamin A expressing cells (+ lamin A) primarily align with the stripe axis whereas HA-progerin-expressing cells do not show preferred orientation. **(c)** On 20 μm diameter stripes, treatment with latrunculin A and fixation at different time points shows an exponential decay. **(d)** Fits of exponential decay shows the differential decay constants for control and exogenous lamin A versus HA-progerin cells. Fits same for 4 points as 2 points. 30–50 cells per condition considered. * indicates statistically similar $p > 0.05$; ** indicates $0.001 < p < 0.05$; (c and d) no * indicates statistically different with $p < 0.001$ using unpaired Students t-test.

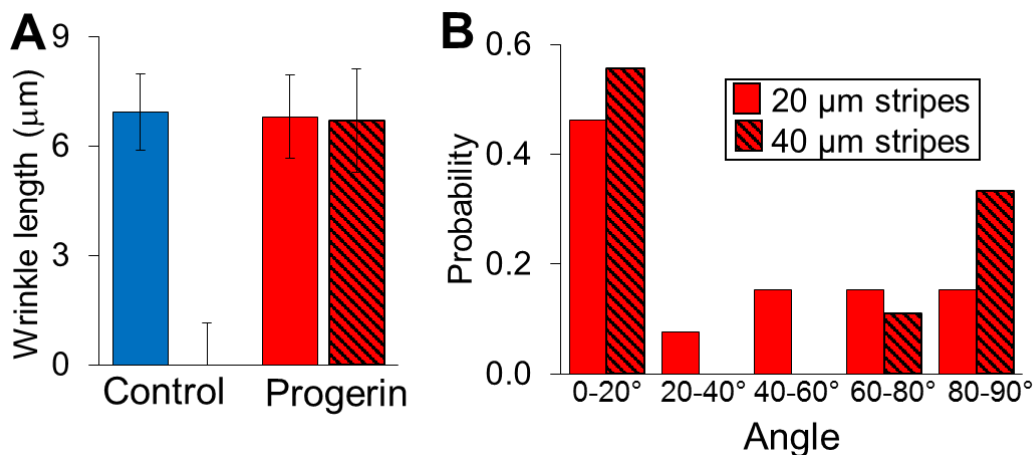


Figure 13: Wrinkle comparison on 40 μm stripes versus 20 μm stripes. (A) Length of deformations or wrinkles for control or HA-progerin expressing endothelial cells on 20 μm or 40 μm diameter stripes. On 40 μm stripes, control cells show no wrinkles whereas cells expressing progerin do. **(B)** For progerin-expressing cells, orientation preference of the wrinkles is further lost as the stripe diameter widens. 30-50 cells per condition considered.

Fibroblasts fail to align when exposed to uniaxial stretch

In addition to defects associated with exogenous progerin-expressing cells, we also aimed to examine cells from HGPS patients. HGPS patient fibroblasts are available from the Coriell Institute, along with HGPS control fibroblasts. Fibroblasts have previously been shown to align when the substrate is deformed perpendicular to the applied stretch(74). The alignment of nuclei and actin cytoskeletal structures align dependent, to some degree, on frequency of stretch, amount of stretch and integrated time of stretch(75). Control primary fibroblasts showed actin and nuclear alignment, but HGPS patient cells did not (**Figure 14**). Despite similar, high initial seeding densities between control and HGPS patient cells, there was substantial cell loss in the HGPS patient cells under stretch, likely due to cell death or detachment possibly due to the inability to adapt under force. Given the nearly complete lack of alignment as well as the heterogeneous shape of the HGPS cells (**Figure 14**) it was difficult to quantify the lack of alignment in the HGPS sample.

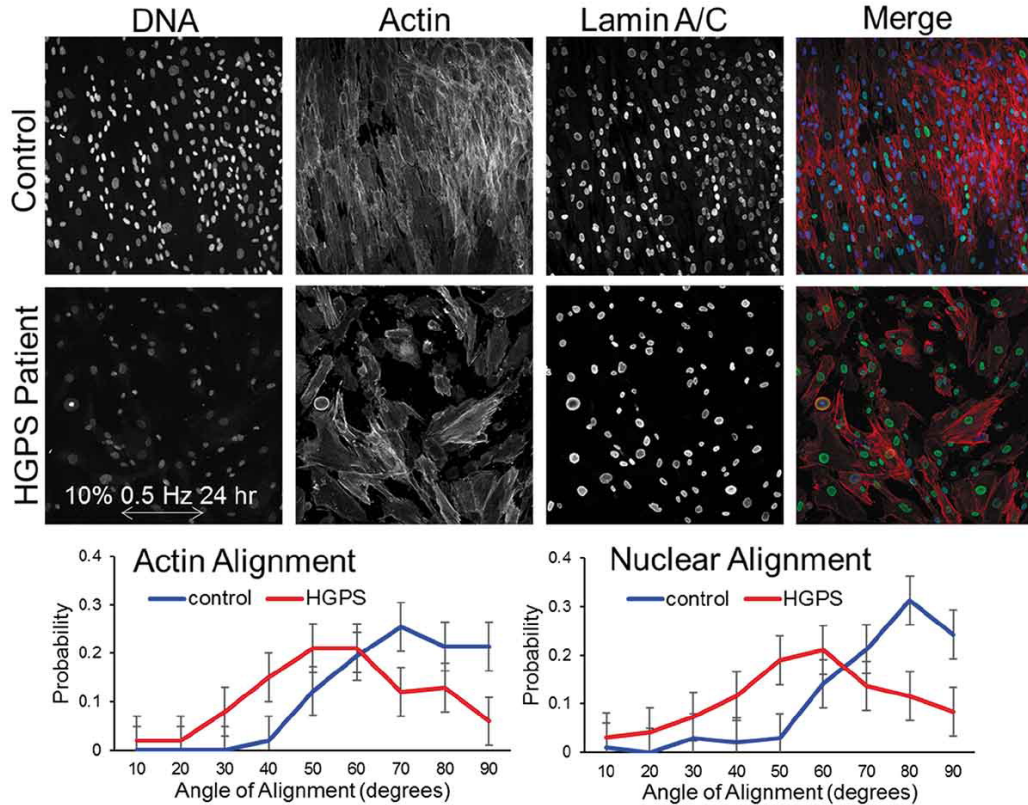


Figure 14: HGPS patient fibroblasts do not align under uniaxial stretch. Fibroblasts from a patient with HGPS or parent control were grown on deformable substrates and stretched at 0.5 Hz for 10% for 24 hr. Control cells showed characteristic orthogonal alignment to the applied stress with both actin and nuclei reorienting perpendicular to the direction of the stress. HGPS patient cells showed no particular alignment patterns. Comparatively, cell and nuclear shapes were also heterogeneous and irregular. Quantification ($n > 100$ cells per condition) shows alignment of actin fibers and nuclei preferentially 90° from the direction of stress. HGPS cells show mostly random distribution with some preference for 40° - 70° distributions, but these are skewed by drastic cell shape differences. Error bars reflect sample size by Fisher's exact method.

3.4. DISCUSSION

Nuclei in cells from patients with HGPS can exhibit protrusion of the nucleus toward the cytoplasm (11) as well as many other gross nuclear morphological changes (8,14). There are many structural changes associated with HGPS including reduced lamin B1 levels(76), loss of heterochromatin(12), changes in chromatin-lamin binding(77) ,altered lamin-nuclear envelope association(78), altered nuclear pore complex(79) and changes in how the nucleus binds to the cytoskeleton(25). Here, we have tried to examine lamina-specific defects through different cellular manipulations of cells exogenously expressing progerin. Of note by our group and others is that the exogenous expression of progerin, by plasmid such as DsRed-progerin or virus such as HA-progerin, is not the same as HGPS. Defects that result from exogenous expression appear to be more severe from the higher expression levels (7). However, the physical model we propose here is entirely consistent with the force-induced wrinkling behavior observed in nuclei from patients with HGPS (8). In previous studies, micropipette aspiration of isolated nuclei from patients shows wrinkling under high stress that is independent of the direction of applied force (8). Thus, it appears that this model would hold with endogenous expression as well as with exogenous expression.

Several other lamin and nuclear envelope mutations are associated with nuclear dysmorphisms(27), and the term ‘blebbing’ has been used to categorize most of these altered shapes(80). Although progerin-induced lamin misalignment may be due to altered signaling, it might not be mutually exclusive. We suggest here that the unique aspects of the nuclear shape changes – outward blebbing seen in some nuclear defects(81) versus the folds observed in HGPS – are likely significant markers of the etiology of this mechanical dysfunction. We suggest that the phrase blebbing should be used exclusively for an increase in the size of the nuclear envelope

and an outward distention of a particular region of the nucleus. Thus, models developed for other nuclear blebs as outward protrusions and dilations may not necessarily be applied to progeria(82, 83). However, ‘traditional’ outward nuclear blebs have been observed in nuclei from progeria patients (11), which may be a function of passage time and other cellular factors suggesting numerous lamina failure mechanisms.

Micro-aggregate model of the HGPS nuclear lamina

The energy of bending for an elastic two-dimensional surface that bends into a third dimension can be calculated based on previous works by Israelachvili(84). Lamina networks are mostly elastic(85–87), and weak bending is a type of deformation that costs significantly less energy than stretching. The bending modulus, κ , of a general single elastic sheet is defined

$$\text{according to: } \kappa = \frac{1}{12} K_{stretch} h^2$$

where h is thickness and is the $K_{stretch}$ dilation modulus (37). For the lamina of progerin-expressing cells, the $K_{stretch}$ would increase (8) and the local thickness, h , of the lamina increases significantly with progerin accumulation, as has been shown by electron and light micrographs (8,11). Thus, κ would be much higher for progerin-expressing cells over control cells.

Micropipette aspiration has confirmed the increased stiffening of the lamina nuclei from cells exogenously expressing progerin (7) in addition to nuclei from patients with HGPS measured by micropipette (8) and by stretching (9).

The resulting energy, e_{bend} , to bend around a segment radius of curvature, R , can be described as

$$(37): e_{bend} = \frac{1}{2} \kappa \frac{1}{R^2}$$

Since nuclei in both control and progerin-expressing cells show wrinkles and invaginations (**Figure 10**), in many cases with progerin-expressing cells showing more wrinkles then we assume that R doesn't change or gets larger. Thus, if the energy required to bend the progerin lamina was much higher than a control lamina, then the deflections should be much smaller than control lamina. However, this is not the case. Another mechanism governing the wrinkling of the progerin lamina must be occurring.

Given the differential responsiveness on patterns (**Figure 10**) and this model prediction, we suggest in sum that the deformations in the lamina of progeria cells are driven by entirely or mostly different factors than those seen in control cells. In **Figure 15**, we summarize a model that conveys the mechanism that we suggest for the nuclear lamina wrinkles associated for progerin. For control cells, due to a uniform distribution of lamin, stress, and exogenous forces cause the nuclear lamina to become thinner due to the elastic properties of the lamina (40) and therefore results in a dilation of the lamina network and low intensity values at the site of applied force (Fig. 56). Conversely, progerin-expressing cells show microaccumulations of progerin and deformation occurs at these regions rather than at regions of applied force (**Figure 15(b)**). This model will always show high intensities of progerin associated with defects. **Figure 4** shows increased progerin intensity at the invaginations and **Figure 14** shows defects growing from regions of high intensity. Also, this model accounts for defects that occur in regions not necessarily associated spatially with the application of force (**Figures 8 and 10**), wrinkles not aligned with actin filaments), rather defects associate with the region of accumulation of progerin. This model is consistent with our simulations as well as the concepts of stiffened inclusions shown in many examples throughout materials science.

Previous models of blebs have suggested that the lamina is restorative and resistant to blebs (35, 36). Finite element analysis of an isotropic elastic two-dimensional sheet has predicted folds rather than blebs in shape bifurcation studies, but not at regions distinct from applied pressure(88). Also, the nature of intermediate filaments makes the lamina resistant to holes and defects from loss of local filament structure(89). However, as with the HGPS defects seen here, there may be unreparable damage to the lamina associated with overaccumulation.

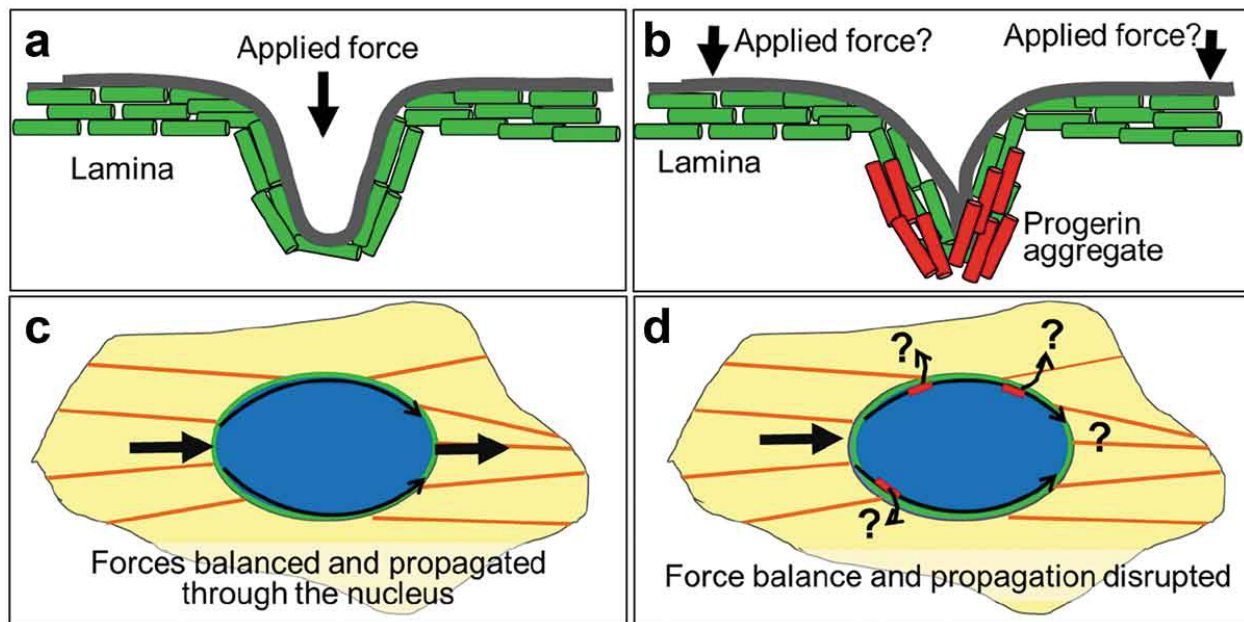


Figure 15: Model of nuclear lamina under force. (a) The nuclear lamina for control cells experiences a thinning of membrane and dilation of lamin A network. (b) The nuclear lamina for progerin-expressing cells experience high stress and buckle at the aggregates irrespective of force application. Wrinkles then emanate from the aggregate space. (c) In control cells cytoskeletal forces are balanced through the nuclear lamina and are propagated from one side of the nucleus to the other. (d) With wrinkles or defects in progerin-expressing cells forces may be disrupted along the lamina.

Implications in force transmission through the lamina and nucleus

One particularly important implication for the progerin-expressing nucleus would be structural integration of the cytoskeleton with the nucleoskeleton called the LINC (linker of nucleus to cytoskeleton) complex. The LINC complex is important in balancing forces throughout the cell and transmitting forces across the cell (**Figure 15(c)**)(90, 91). Severing the LINC complex prevents forces from being transmitted to the inside of the nucleus(92) and forces from being transmitted from one side of the cell to the other(93). It is unclear if LINC components are changed in HGPS cells. However, even if LINC complexes are maintained, we suggest that improper distribution of forces across the nuclear lamina from the non-isotropic distribution of lamins associated with progerin expression could modify the propagation of force throughout the cell (**Figure 15(d)**). This may be in-part why the wrinkles form away from the direction of the actin filaments in progerin-expressing cells (**Figures 10 and 12**). Thus, in HGPS premature aging, and in aspects of normal cellular aging(94), accumulated nuclear lamina defects may prevent proper force transmission through cells.

Our findings reveal that the abnormal nuclear morphology observed in HGPS and progerin expression is a consequence of both structure and mechanics. Excessive accumulation of progerin at the nuclear lamina causes wrinkles and invaginations observed in numerous cellular conditions. We suggest that these altered shapes are a result of microaggregates rather than just a uniform stiffening of the lamina.

CHAPTER 4: PROGERIN-EXPRESSING ENDOTHELIAL CELLS ARE UNABLE TO ADAPT TO SHEAR STRESS

Danielsson, B.E., H.C. Peters, K. Bathula, L.M. Spear, N.A. Noll, K.N. Dahl, and D.E. Conway. 2022. Progerin-expressing endothelial cells are unable to adapt to shear stress. Biophys. J. <https://doi.org/10.1016/j.bpj.2022.01.004>.

4.1. RATIONALE

The nuclear lamina, a fibrous lamin-protein network, located between the inner membrane of the nuclear envelope and chromatin, provides structural support for the nucleus and plays a major role in nuclear shape, gene regulation, as well as the assembly/disassembly of the nucleus during cell division (27–29, 95). Numerous studies have shown the mechanoadaptive and mechanoresponsive nature of the nuclear lamina under force (10, 14–16, 18).

Hutchinson-Gilford progeria syndrome (HGPS) is a rare premature aging disease in children caused by an autosomal dominant mutation in the *LMNA* gene, resulting in an aberrant form of lamin A termed progerin(58). The predominant mutation in HGPS involves a de novo point mutation (1824C>T), which activates a cryptic donor splice site resulting in an internal deletion of 50 amino acids. These amino acids include a cleavage site for ZMPSTE24, a protease that removes the farnesyl group from mature lamin A—loss of this cleavage site leads to the permanent farnesylation of progerin. Permanent farnesylation of progerin is thought to be the critical feature of HGPS, which is supported by the observation that ZMPSTE24 knockout mice phenocopy HGPS (96, 97). Similar to lamin A, progerin accumulates at the nuclear periphery. However, progerin expression has been shown to alter the nuclear lamina structure, and leads to several downstream nuclear defects, including: abnormal nuclear morphology, increased nuclear stiffness, redistribution of heterochromatin, modified nuclear pore structure, alterations in gene expression, and nuclear structural instability (41–43, 45, 98).

HGPS patients have accelerated atherosclerosis, leading to premature death as a result of heart attack and stroke (99). Cardiovascular alterations in HGPS patients are similar to atherosclerosis of aging individuals such as exhibiting hypertension, vascular stiffening and calcification, and plaque formation(100–102). Yet these patients do not experience traditional risk factors for atherosclerosis, such as hypercholesterolemia or increased serum levels of c-reactive protein(103). Thus, an important question is why and how progerin expression affects the vasculature to lead to rapid onset of atherosclerosis? One of the hallmarks of the disease is the loss of vascular smooth muscle cells (vSMCs) in large arterial vessels(104, 105). Several studies, using both iPSCs and HGPS mouse models have shown that expression of progerin in vSMCs impairs cell proliferation (106), impairs cell response to physiological levels of strain (stretch) (107, 108), reduces vasoreactivity (109), and accelerates atherosclerosis by inducing endoplasmic reticulum stress (110, 111).

In addition to vSMCs, progerin also alters endothelial cell function. Using a HGPS mouse model with progerin expression only in endothelial cells it was shown that this resulted in increased inflammation, impaired vascularization, and shortened life span(112). In a similar HGPS mouse endothelial model, it was observed that progerin-expressing endothelial cells caused cardiac pathologies, and that these endothelial cells had impaired mechanoresponsivity(113). We hypothesized that an important aspect of progerin expression in endothelial cells would be impaired mechanoadaptation to shear stress, which was suggested in a previous study(113). To investigate this hypothesis, we developed an HGPS model using human umbilical vein endothelial cells (HUVEC) expressing progerin, as well as HUVECs with ZMPSTE24 shRNA knockdown. Progerin-expressing cells, as well as ZMPSTE24 knockdown cells, failed to adapt to physiological levels of fluid shear stress, exhibiting cell loss at longer

timepoints of shear stress exposure. Cell loss was rescued by treatment with the farnesyltransferase inhibitor lonafarnib, DNA demethylase inhibitor methylstat, as well as pre-adaptation of cells to fluid shear stress prior to progerin expression. Collectively our results show that endothelial cells expressing progerin cannot adapt to the mechanical forces of fluid shear stress, which may be an important aspect of the rapid onset of atherosclerosis in HGPS patients.

4.2 METHODS

Cell Culture and Transfection

Commercially available primary human umbilical vein endothelial cells (HUVECs) (pooled, passages 3-5, Lonza, Basel, Switzerland) were grown in EGM-2 medium (Lonza, Basel, Switzerland). To express progerin in HUVECs, a previously described HA-tagged progerin adenovirus was developed(67).The lowest level of adenovirus that infected nearly 100% of cells was used. To overexpress wild-type lamin A in HUVECs, lamin A adenovirus (based on RefSeq BC014507) was purchased from Vector Biolabs and used at an identical titer level as progerin, as previously described(114).

shRNA Knockdown

To knockdown ZMPSTE24 the pLKO-1 vector was used (Sigma Aldrich, clone ID TRCN0000294124, target sequence TGGTAAGGCCAATGTTATTTA). Lentivirus was prepared using HEK 293 cells, with second generation packaging plasmids, pSPAX2 (Addgene 12260) and pMD2.G (Addgene 12259). HUVECs were transduced with lentivirus shRNA and

selected with puromycin (1 $\mu\text{g}/\text{ml}$). A non-targeting shRNA (Sigma SHC216) was used as a control.

Lonafarnib and Methylstat Treatment

HUVECs were treated with either 1.0 μM Methylstat (Sigma-Aldrich, SML0343), a histone demethyltransferase inhibitor or 0.5 μM Lonafarnib (Tocris, 6265), a farnesyltransferase inhibitor. HUVECs were treated with a daily dose of 1.0 μM Methylstat (Sigma-Aldrich, SML0343) for 48 hours. HUVECs were treated with a daily dose of 0.5 μM Lonafarnib (Tocris, 6265) for 72 hours.

Fluid Shear Stress

HUVECs were seeded onto ibidi chamber slides (ibidi-treated μ -slides I^{0.6}, cat #80186 or ibidi-treated μ -slides VI^{0.4}, cat#80606, Germany), coated with 60ng/mL fibronectin (Sigma-Aldrich, F1141). At 80% confluency, HUVECs were exposed to laminar or oscillatory shear stress using the ibidi pump system (ibidi, cat #10902, Germany), at 12 dynes/cm² for 1, 3, or 6 days with or without modifications perfused in the media.

Cell Fixation and Labelling

After fluid shear stress experiments were finished, HUVECs were washed two times with PBS and fixed for 10 min at room temperature with 4% paraformaldehyde in PBS. After three washes with PBS, the cells were permeabilized for 10 min at room temperature with 0.2% Triton X-100 in PBS and blocked with 5% BSA for 1 hour at room temperature. Cells were then incubated overnight at 4 degrees Celsius room temperature with the primary Ab diluted in blocking solution, using either anti-lamin A antibody (cat # sc-7292, Santa Cruz Biotechnology) for control cells, or anti-HA antibody (cat # 901501, Biolegend) for progerin-expressing cells

and anti-lamin B1 antibody (cat # ab16048, Abcam). Three more washes with PBS were then followed by incubation with the secondary Ab (Alexa Fluor 647-conjugated donkey anti-mouse IgG; Thermo Fisher) and stained with rhodamine phalloidin (cat # PHDR1, Cytoskeleton) for 45 min followed by three additional PBS washes. Samples were stained with Hoechst 33342 (ThermoFisher) and mounted with ibidi mounting medium (ibidi, cat #50001, Germany). For cell death assays, an apoptosis/necrosis Detection kit (abcam, ab176749) was used following the manufacturer's instructions. The same antibodies, as well as ZMPSTE24 (Novus, NB100-2387ss) and tubulin (Proteintech, mouse monoclonal), were used for Western Blotting quantification of overexpression and knockdown.

Quantification and Imaging Analysis

Samples were imaged on Zeiss LSM 710 confocal microscope at 20x and 63x. Image analysis was completed using Fuji Image J. We analyzed the progerin-expressing endothelial cell response to the force of shear stress by quantifying abnormally structured nuclear lamina (through lamin A, HA-progerin, and lamin B staining), nuclear lamina outward blebs (through lamin A and HA-progerin staining), and the presence or absence of micronuclei (through Hoechst staining). Cell loss was quantified using a cell counting macros on Image J.

Statistical Analysis

Statistical significance was measured using an unpaired, two-tailed student t-test for data containing two groups. For data involving more than two groups, the Analysis of Variance (ANOVA) test was performed in order to obtain the statistical analysis for the data sets concerned. A further comparison of the groups was performed using the Tukey (HSD) test to determine significant differences between groups. All statistical tests were conducted at a 5%

significance level ($p < 0.05$). Prism GraphPad was used for statistical analyses. N=3 denotes the number of times each experiment was done. Every experiment was completed 3 times, and between 5 and 10 images from each group was quantified.

4.3. RESULTS

Endothelial cells expressing progerin or overexpressing wild-type lamin A are unable to adapt to shear stress

Previous work has shown that HGPS cells exhibit both a combination of a stiffened nucleoskeleton and a softened nuclear interior,(42) which in turn can cause mechanical irregularities and impaired mechanoadaptation (42, 114). We therefore sought to understand how progerin expression would affect endothelial cell responses to fluid shear stress, the frictional drag force created by blood flow. We expressed progerin in HUVECs using an adenovirus, and as a control we also examined the effects of overexpression (OE) of wild-type lamin A. HUVECs expressing either progerin or overexpressing wild-type lamin A had a significant decrease in cell count after 72 hours of arterial levels of shear stress (12 dynes/cm²) (**Figure 16 (A & B)**). Western blotting was used to confirm both lamin A and progerin overexpression [**Figure 16 (C)**], which was similar to prior published findings (114). Interestingly there was minimal cell loss for both groups at 24 hours of shear stress, indicating that cell loss is not a rapid event and detachment would not be the cause for the cell loss. Non-transduced control cells had no cell loss and were able to characteristically align in the direction of shear stress. Additionally, no cell loss was observed for progerin-expressing or lamin A OE HUVECs when grown in static culture (0-hour images), indicating that fluid shear stress is necessary for cell loss. Additionally, we examined surface expression of phosphatidylserine as a

marker of apoptosis. Progerin-expressing HUVECs had a substantial number of cells with surface expression of phosphatidylserine when exposed to 24 hours of shear stress (**Figure 16 (D)**), suggesting that apoptosis is occurring prior to cell loss.

As an alternate approach to model HGPS in endothelial cells we developed HUVECs in which ZMPSTE24 was knocked down by shRNA. Densitometry analysis of Western blot (**Figure 16 (G)**) showed that the cells with ZMPSTE24 KD had 40% less ZMPSTE24 than the shRNA control. ZMPSTE24 is a protease involved in post-translational cleavage of farnesylated prelamin A. Loss of ZMPSTE24 leads to the accumulation of farnesylated lamin A and phenocopies features of HGPS (96, 97). HUVECs with knockdown of ZMPSTE24 showed increased nuclear wrinkles and also experienced similar cell loss when exposed to shear stress, (**Figure 16 (E & F)**). To see if oscillatory flow would cause more cell death events in the progerin-expressing cells we exposed the HUVECs to 12 dynes/cm² of laminar and oscillatory shear stress. No significant difference in cell loss was observed between the different flow types (**Figure 16 (H & I)**). Taken together, these results show overexpression of lamin A or the expression of progerin, can affect the ability of endothelial cells to adapt to the forces of fluid flow.

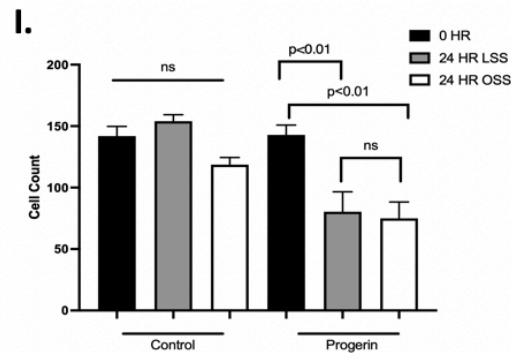
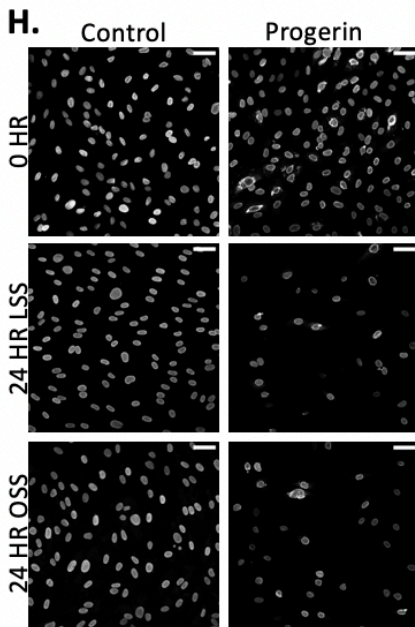
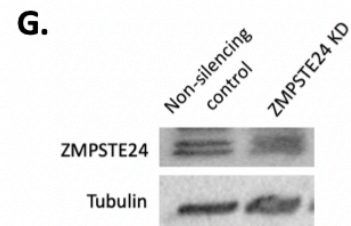
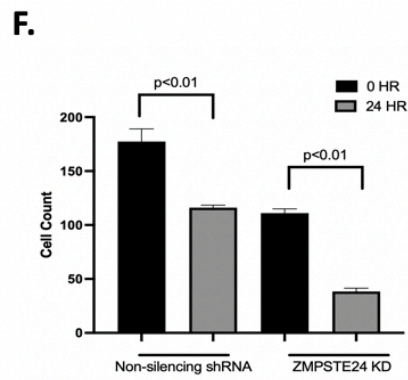
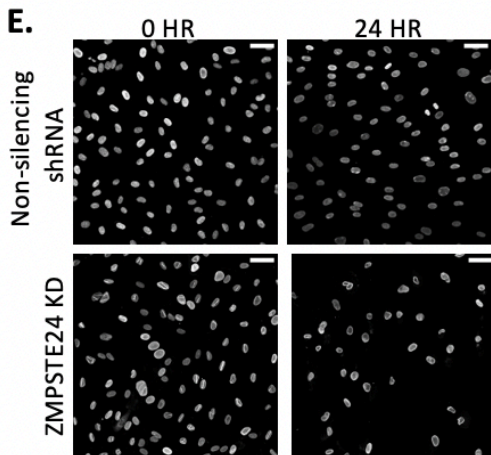
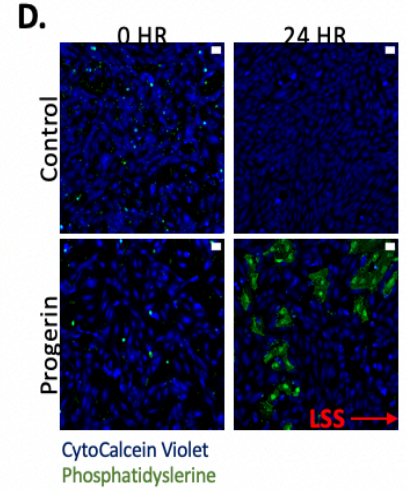
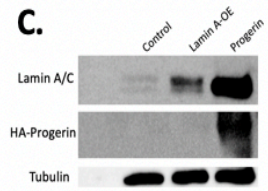
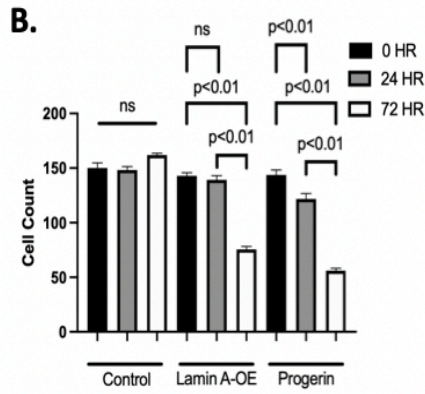
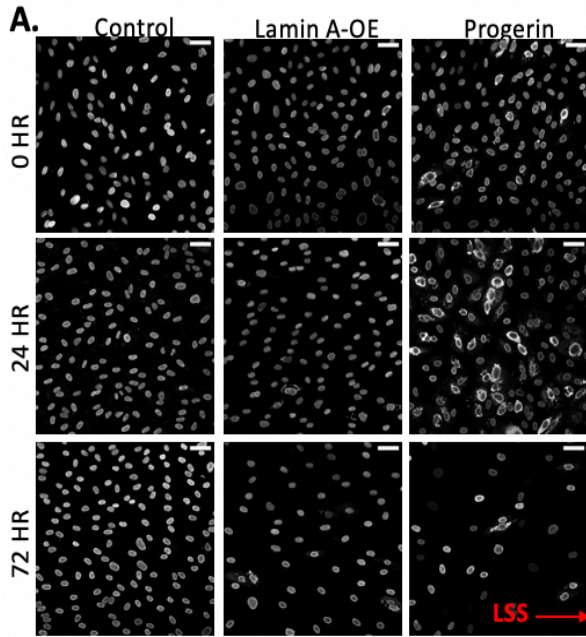


Figure 16: Progerin expression causes cell loss in HUVECs under laminar shear stress.

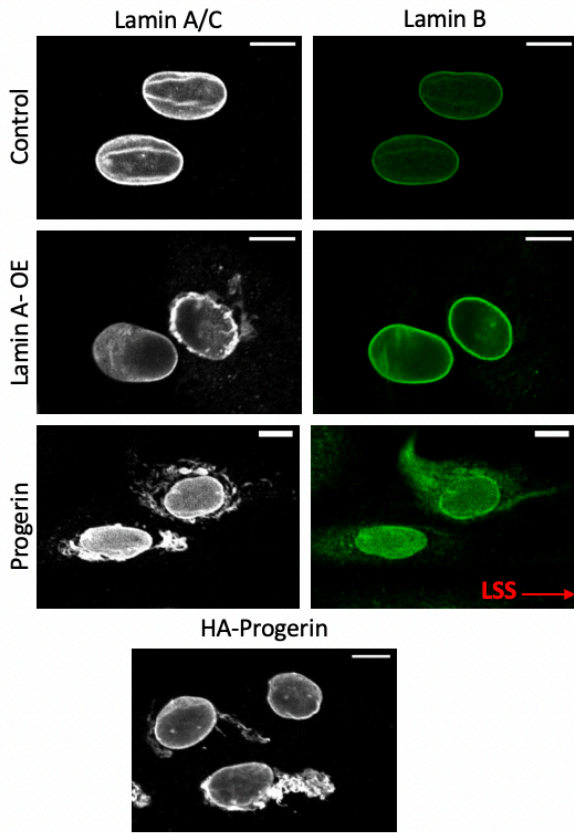
Confocal images taken at 20 \times . Scale bar, 50 μ m. Arrow represents direction of fluid shear stress at 12 dynes/cm². LSS, laminar shear stress; OSS, oscillatory shear stress. HUVECs stained with HA-progerin (Progerin), laminA/C (Lamin A-OE, Control, ZMPSTE24, nonsilencing shRNA). Ordinary one-way ANOVA. N = 3. **(A)** Cell loss in progerin-expressing HUVECs under laminar shear stress for 0, 24, and 72 h. **(B)** Cell count for HUVECs under laminar shear stress for 0, 24, and 72 h. **(C)** Western blot for protein expression of HA-progerin, lamin a/c and tubulin. **(D)** Progerin-expressing cells undergo apoptosis under 24 h of laminar shear stress. **(E)** Cell loss in ZMPSTE24 KD HUVECs under laminar shear stress for 0 and 24 h. **(F)** Cell count for ZMPSTE24 KD HUVECs under laminar shear stress for 0 and 24 h. **(G)** Western blot for ZMPSTE24 and tubulin showing the knockdown of ZMPSTE24 in HUVECs. **(H and I)** No difference was observed between 24 h of oscillatory and laminar shear forces in progerin-expressing HUVECs. Images taken with confocal microscope at 10 \times . Scale bar, 50 μ m. A cell death assay showed progerin-expressing HUVECs under 24 h of laminar shear stress experience apoptosis, indicated by the presence of the phosphatidylserine, an apoptotic marker.

Progerin-expressing endothelial cells have increased nuclear abnormalities in both static and shear conditions

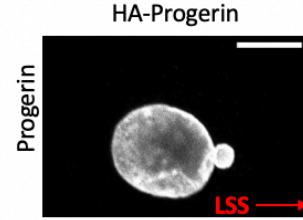
Progerin-expressing HUVECs under both flow (**Figure 16(A)**) and static conditions displayed exaggerated nuclear morphologies. Previous work as shown that the lamina in HGPS cells has a significantly reduced ability to rearrange under mechanical stress (8). We quantified nuclear abnormalities (including dysmorphic nuclear lamina, outward blebs, and micronuclei) in

progerin-expressing HUVECs under shear stress and static conditions, and compared results to control and the lamin OE groups. Consistent with prior observations in non-endothelial cell types, nuclear abnormalities were present in progerin-expressing endothelial cells. **Figure 17(A)** shows the examples of dysmorphic nuclear lamina in both progerin-expressing and lamin OE cells. In the progerin-expressing cells we also observed disruptions in lamin B structure. We also examined the incidence of outward blebs (**Figure 17 (B)**) and micronuclei (**Figure 17 (C)**). Quantification of dysmorphic nuclear lamina, outward blebs, and micronuclei showed similar levels of occurrence both under shear stress (**Figure 17 (D)**) and static culture conditions (**Figure 17 (E)**) for progerin expressing cells.

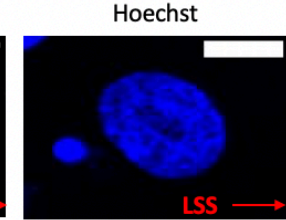
A. Dysmorphic Nuclear Lamina



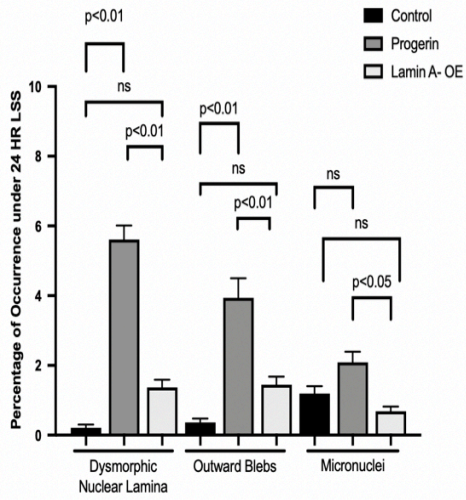
B. Outward Blebs



C. Micronuclei



D.



E.

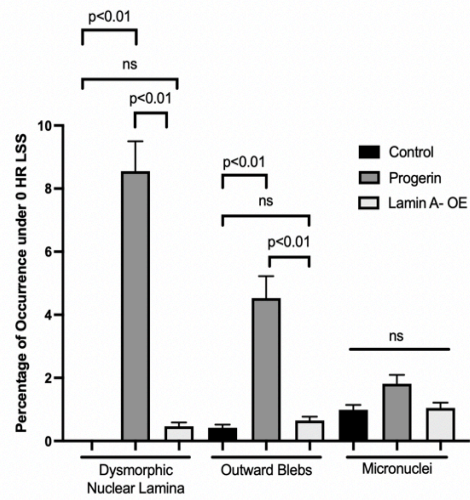


Figure 17: Laminar shear stress causes nuclear envelope disruption in Progerin-expressing HUVECs. Confocal images taken at 20×, 40×, and 63×. Scale bar, 10 μm. Arrow represents the direction of fluid shear stress at 12 dynes/cm². LSS, laminar shear stress. HUVECs HA-progerin (HA, lamin B, lamin A/C, and Hoechst stained), control, and lamin A-OE (lamin A/C, lamin B, and Hoechst stained). Ordinary one-way ANOVA. N = 3. **(A)** Dysmorphic nuclear lamina characterized by abnormal structure of lamin a/c, HA-progerin and lamin B staining in progerin-expressing HUVECs under 24 h of laminar shear stress. **(B and C)** Lamin A/C blebs and micronuclei was observed in progerin-expressing cells after 24 h of shear stress. **(D)** Quantification of nuclear abnormalities in 24-h laminar shear stress condition. **(E)** Quantification of nuclear abnormalities in static (0 HR shear stress) condition.

Lonafarnib rescues cell loss and nuclear envelope dysmorphia in progerin-expressing HUVECs under shear stress

In progerin-expressing cells, the attachment of farnesyl groups causes the nuclear envelope to have lobes instead of a round shape. This lobulation of the nuclear envelope is due to accumulation of progerin within the nucleus and dramatically changes the nuclear architecture as well as its stability (102). Previously it has been shown that the farnesyltransferase inhibitor (FTI) Lonafarnib can be used to prevent progerin accumulation and improve nuclear shape (66), and is currently used in clinical trials as a treatment for HGPS. To inhibit farnesylation of lamin A, ZMPSTE24 KD and progerin-expressing HUVECs were treated with Lonafarnib for 72 hours.

These treated cells were then subjected to 24 hours of laminar shear stress. We hypothesized that inhibiting progerin farnesylation would improve the ability of these cells to adapt to shear stress. Our results showed that Lonafarnib significantly prevented cell loss the ZMPSTE24 KD cells (**Figure 18 (A & B)**) but did not lead to a significant improvement in the progerin-expressing cells. Furthermore, the results showed that Lonafarnib treatment prevented nuclear envelope disruptions in the HA-progerin expressing cells exposed to shear stress (**Figure 18 (C & D)**). Taken together, these improvements show the effects of Lonafarnib on cell loss after exposure to fluid shear stress, suggesting Lonafarnib enhances the ability of cells to respond and adapt to changes in mechanical forces.

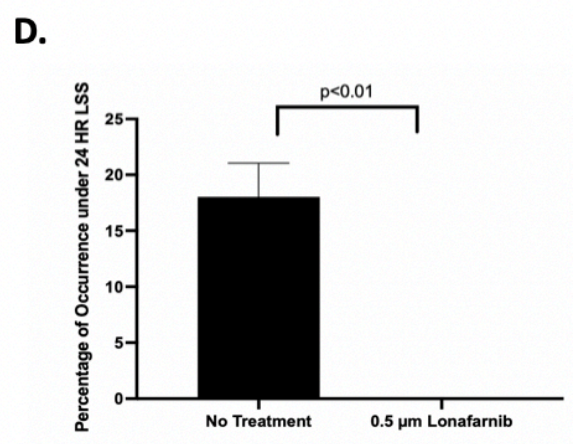
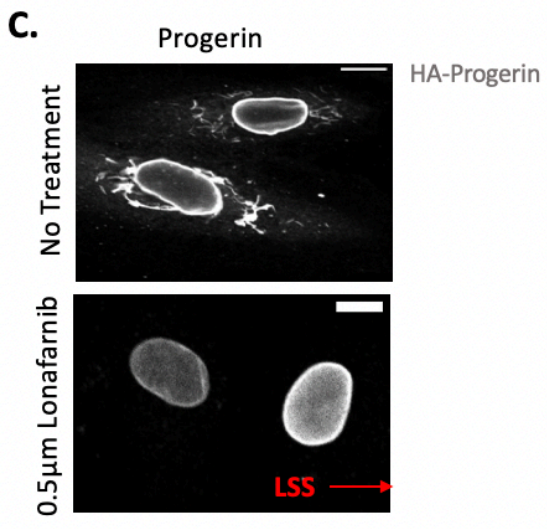
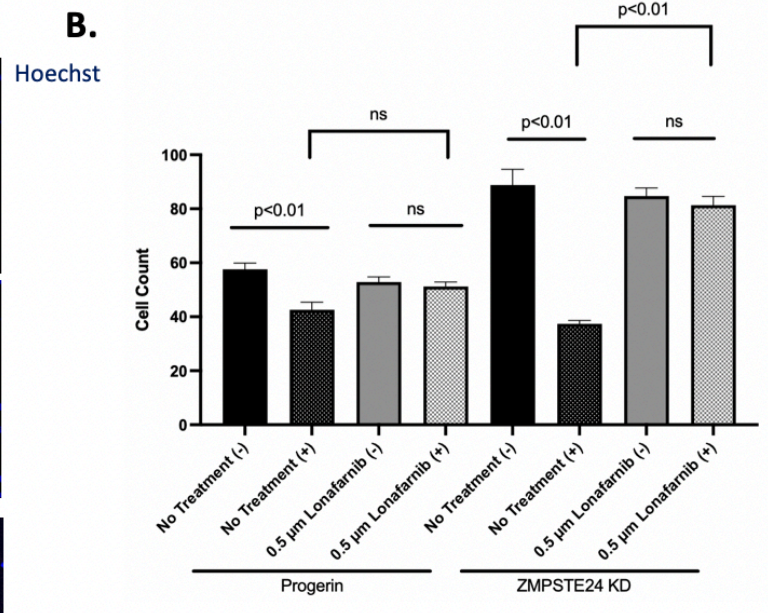
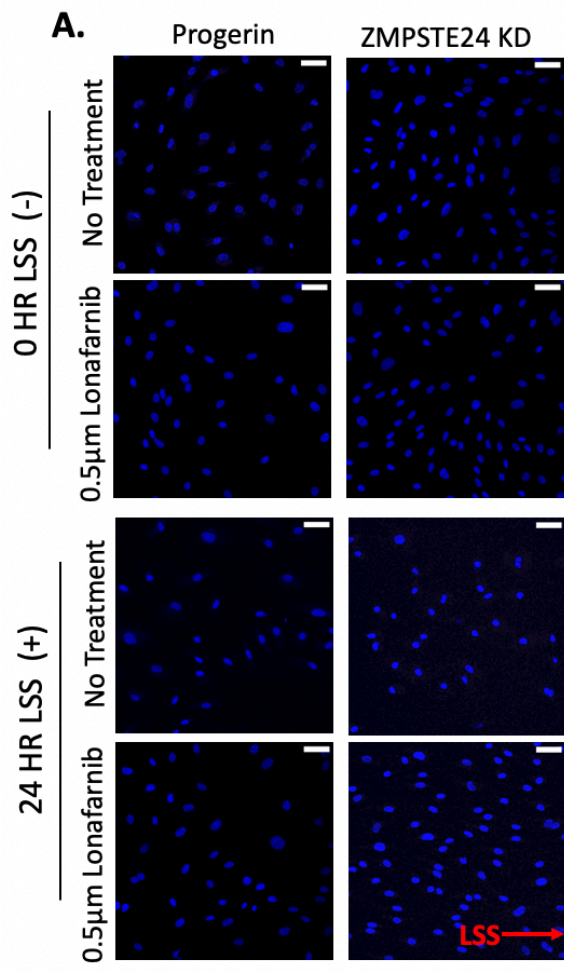


Figure 18: Lonafarnib rescues cell loss and nuclear envelope disruptions in progerin-expressing HUVECs under shear stress. Confocal images taken at 20× and 40×. Scale bar, 50 μm. Arrow represents direction of fluid shear stress at 12 dynes/cm². LSS, laminar shear stress. HUVECs progerin and ZMPSTE24 KD cells stained with HA-progerin and Hoechst N = 3. HUVECs were treated with a daily dose of 0.5 μM lonafarnib (Tocris, 6265) for 72 h and then exposed to laminar shear stress for 24 h. **(A and B)** Lonafarnib rescues cell loss in ZMPSTE24 KD cells under 24 h of shear stress compared to static group (0 h). Ordinary one-way ANOVA. N = 3. **(C and D)** Lonafarnib rescues nuclear envelope disruptions in progerin-expressing HUVECs under shear stress. Unpaired *t* test. N = 3.

Methylstat rescues cell loss in progerin-expressing and ZMPSTE24 KD HUVECs under shear stress

It has been previously shown that progerin-expressing cells have alternations in histone modifications, including: a loss of peripheral heterochromatin, reduced levels of H3k9me3 and increased levels of trimethylation of H4K20, an epigenetic mark for constitutive heterochromatin on H4 (45). Notably, pharmacological-induced increases in heterochromatin have been shown to rescue nuclear morphology in a HGPS patient cells (115). To examine if increases in heterochromatin would improve the ability of progerin-expressing endothelial cells to adapt to shear stress, we used the drug methylstat, an inhibitor of histone trimethyl demethylases. ZMPSTE24 KD and progerin-expressing HUVECs were treated with Methylstat for 72 hours and exposed to 24 hours of laminar shear stress. Cell loss (**Figure 19 (A & B)**) and nuclear envelope disruptions were prevented (**Figure 19 (C & D)**) in cells treated with Methylstat. Taken together, these results show that increases in DNA methylation in progerin-expressing endothelial cells rescue nuclear morphology and ability to adapt to shear stress.

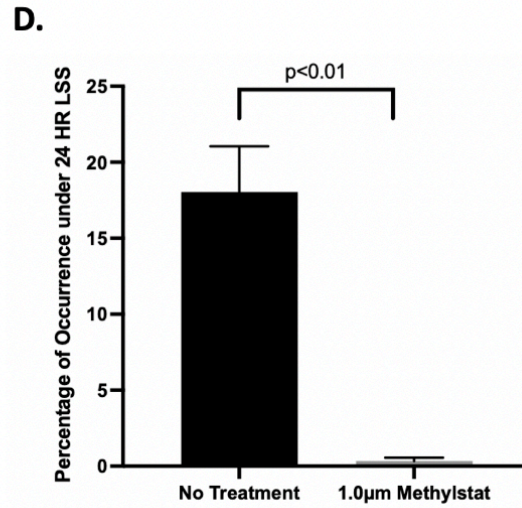
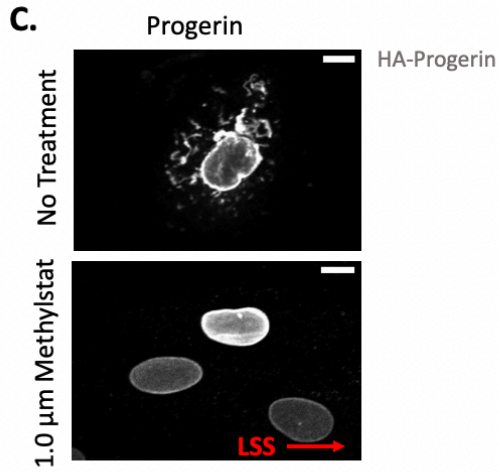
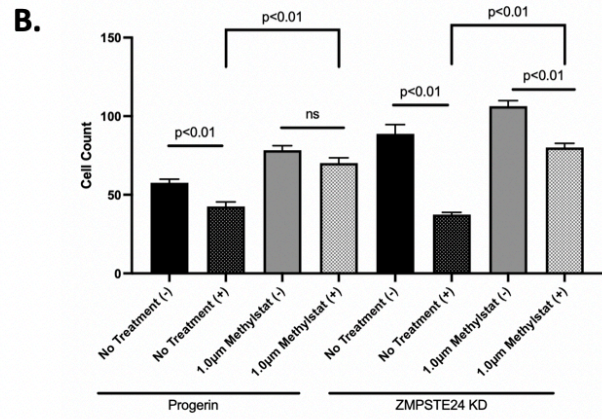
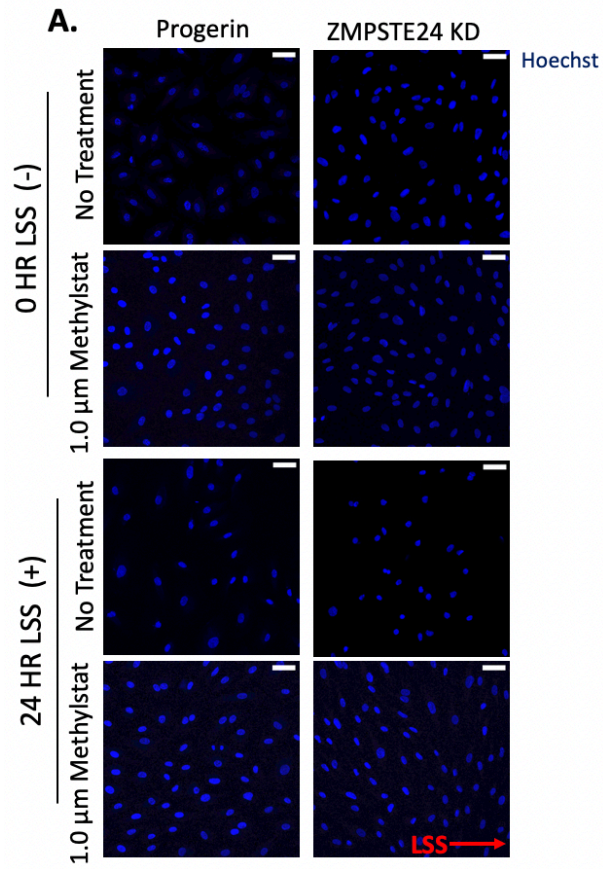


Figure 19: Methylstat rescues cell loss in Progerin-expressing HUVECs and ZMPSTE24 KD cells under shear stress. Confocal images taken at 20× and 40×. Scale bar, 50 μm. Arrow represents direction of fluid shear stress at 12 dynes/cm². LSS, laminar shear stress. HUVECs progerin and ZMPSTE24 KD cells stained with HA-progerin and Hoechst N = 3. HUVECs were treated with a daily dose of 1.0 μM methylstat (Sigma-Aldrich, SML0343) for 48 h and then exposed to fluid flow. **(A and B)** Methylstat rescues cell loss in progerin-expressing HUVECs, as well as in ZMPSTE24 KD HUVECs, under shear stress compared to the static group (0 h). Ordinary one-way ANOVA. N = 3. **(C and D)** Methylstat rescues nuclear envelope disruptions in progerin-expressing HUVECs under shear stress. Unpaired *t* test. N = 3.

Pre-alignment of progerin-Expressing HUVECs prevents cell loss under shear stress

We hypothesized that progerin-expressing endothelial cells which did not have to undergo cellular and nuclear shape changes would be less affected by exposure to shear stress. To investigate how progerin expression would affect aligned endothelial cells, we first exposed non-transduced HUVECs to shear stress for 72 hours to induce alignment. Afterwards, these cells were then transduced with progerin or a control adenovirus (GFP), and exposed to an additional 72 hours of shear stress. Our results showed that progerin expression in pre-aligned cells (**Figure 20 (A)**) resulted in reduced cell loss (**Figure 20 (C)**) and nuclear envelope disruptions (**Figure 20 (D)**) when compared to progerin-expressing cells not adapted to shear stress (**Figure 20 (B)**).

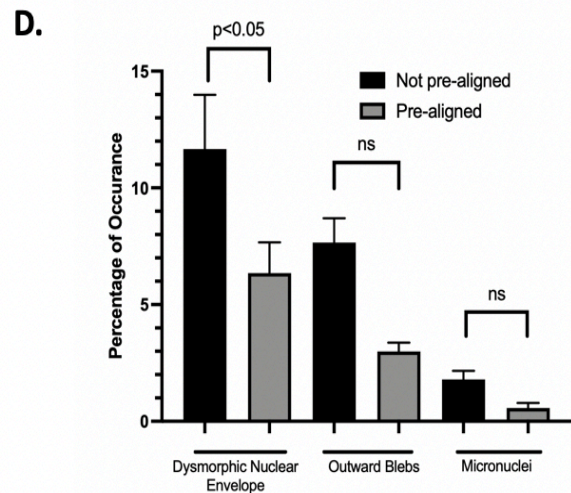
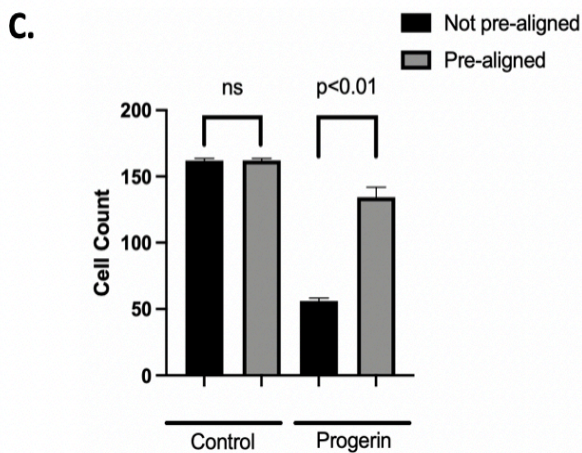
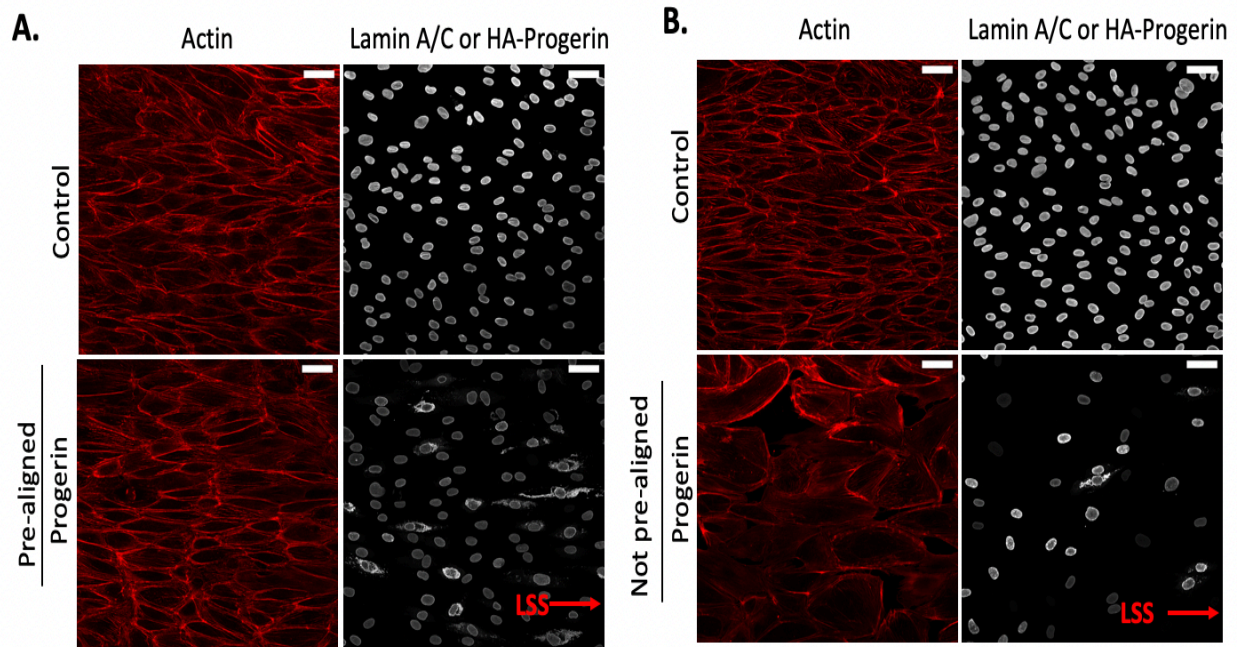


Figure 20: Prealignment of Progerin-Expressing HUVECS prevents cell loss under shear stress. Confocal images taken at 20 \times . Scale bar, 50 μ m. Arrow represents direction of fluid shear stress at 12 dynes/cm². LSS, laminar shear stress. HUVECS stained with HA-progerin and control stained with lamin A/C. Both groups stained with Phalloidin. Ordinary one-way ANOVA. N = 3. **(A)** HUVECS were exposed to shear stress for 3 days and once actin alignment

(actin fibers oriented parallel to the applied direction of force) and nuclear remodeling was observed (nuclear shape appeared to have changed from more circular to more elongated) progerin expression was induced and the cells were exposed to shear stress of an additional 3 days. **(B)** Progerin-expressing HUVECs (cells treated with progerin adenovirus 24 h before shear) and the control groups were exposed to shear stress for 3 days total. When progerin was induced after actin and nuclear remodeling had occurred, cell loss **(C)** and nuclear envelope disruptions were prevented **(D)**.

4.4. DISCUSSION

In this work we developed an *in vitro* model of HGPS endothelium by 1) expressing progerin and 2) knockdown of ZMPSTE24 in HUVEC. In our model, the expression of progerin could be higher than what is observed in HGPS patients. Even if the expression of progerin were above physiological levels, it may still be relevant given evidence that progerin expression increases over time, even in healthy cells(116). Additionally, we also assume that knockdown of ZMPSTE24 serves as an additional approach which may result in a more modest, and potentially philological level of progerin. With either progerin overexpression or ZMPSTE24 knockdown HUVEC exhibited characteristic progerin-induced changes in nuclear morphology, indicating that the endothelial cell is sensitive to progerin expression. Strikingly, application of fluid shear stress resulted in dramatic cell loss, occurring between 1-3 days of fluid shear stress **(Figure 16)**. Interestingly, pre-alignment of endothelial cells to fluid shear stress prior to expression of progerin **(Figure 20)** prevented the cell loss, suggesting that progerin-expression prevents the ability of endothelial cells to adapt to changes in mechanical forces, but has less of an effect in cells already adapted and aligned to shear stress.

Although a number of prior studies have focused on the effects of progerin in fibroblasts and vascular smooth muscle cells(105, 110, 117–120), our results add to growing evidence that the endothelium is also sensitive to progerin expression (112, 113, 121), including a recent study showing that progeria endothelial cells exhibit altered response to shear stress (122). Although two prior mouse models expressing progerin in the endothelium did not report dramatic loss of endothelial cells (112, 113), our finding that pre-aligned cells are less sensitive to progerin expression suggests that progerin expression may be most significant when endothelial cells are required to adapt to changes in mechanical environments. Supporting this hypothesis *Sun et al* showed that there was defective neovascularization of progerin-expressing endothelial cells in response to ischemia (112). Additionally, *Osmanagic-Myers et al* showed impaired endothelial alignment in response to short-term (3 hours) fluid shear stress (113). Loss of endothelial cells is especially significant in the context of HGPS early onset atherosclerosis, as endothelial dysfunction and damage is considered an initial step in the onset of atherosclerosis(123). Recently, *Pitrez et al*, showed HGPS patient-derived vSMCs cultured under arterial flow conditions detached from a microchip after a few days of culture and that this process is mediated by the upregulation of the enzyme metalloprotease 13 (124).

We showed that two pharmacological treatments previously shown to improve HGPS nuclear morphology in epithelial and fibroblast cell lines, lonafarnib (farnesyltransferase inhibitor)(125) and methylstat (inhibitor of histone trimethyl demethylases) (115) also restored normal nuclear morphology to progerin-expressing endothelial cells (**Figures 18 and 19**). Interestingly increasing chromatin methylation with methylstat significantly improved the ability of progerin-expressing endothelial cells to adapt to fluid shear stress (**Figure 19**). However, lonafarnib did not rescue cell loss for progerin-expressing cells (but did rescue ZMPSTE24 knockdown cells).

This result may be in part due to differences in the level of progerin expression, which may be lower in the ZMPSTE24 knockdown cells. Thus, improvements in nuclear morphology did not uniformly result in improved mechanoadaptation to shear stress.

An unanswered question in our work is the specific biochemical or physical mechanisms that account for the loss of progerin-expressing cells under fluid shear stress. Cell loss could be a direct result of increased apoptosis under shear stress (**Figure 16 (D)**). Related, prior work by *Bidault et al* showed progerin-expressing in endothelial cells have increased markers of DNA damage as well as upregulation of p53 and p21 which induce cellular senescence(121). The reasons for increased apoptosis are not yet known. One possibility is that apoptosis may result from the inability of progerin expressing cells to remodel their nucleus to adapt to shear stress. Nuclear circularity, elongation, and area rapidly change upon exposure to shear stress(47), suggesting that the nuclear lamina must undergo remodeling. Interestingly impaired lamin A phosphorylation has been observed in HGPS iPS-MSCs (126). Since lamin A phosphorylation is associated with the ability of the nuclear lamina to remodel, it is possible that the impaired lamin A phosphorylation prevents the progerin lamina from remodeling. Our results showing minimal effects of progerin-expression in pre-aligned cells (**Figure 20**) supports this remodeling hypothesis.

We define cell loss as the decrease in cell count from the start of shear stress (0 hour group). In addition to apoptosis, cell loss could be the result of slower proliferation or mechanical instability. Prior work has shown that cells expressing progerin proliferate slower(127); however given that cells were seeded at confluence proliferation is not expected to be a major contributing factor to cell count. Cell detachment, perhaps as a result of weakened focal adhesions or cell-cell adhesions, could be a cause for the decreased cell count. Our group recently published work

showing that the LINC complex is a necessary structure in endothelial cell mechanoadaptation, in which we observed that disruption of the LINC complex resulted in rapid loss of cells under fluid shear stress (<24 hours), due in part to impaired cell-substrate attachment (128). We do not believe the progerin-expressing cells have weaker or impaired attachment to the substrate, as we observed no cell loss or detachment in static culture, as well as minimal cell loss after one day of shear stress.

Interestingly, we observed that similar levels of cells were lost under shear stress when wild-type lamin A was overexpressed as compared to progerin expression (**Figure 16(A)**). However, lamin A overexpressing cells had significantly less dysmorphic nuclear lamina and blebbing when compared to progerin expressing cells (**Figure 17(D)**). Thus, changes in nuclear morphology do not completely account for the cell loss or an inability to adapt to shear stress. Overexpression of lamin A has been shown to increase nuclear stiffness(129), similar to progerin expression(42). It is therefore tempting to speculate that stiffer nuclei are less able to adapt to changing mechanical forces. Prior work has shown that there are substantial changes in nuclear shape and stiffness when endothelial cells adapt to shear stress (130), indicating that the nucleus undergoes significant remodeling to adapt to shear stress.

This work highlights the nuclear lamina as a critical feature for endothelial adaptability to fluid shear stress. We hypothesize that other factors that control nuclear stiffness beyond nuclear lamins, such as chromatin stiffness, may also impact how readily endothelial cells adapt to shear stress. We also note that aging can induce similar nuclear phenotypes to HGPS, including expression of progerin, increased nuclear stiffness, and altered nuclear morphology(131). An important question will be to determine if aging-associated changes in nuclear stiffness similarly impair endothelial cell adaptation to mechanical forces.

CHAPTER 5: CHROMATIN CONDENSATION REGULATES ENDOTHELIAL CELL ADAPTATION TO SHEAR STRESS

Danielsson, B.E., Tieu, K.V., Spagnol, S.T., Vu, K.K., Cabe, J.I., Raisch, T.B., Dahl, K.N., Conway, D.E. Chromatin condensation regulates endothelial cell adaptation to shear stress. Submitted to MBoC. February 28, 2022.

5.1. RATIONALE

Structures within the nucleus, including chromatin, lamins and other genomic elements, are highly adaptable and can assume various structural morphologies. Epigenetic changes to the chromatin, such as acetylation and methylation of histones, alter compaction and configuration(132). Decondensed chromatin has been shown to have heightened mobility, reduced stiffness and is frequently associated with gene-rich regions of euchromatin (133, 134). In contrast, condensed chromatin exists as a more compacted structure, frequently associated with gene-poor regions of heterochromatin (135–138). Changes in chromatin compaction can modulate overall nuclear shape, volume, and stiffness(115, 139, 140). Mechanical measurements of the nucleus have shown that the viscoelastic nature of chromatin acts as the dominant mechanical element of the nuclear interior when a nucleus deforms under high strain(141, 142).

Vascular endothelial cells (EC) are continually exposed to mechanical forces as a result of blood flow, which include both fluid shear stress and cyclic stretch. Both *in vivo* and *in vitro* studies of EC responses to fluid shear stress have shown that athero-protective shear stress (unidirectional laminar shear stress-LSS) induces a cellular response in EC whereby cells adapt to the forces of fluid flow by aligning both the EC nucleus and actin filaments in the direction of flow. However, EC exposed to athero-prone shear stress (multi-directional, oscillating shear

stress-OSS), this alignment response does not occur, with random orientation of cellular alignment. The alignment EC to shear stress is considered to be an important aspect of cellular adaptation to fluid shear stress, and is frequently correlated to differences in gene expression and inflammatory markers(143).

Previous publications have studied epigenetic changes for endothelial cells exposed to fluid shear stress (144–152). It has been shown that OSS induces expression of DNA methyltransferases (DNMTI) (147, 153), as well as up-regulates histone deacetylases (HDACs)(150, 152) in comparison to LSS both *in vivo* and *in vitro*. A major focus of these studies has been how epigenetic changes affect gene expression. However, it remains possible that these epigenetic changes can also affect the mechanical state of the nucleus. Prior studies have shown that direct force generated on cells influences chromatin organization(92, 154–156). Additionally, these nuclear mechanical changes may not only affect how cells sense and respond to mechanical forces but may also be a critical aspect in the prevention of DNA damage(2, 157, 158). For example, *Nava et al.* showed, in an epithelial stretch model, that adaptations in chromatin architecture and rheology are required to prevent DNA damage in cells exposed top mechanical force(159).

We hypothesized that chromatin condensation could represent an important aspect for how EC adapt to and align in the direction of shear stress. By examining changes in epigenetic histone markers, we identified H3K9ac, H3K27me₃, and H3K9me₃ as sensitive to fluid shear stress, indicating that there are substantial changes in chromatin acetylation and methylation in cells adapted to either athero-protective or athero-prone shear stress. We also show that increasing histone acetylation increases the speed by which EC align to fluid shear stress,

whereas increasing histone methylation inhibited EC alignment to fluid shear stress. Lastly, by measuring γ H2AX foci, we show that DNA damage in response to fluid shear stress is sensitive to changes in chromatin condensation. Taken together, our data identify chromatin condensation as an important biophysical parameter for EC adaptation to fluid shear stress.

5.2. METHODS

Cell Type

Commercially available primary Human Umbilical Vein Endothelial Cells (HUVEC) (pooled, passages 3-5, Lonza, Basel, Switzerland) grown in EGM-2 medium (Lonza, Basel, Switzerland) was used for all experiments.

Chromatin Condensation Modifications

For epigenetic modifications, HUVEC were treated with histone deacetylase inhibitor, 100nM Trichostatin A (TSA) (Cayman Chemical Company), to increase euchromatin, and a histone demethyltransferase inhibitor, 2.5 μ M Methylstat (Sigma Aldrich), to increase heterochromatin. In addition, we also used 50ng/mL-100ng/mL VEGF (Peprotech) for 24 hours for shear experiments, and 1-2.5 hours for FLIM experiments.

Fluid Shear Stress

HUVEC were seeded onto ibidi chamber slides (ibidi-treated μ -slides I^{0.4} or I^{0.6}, cat #80186 or ibidi-treated μ -slides VI^{0.4}, cat#80606, Germany), coated with 60 μ g/mL fibronectin (Sigma-Aldrich, F1141). At 80% confluency, HUVEC were exposed to laminar (steady 12 dynes/cm²) or oscillatory (0 +/- 12 dynes/cm², 1Hz) shear stress using the ibidi pump system (ibidi, cat #10902,

Germany) 1-3 days with or without drug treatments (as indicated in figure legends) perfused in the media.

Cell Fixation and Immunofluorescence Staining

HUVEC were washed two times with PBS and fixed for 10 min at room temperature with 4% paraformaldehyde in PBS. After three washes with PBS, the cells were permeabilized for 10 min at room temperature with 0.2% Triton X-100 in PBS and blocked with 5% BSA for 1 hour at room temperature. Cells were then incubated overnight at 4 degrees Celsius room temperature with the primary Ab diluted in blocking solution. The following primary antibodies were used: H3K9ac(Cell Signaling 9649; 1:400), H3K27me₃(Cell Signaling 9733; 1:1000), H3K9me₃(Cell Signaling 13969;1:100), Phospho-Histone H2A.X (Ser139) (Cell Signaling 9718; 1:400). Three more washes with PBS were then followed by incubation with the secondary Ab (Alexa Fluor 647-conjugated donkey anti-rabbit IgG; Thermo Fisher) and stained with rhodamine phalloidin (cat # PHDR1, Cytoskeleton) for 45 min followed by three additional PBS washes. Samples were stained with Hoechst 33342 (ThermoFisher) and mounted with ibidi mounting medium (ibidi, cat #50001, Germany).

Mouse Aorta Preparation and Immunohistochemistry

All animal studies were approved by the Virginia Commonwealth University Institutional Animal Care and Use Committee (protocol # AD10002187) and performed in accordance with the Guide for the Care and Use of Laboratory Animals (33). Mice were euthanized by CO₂ inhalation followed by cervical dislocation. The mouse heart was immediately perfused with saline solution containing heparin (Tocris Bioscience, 28-12100) and then were perfusion-fixed with either 10% formalin (Sigma-Aldrich, HT501320) or 100% methanol (Fisher

Scientific, BP28184). The aortas, arch and descending thoracic, were then harvested, cleaned *in situ* and then transferred to a 12-well dish containing saline. *En Face* preparation and immunohistochemistry of the tissue was performed using previously described methods (160).

The aortic arch and thoracic aorta were separated and dissected, then permeabilized with 0.1% Triton X-100 (Sigma-Aldrich, X100-500ML) for 10 minutes at room temperature or 100% ice cold methanol at -20°C for 10 minutes. All washing steps were done by washing three times with TBST-1X rocking at room temperature for 10 minutes each time. The samples were blocked with 10% normal donkey serum (abcam, 7475) in 1X Tris Buffered Saline with Tween 20 (TBST) diluted from TBST-10X (Cell Signaling, 9997) using ddH₂O for 30 minutes with rocking at room temperature. Primary antibodies were diluted in TBST-1X with 10% normal donkey serum overnight in 4°C. The following primary antibodies were used: H3K9ac(Cell Signaling 9649; 1:400), H3K27me₃(Cell Signaling 9733; 1:1000), H3K9me₃(Cell Signaling 13969;1:100), PECAM-1 (Santa Cruz Biotechnology sc-18916; 1:250). After washing, the tissues were fluorescently labeled with secondary antibodies diluted in TBST-1X with 10% normal donkey serum for 1 hour, rocking in room temperature. The following secondary antibodies were used: chicken anti-rat 647 (Invitrogen, A21472), donkey anti-rabbit 568 (Invitrogen, A10042), donkey anti-rabbit 647 (Thermo Scientific, A31573). Next, nuclear staining was done with Hoechst (Invitrogen, H3570) diluted in TBST-1X (1 µL: 10 mL) and incubated with rocking at room temperature for 30 minutes. After washing the tissues were mounted onto glass slides and sealed with ProLong Gold Antifade (Invitrogen, P36930).

Microscopy and Image Analysis

Fixed samples were imaged on Zeiss LSM 710 confocal microscope at 20x and 40x with water immersion. Histone modifications were quantified based on fluorescence intensities as previously described(159) using Fuji Image J. The orientation of actin fibers was measured using a custom Matlab program. The phalloidin channel of each image was selected, then sharpened and de-speckled using “imsharpen,” “edge,” and “bwareaopen” Matlab commands to isolate the actin fibers. The “regionprops” command was then used to measure the orientation of each region – the isolated actin fibers. The orientation of these fibers was then averaged, and the averaged orientations are reported. A randomly-distributed arrangement of fibers should have an average orientation of about 45°, which is what was observed in our static samples. An average orientation closer to zero is representative of fibers which are more oriented in the direction of fluid flow.

Fluorescence Lifetime Imaging Microscopy

Our FLIM setup utilized a Leica TCS SP5 inverted laser scanning confocal microscope and a 100x (1.4 NA) oil immersion objective. For excitation in the FLIM experiments, a Ti:sapphire mode-locked, pulsed infrared laser (Chameleon, Coherent) system was utilized as the multiphoton excitation source (1 W, average) tuned to 825 nm (Hoechst 33342) with pulse-widths of <140 fs delivered at 90 MHz. For emission, a FLIM-specific photomultiplier tube (PMT) was used and collected the spectra from 404-536 nm (Hoechst 33342). Fluorescence lifetime data was acquired and analyzed using previously published methods(92, 161) with a suite of software from Becker & Hickl SPC-830 for time-correlated single photon counting

(TCSPC) with 10 ps resolution along with 220 time channels and a 10.8 ns measurement window.

The decay rate of the fluorescence lifetime can be modeled as a summation of exponential decays (Equation 1), where τ_n and a_n are the lifetime and normalized amplitude of the n^{th} exponential decay, respectively. $I(t)$ is the number of photons detected per unit time, t , and I_0 is the offset for the background. The mean fluorescence lifetime is defined as shown in Equation 2.

$$I(t) = I_0 + \sum_n a_n e^{-t/\tau_n} \quad (1)$$

$$\tau_m = \frac{\sum_n a_n \tau_n}{\sum_n a_n} \quad (2)$$

The heat maps of the fluorescence lifetimes were created in Becker & Hickl SPCImage software along with the data analysis. For cell experiments, we segmented the nuclei in each field of view to isolate only nuclear pixel signal for data analysis using MATLAB. We analyzed the fluorescence lifetime fits using a χ^2 test, with Hoechst 33342 best modeled by a double exponential decay.

Statistical Analysis

Statistical significance was measured using an unpaired, two-tailed Student's t -test for data containing two groups. For data involving more than two groups, the analysis of variance (ANOVA) test was performed in order to obtain the statistical analysis for the data sets concerned. A further comparison of the groups was performed using the Tukey test to determine significant differences between groups. All statistical tests were conducted at a 5% significance level ($p < 0.05$). Prism GraphPad was used for statistical analyses. Every experiment was completed 3 times, and between 5 and 10 images from each group were analyzed. Data represents individual nuclei values with $n > 300$ per experiment.

Magnitudes of the mean fluorescence lifetimes were statistically compared using Student's t-test. Fits of the fluorescence lifetime exponential decay were verified using a χ^2 test. For nuclear chromatin condensation state experiments using FLIM, the mean fluorescence lifetimes and associated standard deviations in the figures reflect those for segmented nuclei, with the final magnitudes resulting from pixel-to-pixel averaging within segmented nuclei across multiple nuclei per field of view and multiple fields of view per treatment condition.

5.3. RESULTS

Endothelial cells adapted to shear stress have altered histone acetylation and methylation indicative of increased chromatin decondensation

We sought to understand how chromatin condensation changes in EC adapted to laminar shear stress (LSS). Human umbilical vein endothelial cells (HUVECs) were exposed to laminar and oscillatory shear stress at physiological levels of arterial shear stress (12dynes/cm²)(162) and assayed for histone markers H3K9ac, H3K27me₃, and H3K9me₃. H3K9ac is an epigenetic marker for histone acetylation, indicating chromatin decondensation(163). H3K27me₃ and H3K9me₃ are epigenetic markers for histone methylation, indicating chromatin condensation(164).

We observed that as EC remodeling occurs (indicated by actin alignment in the direction of flow), H3K9ac expression increases (**Figure 21A**) and H3K27me₃ expression decreases (**Figure 21B**), showing that EC adapted to laminar shear stress have increased chromatin decondensation. Under oscillatory flow, H3K9ac expression was higher than H3K27me₃ expression (**Figure 21A & 1B**). This result was surprising due to prior reports of increased methylation in regions of oscillatory flow(147, 165) *in vitro* as well as *in vivo*. We also examined

H3K9me₃ expression, as recently reported findings of its expression levels being correlated to nuclear stiffness in epithelial cells (159). In our *in vitro* endothelial shear model, we found that EC exposed to laminar shear stress had decreased H3K9me₃ expression compared to EC in static culture (**Figure 21C**). Under oscillatory flow, however, H3K9me₃ expression increased (**Figure 21C**).

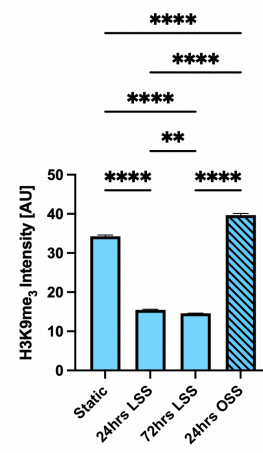
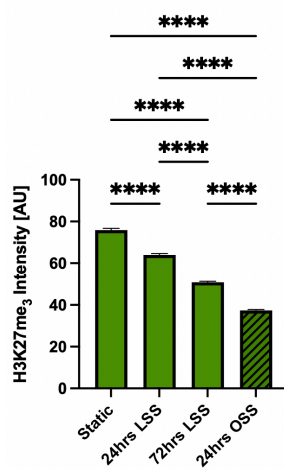
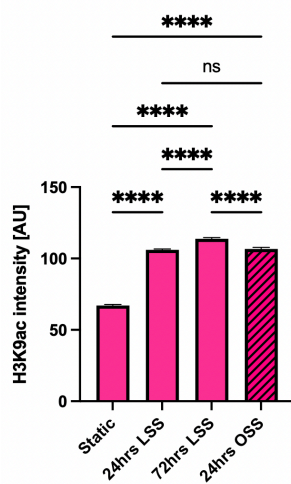
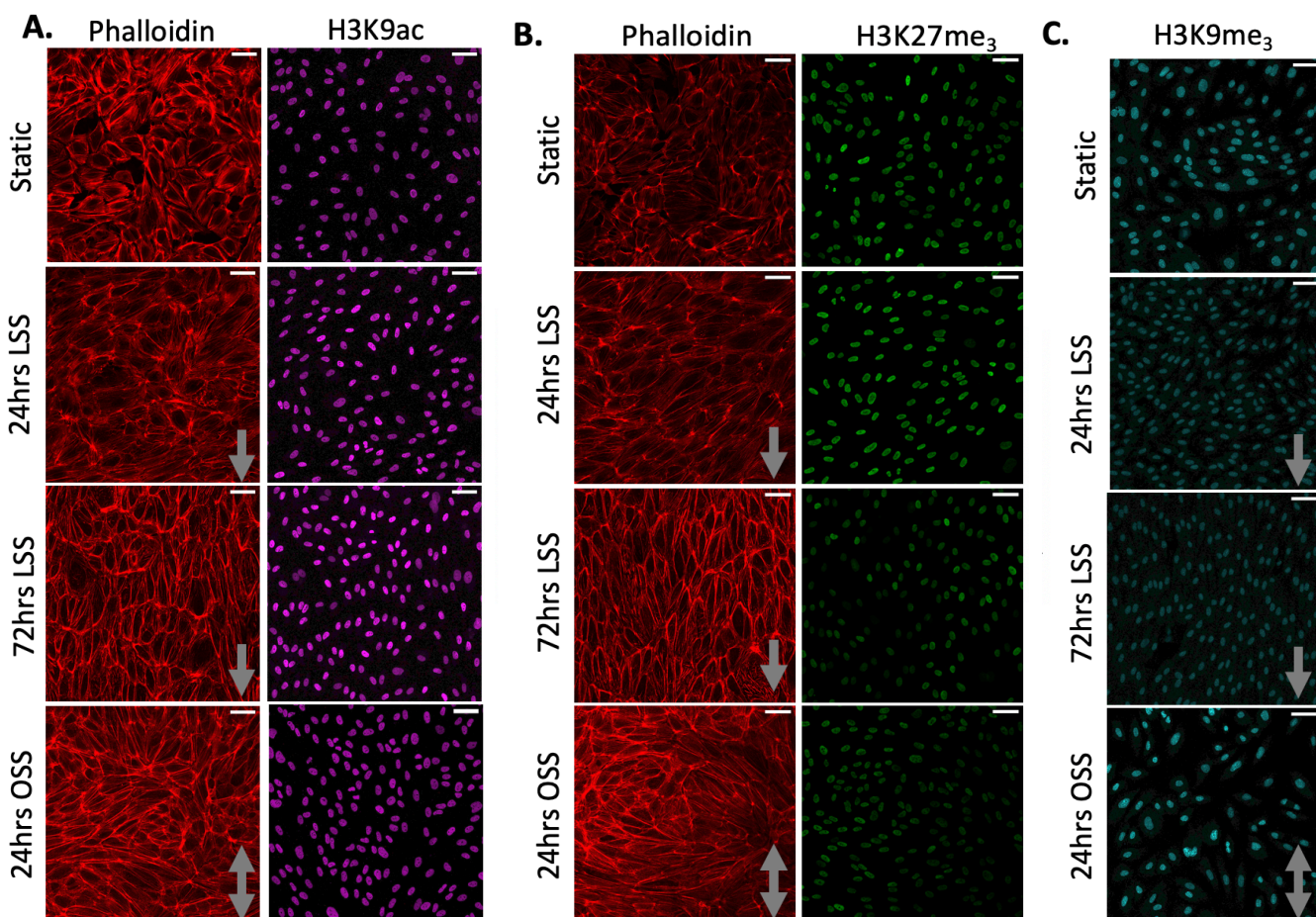


Figure 21: Epigenetic Modifications in Response to Fluid Shear Stress *in vitro*.

Representative phalloidin and histone epigenetic markers (H3K9ac, H3k27me₃, H3k9me₃) images and quantification of untreated EC exposed to 12 dynes/cm² laminar and oscillatory shear stress. Confocal images taken on 20x. Grey arrows indicated flow direction. Scale bar= 50µm.

(A) Laminar shear stress causes an increase in H3K9ac expression in aligned EC adapted to flow. Graph quantifies the fluorescent intensity of histone marker H3K9ac (three experiments with n>300 cells; ****p<0.0001, ns: non-significant; Ordinary one-way ANOVA with SEM/ Tukey's multiple comparisons.) **(B)** Laminar shear stress causes a decrease in H3K27me₃ expression in aligned EC adapted to flow. Graph quantifies the fluorescent intensity of histone marker H3K27me₃ (three experiments with n>300 cells; ****p<0.0001, ns: non-significant; Ordinary one-way ANOVA with SEM/ Tukey's multiple comparisons.) **(C)** Laminar shear stress causes a decrease in H3K9me₃ expression in aligned EC adapted to flow. Graph quantifies the fluorescent intensity of histone marker H3K9me₃ (three experiments with n>300 cells; ****p<0.0001, p<0.05; Ordinary one-way ANOVA with SEM/ Tukey's multiple comparisons.)

Endothelial cells adapt to shear stress *in vivo* through chromatin decondensation

Next, we sought to examine chromatin condensation *in vivo* by comparing histone acetylation and methylation changes of mouse EC in the descending aorta to the inner curvature of the aortic arch. EC in the descending aorta experience laminar shear stress whereas EC in the inner curvature of the aortic arch experience oscillatory shear stress(166). Our *in vivo* findings mirrored our *in vitro* findings in that EC adapted to LSS have an increase in H3K9ac expression. We observed that EC located in the descending aorta had more H3K9ac expression than the EC located in the aortic arch (**Figure 22A**). This suggests that chromatin decondensation is associated with EC adapted shear stress *in vivo* as well as *in vitro*. In contrast, H3K27me₃

expression was higher in the aortic arch than in the descending aorta (**Figure 22B**). This result was different than the EC histone modification expression in the *in vitro* model where H3K27me₃ was lower under OSS flow. When we looked at H3K9me₃ expression we saw no significant difference between the two regions of flow (**Figure 22C**).

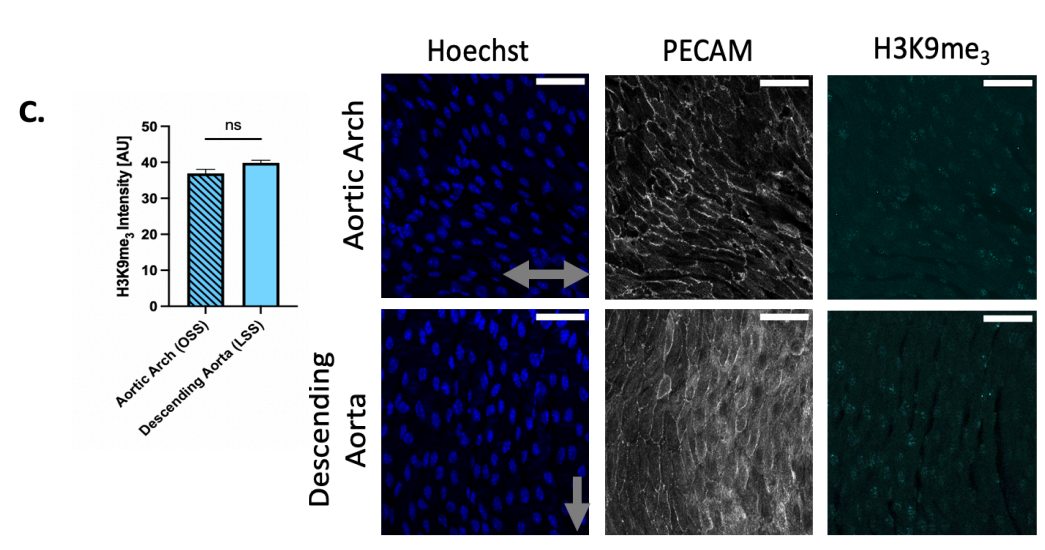
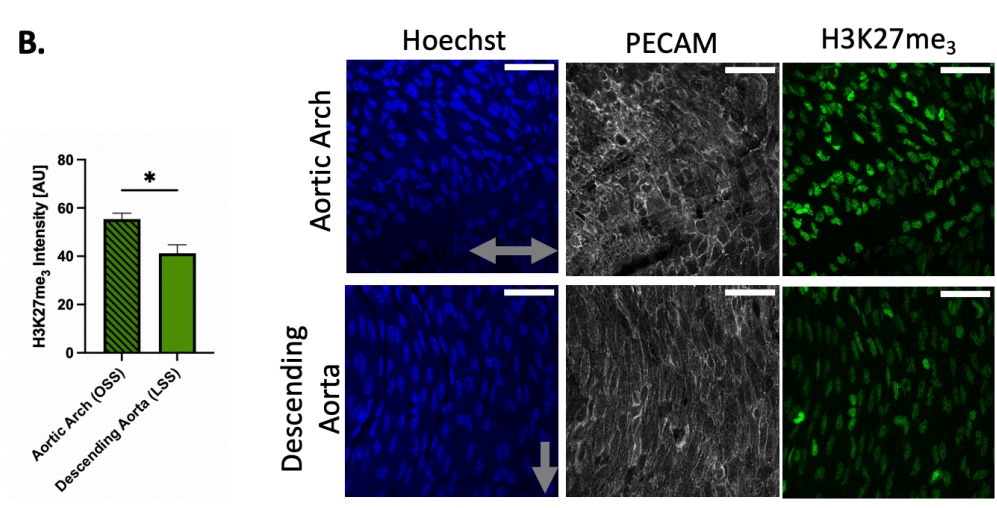
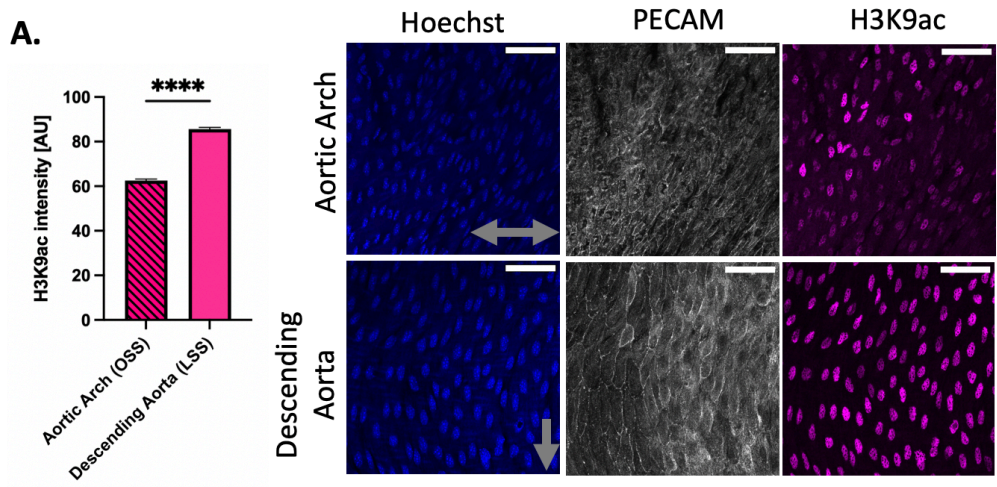


Figure 22: Epigenetic Modifications in Response to Fluid Shear Stress in vivo.

Representative Hoechst, PECAM, and histone epigenetic markers (H3K9ac, H3K27me₃) images and quantification of harvested mouse aortic tissue. Confocal images taken on 40x with water immersion. Grey arrows indicated flow direction. Scale bar= 50μm. **(A)** H3K9ac expression was higher in vascular region of laminar shear stress (descending aorta) than in regions of oscillatory flow (aortic arch). Graph quantifies the fluorescent intensity of histone marker H3K9ac (samples harvested from 3 mice; ****p<0.0001; Paired, Two-tailed T-test with SEM). **(B)** H3K27me₃ expression was higher in vascular regions of oscillatory flow (aortic arch) than in regions of laminar shear stress (descending aorta). Graph quantifies the fluorescent intensity of histone marker H3K27me₃ (samples harvested from 3 mice; *p<0.05; Paired, Two-tailed T-test with SEM). **(C)** No significant different was observed in H3K9me₃ expression between the descending aorta and the aortic arch. Graph quantifies the fluorescent intensity of histone marker H3K9me₃ (samples harvested from 3 mice; ns denotes non-significant; Paired, Two-tailed T-test with SEM).

Chromatin decondensation leads to faster EC actin alignment under laminar shear stress

EC were treated with histone deacetylase inhibitor, Trichostatin A (TSA), which has been previously shown to increase euchromatin(167, 168), whereas histone demethyltransferase inhibitor, Methylstat has been shown to increase heterochromatin(169). To confirm TSA and Methylstat were causing the desired histone modifications in our EC model, we did immunofluorescent staining and quantified fluorescent intensity of H3K9ac for histone 3 acetylation, and H3K27me₃ for histone 3 methylation. H3K9ac expression was increased in EC treated with 100nM TSA for 24 hours (**Figure 23B**), confirming that TSA causes chromatin decondensation. H3K27me₃ expression was increased in EC treated with 2.5μM Methylstat for 48 hours (**Figure 23B**), confirming Methylstat causes chromatin condensation.

To see how induced chromatin decondensation or condensation effects EC adaptation to flow, we examined how treatment with TSA or Methylstat affected EC alignment. ECs were exposed to static culture, as well as 12 dynes/cm² of laminar shear stress for 24 or 72 hours. Actin alignment was quantified by the mean actin orientation in degrees, where closer to 0 is more aligned in the direction of flow, and 45 degrees is random orientation (as seen in static conditions). Untreated EC showed complete actin alignment in the parallel direction of flow by 72 hours of shear stress, however, TSA-treated cells were completely aligned after only 24 hours of shear stress (**Figure 23A**). In contrast, cells treated with Methylstat did not align even after exposure to 72 hours of shear stress (**Figure 23A**). Taken together these results show that changes in chromatin organization affect EC adaptation to flow.

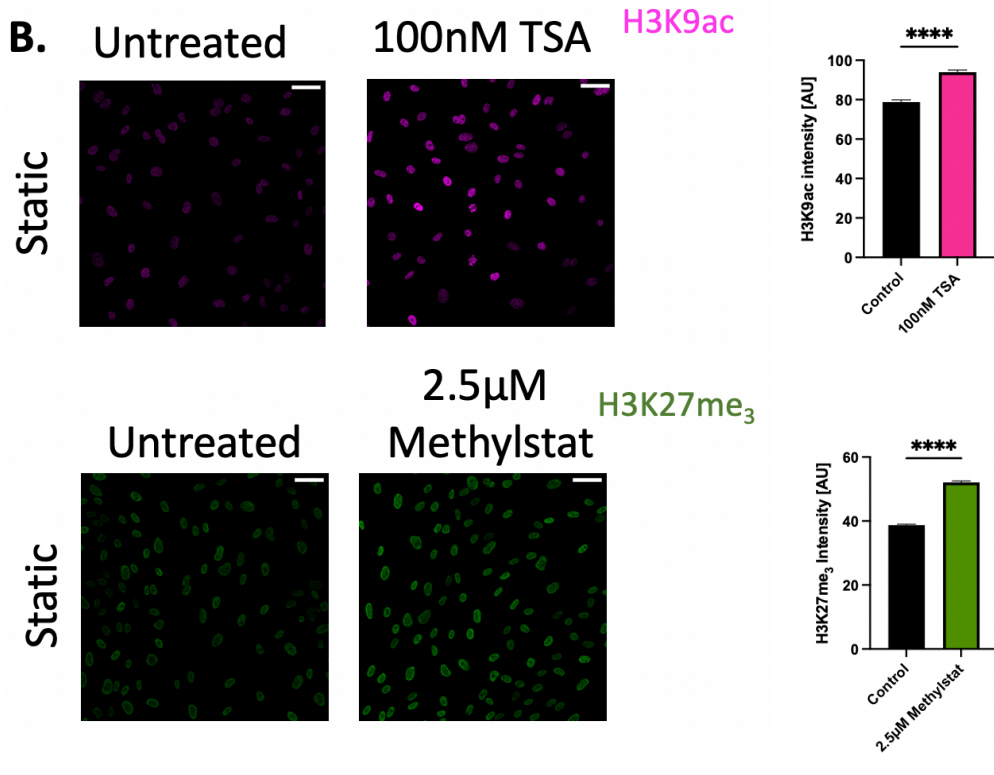
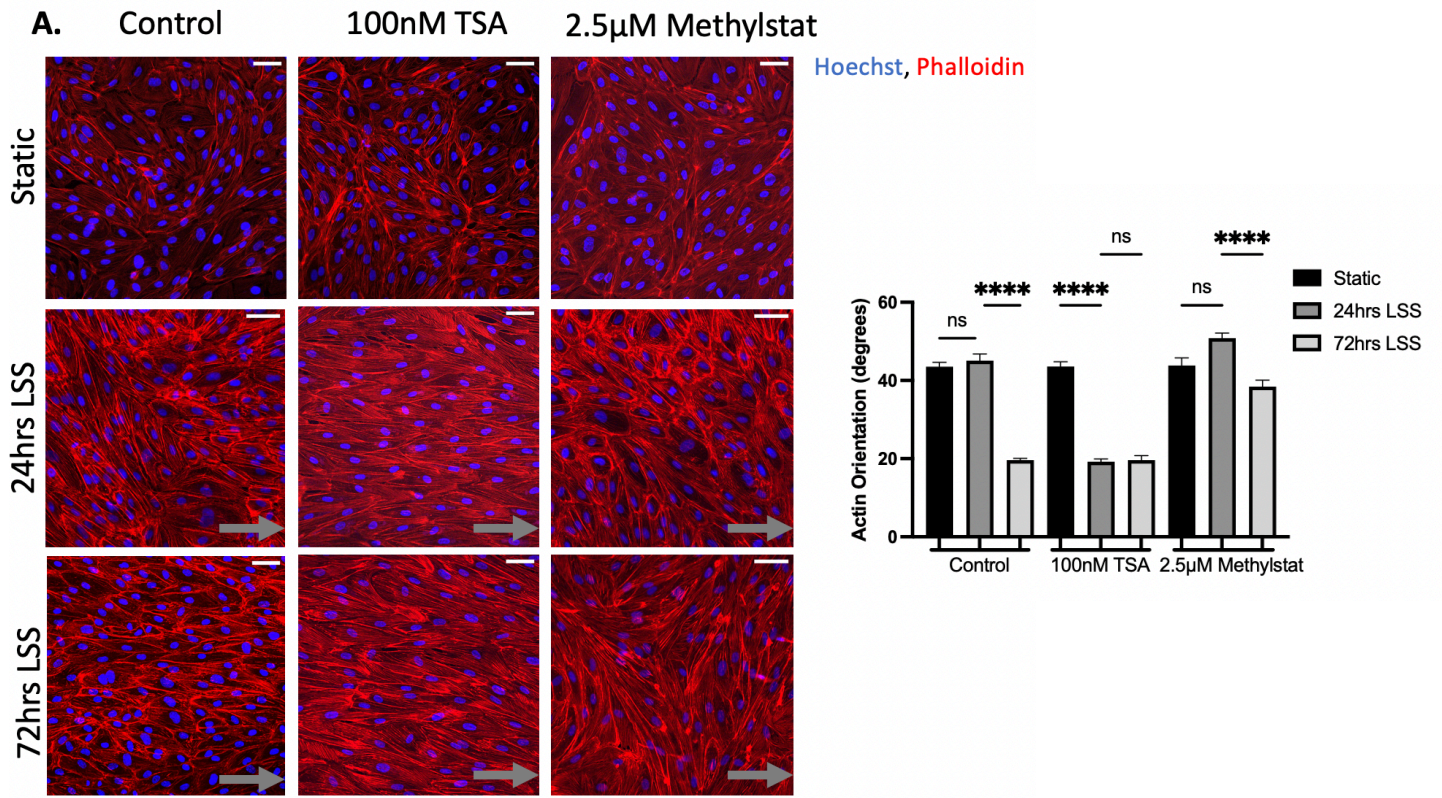


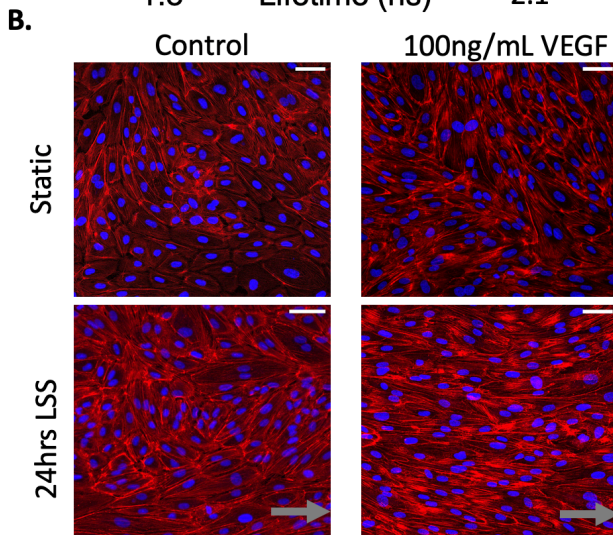
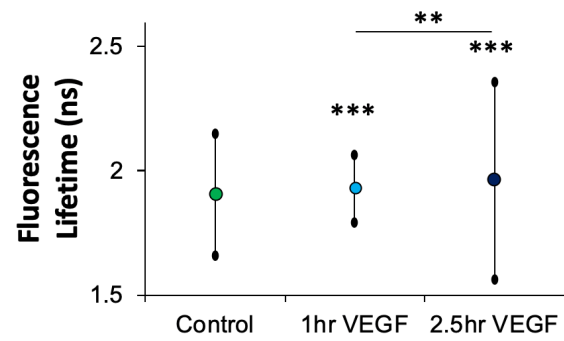
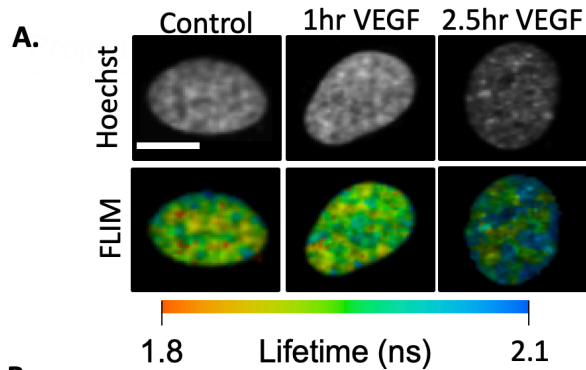
Figure 23: Chromatin decondensation increases the rate of EC alignment to shear stress.

(A) Representative phalloidin and Hoechst images and quantification of EC exposed to 12 dynes/cm² laminar shear stress. Confocal images taken on 20x. Grey arrows indicated flow direction. Scale bar= 50µm. Chromatin de-condensation through TSA treatment facilitate actin alignment 48 hours faster than untreated EC under shear stress. Chromatin condensation through Methylstat treatment blocks EC adaptation by inhibiting actin remodeling under shear stress. Actin orientation was quantified by fiber degrees. Static orientation is at 45 degrees (three experiments, data represents average per frame with 10 frames per experiment, ****p<0.0001, ns: non-significant; Ordinary one-way ANOVA with SEM/ Tukey's multiple comparisons). (B) Representative histone epigenetic markers (H3K9ac, H3K27me₃) images and quantification showing chromatin condensation changes due to EC treatment with TSA (increase in H3K9ac) and Methylstat (increase in H3K27me₃) compared to untreated controls. Confocal images taken on 20x. Scale bar= 50µm. Graph quantifies the fluorescent intensity of histone marker H3K9ac and H3K27me (3 experiments with each experiment having > 500 cells. **** p<0.0001. Two-tailed paired T-test with SEM).

VEGF decondenses chromatin and causes faster EC alignment

Next, to examine a more physiological treatment, we examined the effects of vascular endothelial growth factor (VEGF), a signal protein that stimulates angiogenesis, on both chromatin condensation and EC alignment. Prior work, using particle-tracking micro rheology, showed that VEGF treatment resulted in a more decondensed chromatin structure (92). Using fluorescence lifetime measurements to characterize chromatin condensation state(170), we examined the effects of VEGF treatment on EC chromatin mobility. We observed an increasing number of high mean fluorescence lifetime regions within the nucleus with increasing duration

(1-2.5 hours) of VEGF exposure consistent with a growing number of regions of decondensed chromatin (**Figure 24A**). At later times, we qualitatively observe a combination of low and very high mean fluorescence lifetime regions consistent with regions of both condensed chromatin and decondensed chromatin, respectively. Next, we examined if VEGF treatment would also accelerate EC alignment to LSS. We observed VEGF treated EC aligned faster to laminar shear stress (**Figure 24B**), mirroring the results of TSA treatment (**Figure 23A**). These results further support the hypothesis that increasing chromatin decondensation accelerates EC alignment in response to shear stress.



Hoechst, Phalloidin

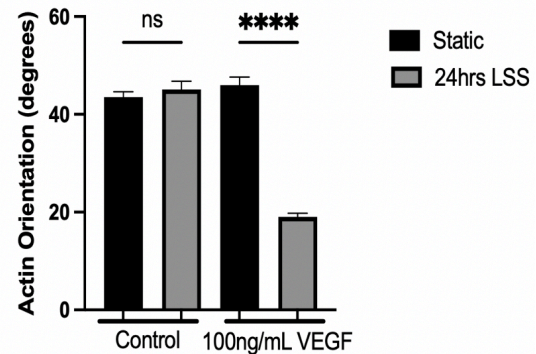
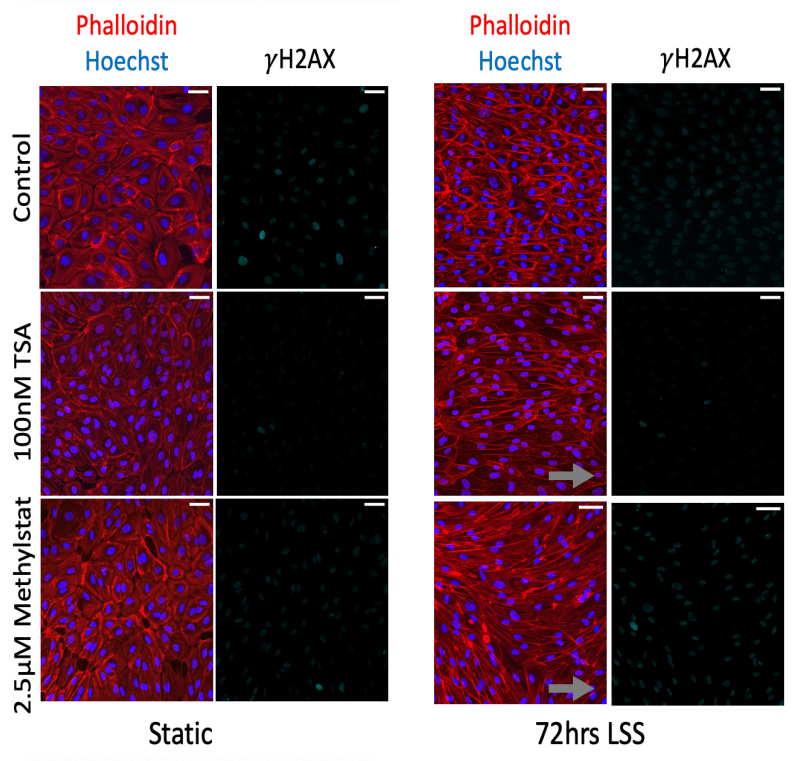
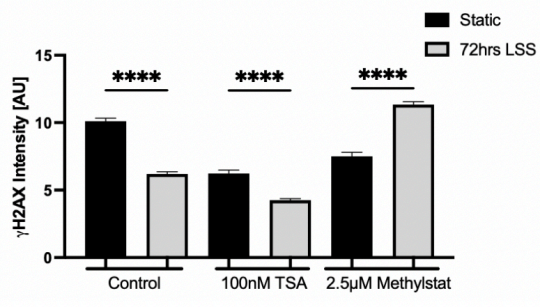


Figure 24: VEGF treatment increases chromatin decondensation and increases the rate of EC alignment to shear stress. (A) Fluorescence lifetime measurements of chromatin condensation state during stimulated gene activation in VEGF-stimulated endothelial cell nuclei. Fluorescence intensity confocal images (top) and mean fluorescence lifetime heat maps (bottom) of chromatin in EC nuclei labeled with Hoechst 33342 and treated with 50ng/mL of VEGF for 0, 1 or 2.5 hours. Mean fluorescence lifetime heat maps indicate spatial arrangement of local fluorophore environments for stained chromatin which is consistent with varying chromatin condensation state. Altered fluorescence intensity with treatments show differential chromatin condensation state, with more intense fluorescence arising from highly concentrated condensed chromatin. Graph shows treatment with VEGF at both time points resulted in a strong and statistically significant increase the mean fluorescence lifetime relative to untreated controls ($***p < 0.001$), with a step-wise increase at each time point ($**p < 0.025$). Analysis was done using 60-80 segmented nuclei for each treatment condition. Error bars indicate standard deviation of pixel-to-pixel mean fluorescence lifetime differences of segmented nuclei under each treatment condition. Scale bar is 10 μm . **(B)** Chromatin de-condensation through VEGF treatment facilitate actin alignment 48 hours faster than untreated EC under shear stress. Representative phalloidin and Hoechst images and quantification of untreated EC exposed to 12 dynes/cm² laminar shear stress. Confocal images taken on 20x. Grey arrows indicated flow direction. Scale bar= 50 μm . Actin orientation was quantified by fiber degrees. Static orientation is at 45 degrees (three experiments, data represents average per frame with 10 frames per experiment, $****p < 0.0001$, ns: non-significant; Ordinary one-way ANOVA with SEM/ Tukey's multiple comparisons).

Changes in chromatin condensation affect shear stress-induced DNA damage

We next examined how changes in chromatin condensation would affect shear stress-induced DNA damage. Untreated control cells, when fully aligned to fluid shear stress (72 hours) had less γ H2AX foci detected by immunofluorescence as compared to static culture (**Figure 25A**), consistent with a prior report showing that fluid shear stress increases expression of p53, potentially enhancing DNA repair(171). When cells were treated with TSA to decondense chromatin, a further reduction in γ H2AX foci was observed in both static and laminar shear stress conditions. Interestingly, Methylstat treatment increased DNA damage most significantly in cells exposed to laminar shear stress. In similar experiments cells were exposed to OSS after treatment with TSA or Methylstat. Oscillatory shear stress induced the most DNA damage in TSA treated EC (**Figure 25B**). Thus, changes in chromatin condensation not only affect EC alignment but also affect DNA damage.

A.



B.

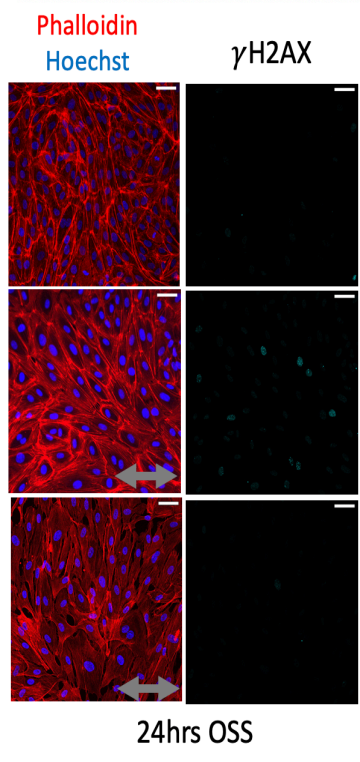
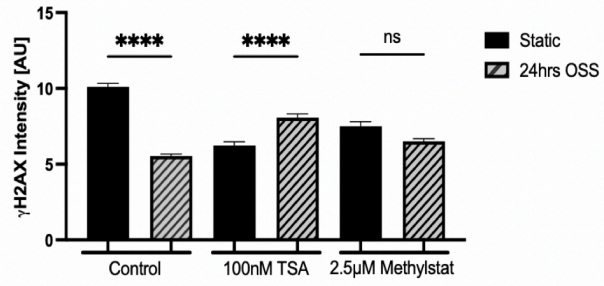


Figure 25: Changes in chromatin condensation affect shear stress induced DNA damage.

Representative phalloidin, Hoechst, and DNA double-stranded DNA damage marker γ H2AX.

images and quantification of untreated EC exposed to 12 dynes/cm² laminar and oscillatory shear stress. Confocal images taken on 20x. Grey arrows indicated flow direction. Scale bar= 50 μ m.

(A) Laminar shear stress in EC with condensed chromatin (Methylstat-treated cells) causes an increase in DNA damage. Graph quantifies the fluorescent intensity of γ H2AX (three

experiments with n>300 cells; ****p<0.0001; Ordinary one-way ANOVA with SEM/ Tukey's

multiple comparisons.) **(B)** Oscillatory shear stress in EC with decondensed chromatin (TSA-treated cells) causes an increase in DNA damage. Graph quantifies the fluorescent intensity of

γ H2AX (three experiments with n>300 cells; ****p<0.0001, ns: non-significant; Ordinary one-way ANOVA with SEM/ Tukey's multiple comparisons.)

5.4 DISCUSSION

In this paper we show both *in vitro* (**Figure 21**) and *in vivo* (**Figure 22**) that fluid shear stress affects histone 3 methylation and acetylation, by examining immunostaining of H3K9ac, H3K27me₃, and H3K9me₃. Overall, our data suggest that EC exposed to laminar shear stress (atheroprotective) have histones which are more acetylated and less methylated, suggesting a more decondensed chromatin structure in EC following adaptation to laminar shear stress. While this data is mostly correlative, we also demonstrate that changes in chromatin condensation with small molecules (**Figure 23**) and VEGF (**Figure 24**) significantly affect EC adaptation to shear stress, using EC alignment as a marker for adaptation. Thus, changes in chromatin condensation greatly impact the propensity of cells to align to shear stress. Lastly, we show that changes in chromatin condensation affect markers of DNA damage (**Figure 25**).

Prior work has also studied the role of histone acetylation and methylation changes during adaptation to shear stress. Early studies showed that short-term exposure (<120 minutes) laminar shear stress induces chromatin remodeling through H3/H4 acetylation(144, 152). Our findings of increased H3K9ac are in agreement with these prior studies, and demonstrate that increased acetylation persists in cells exposed to laminar shear stress as compared to static culture (**Figures 21A and 22A**). More recent work has shown that that oscillatory or atheroprone fluid shear stress increases genome-wide DNA methylation patterns in a DNA methyltransferase-dependent (DNMT-dependent) manner(145, 172). In this study we observed increases in H3K9me₃ (*in vitro*, **Figure 21C**) and H3K27me₃ (*in vivo*, **Figure 22B**) for EC exposed to oscillatory shear stress as compared to laminar shear stress, in agreement with these prior studies showing increased methylation with oscillatory shear stress. However, we observed divergence in the H3 methylation markers upregulated by shear stress in *in vitro* versus *in vivo* experiments. The *in vitro* versus *in vivo* differences in H3 methylation markers could be due to differences in the time of exposure to oscillatory shear stress (24 hours *in vitro* vs months *in vivo*), with the *in vitro* results representing an initial response and the *in vivo* results representing a more terminal response. We also acknowledge that there may be additional factors beyond shear stress that may be regulating histone methylation in the different regions of the aorta.

Although the nuclear lamina is considered to be a major contributor to nuclear stiffness, (35, 36), changes in chromatin condensation, as a result of altered histone acetylation and methylation, have been shown to affect nuclear stiffness independent of the nuclear lamins (6, 115). The changes observed in histone acetylation and histone methylation (**Figures 21 and 22**) are suggestive of nuclei being softer in EC exposed to laminar shear stress when compared to EC exposed to oscillatory shear stress. We also note that *in vitro* oscillatory shear stress increased

expression of H3K9me₃, which has also been previously shown to be a histone marker that correlates to nuclear stiffness(159). Thus, it is tempting to speculate that the observed changes in chromatin methylation and acetylation markers are indicative of changes in nuclear stiffness.

We note prior work by Deguchi and colleagues which showed increased nuclear stiffness in EC aligned to laminar shear stress as compared to EC in static culture (130). It is not yet known if there are differences in nuclear stiffness for EC exposed to laminar shear stress versus oscillatory shear stress. Additionally, it is not yet understood how nuclear stiffness may change during earlier timepoints when EC are actively adapting to shear stress. Nuclear circularity, elongation, and area have already been shown to rapidly change upon exposure to shear stress (173)—thus it may be possible that nuclear stiffness changes rapidly as well at the onset of flow. Further supporting the requirement for an “adaptable” EC nucleus, our group has shown that EC with stiffer nuclear lamins cannot adapt to shear stress (174).

We observed that increasing histone acetylation allowed EC align more rapidly to shear stress, whereas increasing histone methylation inhibited EC alignment (**Figure 23**).

Additionally, similar enhancements of EC alignment can be obtained with a physiological stimulus (VEGF), which also increases chromatin mobility (**Figure 24**). These data clearly demonstrate that EC with decondensed chromatin adapt to flow faster. One mechanism to explain this enhanced adaptability is that reduced nuclear stiffness, as a result of chromatin condensation, allows for a more rapid change in nuclear shape during the EC alignment process. Prior work using atomic force microscopy has shown that chromatin compaction via TSA treatment resulted in decreased nuclear stiffness by ~35% (175) and that Methylstat treatment increased nuclear stiffness by ~40% (115), indicating that these treatments are likely inducing substantial changes to nuclear stiffness to EC in our experiments. We also note that it is well

established that significant gene expression changes occur during the process of EC adaptation to shear stress (143). Thus, an alternative or parallel mechanism to explain the enhanced alignment speed by chromatin decondensation is that decondensed chromatin enhances gene expression changes needed for adaptation to shear stress.

An interesting observation of our findings is that changes in chromatin can also influence shear stress-induced DNA damage. Mechanical forces have been shown to induce DNA damage in a wide variety of contexts(176). The Wickström group recently showed that changes in nuclear mechanical properties can counteract the effects of force-induced DNA damage. Specifically, epithelial cells respond to mechanical stretch by decondensing chromatin by reducing chromatin methylation. These changes in chromatin condensation are critical for preventing stretch-induced DNA damage (159). Our work shows similar findings in the context of laminar shear stress. EC with decondensed chromatin have less DNA damage when exposed to laminar shear stress (**Figure 25A**). Interestingly, our findings were opposite with oscillatory shear stress, where EC with a more condensed chromatin experienced less DNA damage. (**Figure 25B**). In some cases increased chromatin rigidity has been shown to provide genome protection(177). It therefore appears that the relationship between EC chromatin condensation and DNA damage varies depending on the type of mechanical force (LSS vs OSS).

In conclusion, this study demonstrates that chromatin condensation is not only regulated by fluid shear stress, but is a critical parameter that regulates EC mechanoadaptation to fluid shear stress. There are likely many physiologically and pathologically relevant processes, such as inflammation, that regulate EC chromatin condensation, and in turn have the potential to alter EC adaptation to shear stress, as well as force-induced DNA damage. It will be interesting to

determine the role of chromatin condensation in other potential mechanosensitive EC processes, such as angiogenesis.

CHAPTER 6: NUCLEAR LAMINA STRAIN STATES REVEALED BY INTERMOLECULAR FORCE BIOSENSOR

Danielsson, B.E., Abraham, B.G, Mäntylä, E*, Cabe, J.I., Mayer, C.R., Rekonen, A., Ek, F., Conway, D.E., Ihalainen, T.O. Submitted to BioRxiv on March 7, 2022. <https://doi.org/10.1101/2022.03.07.483300>. Submitting to Nature Methods on March 14, 2022.*

6.1. RATIONALE

Mechanical forces are important co-regulators of many physiological processes(178). In addition to mechanotransduction at the surface of the cell, the cytoskeleton also allows transmission of forces throughout the cell, including onto and within the nucleus(179). Thus, the nucleus has emerged as a putative mechanosensitive structure. The Linker of Nucleoskeleton and Cytoskeleton (LINC) complex, consisting of nesprin, SUN, and lamin proteins, is the principal structure that connects the nucleus to the cytoskeleton(18). These connections enable a mechanotransmission pathway, where mechanical stress can be transduced outside-in and inside-out between the cell surface and the nucleus via the cytoskeleton(8).

The lamina is approximately 15 nm thick protein meshwork, formed mainly from flexible ~400 nm long A-type and B-type lamin filaments(55, 180). Large parts of the chromatin are either stably or dynamically tethered to the nuclear lamina and this tethering has been shown to regulate gene expression(180). Especially A-type lamin proteins are also located throughout the nucleoplasm. Although less characterized, these intranuclear or nucleoplasmic lamins bind to chromatin and have been shown to regulate chromatin accessibility and spatial chromatin organization(181).

Similar to other intermediate filament proteins, *in vitro* experiments of purified nuclear lamins have shown that these proteins are able to withstand large mechanical forces, have been

shown to exhibit deformation under mechanical loading, and exhibit strain-stiffening behavior(182). To study the mechanical loading of lamins *in vivo*, we sought to develop a biosensor for lamin A. Prior force biosensor design strategies consisted of chimeric proteins in which FRET-force module (a FRET pair separated by a strain-sensitive peptide) was inserted in the middle of the protein(178). These intramolecular force sensors have been successfully used for proteins at focal adhesions, cell-cell adhesions, and the nuclear LINC complexes. However, concerns remain regarding how internal insertion of a large FRET-force module (~50 kDa) could alter the biological functions of the protein. This may be especially important in the context of filamentous proteins, such as the nuclear lamina, where altered lamin proteins could disrupt or impair the oligomerization and/or polymerization of filamentous structures. Here we report a new intermolecular strain sensor design for measuring mechanical forces on lamin A.

6.2. METHODS

Sensor Design

A sensor to measure mechanical forces on the nuclear lamins was designed using an existing lamin A nanobody. The nanobody was previously developed by Rothbauer et al(52) and is currently commercially distributed as a “chromobody”, consisting of the nanobody tagged with GFP, by Chromotek (Planegg-Martinsried, Germany). The sensor is designed such that an existing FRET-force biosensor, known as TSmod(183) is flanked on either side by the lamin A nanobody V_{HH} sequence (Fig. 1a). To ensure nuclear localization of the protein a c-myc NLS was inserted between each nanobody and TSmod. Additionally, the c-terminal lamin A nanobody was designed by using the reverse sequence of the V_{HH} for orientation of the nanobody outwards from TSmod. The entire sequence of the nanobody-TSmod-reverse nanobody was synthetically cloned by GeneArt (Thermo Fisher Scientific) into pcDNA 3.3. The plasmid is available through Addgene

(plasmid# 178641). A control force-insensitive lamin sensor, consisting of only one nanobody attached to TSmod was also developed and is available through Addgene (plasmid# 178642).

A second sensor was developed designed to measure forces between the nuclear lamina and histones. This sensor consists of a nanobody which binds to the Histone H2A-H2B heterodimer that was previously developed by(184) and is also commercially distributed as a “chromobody” by Chromotek. The sensor was designed similarly to the lamin sensor, with the N-terminal lamin A sensor being replaced with the histone nanobody (histone nanobody-TSmod-reverse lamin A nanobody). This sensor was also synthetically cloned by GeneArt and is available through Addgene (plasmid# 178643). A control force-insensitive histone sensor, consisting of only the histone nanobody attached to TSmod was also developed and is available through Addgene (plasmid# 178644).

Cells

Madin-Darby canine kidney cells (MDCK II) were used in all studies and maintained in high glucose DMEM (Thermo Fisher Scientific) to which was added 10% fetal bovine serum (Thermo Fisher Scientific) and 1 % penicillin/streptomycin (Thermo Fisher Scientific) under standard cell culture conditions. To generate stable cell lines MDCKs were transfected with the TSmod and selected using G418. For the DN-KASH experiments, DN-KASH inducible Lamin-SS cells and DN KASH inducible Lamin-SS-t cells were made into stable cell lines. To generate a system for doxycycline-inducible DN-KASH Lamin-SS cells and doxycycline-inducible DN-KASH Lamin-SS-T cells, the previously established doxycycline-inducible DN-KASH MDCK cells(185) were electroporated with Lamin-SS pcDNA and Lamin-SS-T pcDNA separately. Cells

expressing both DN-KASH and Lamin-SS/SS-T were extracted with cloning rings and were clonally expanded.

Establishment of LMNA knockout with CRISPR/Cas9

To generate a pre-LMNA knockout (KO) MDCK II cell line with CRISPR/Cas9, single guide RNAs (sgRNAs) were custom made from Invitrogen backbone from their LentiArray™ Human CRISPR Library and designed against LMNA1 gene N-terminus in CanFam 3.1 reference genome (https://www.ncbi.nlm.nih.gov/nucore/NM_001287151.1, GeneID: 480124) with an online guide design tool. LMNA target sequence: atggagac cccgtcccag cggcgcgcca cccgtagcgg ggcgaggcc agtccaccc cgctgtcgcc caccgcac acccggctgc aggagaagga ggacctgcag gagtcaatg accgcctggc ggtctacatc gaccgtgtgc gctctctgga gacggagaac gcggggctgc gccttcgcat caccgagtcg. The sgRNA_LMNA_N1 nucleotide sequence was CACGGTCGATGTAGACCGCC (on-target locus chr7:-41719582). For expression, the sgRNA_LMNA_N1 (300 ng) and pCDNA3.1-dCas9-2xNLS-EGFP (gift from Eugene Yeo, #74710, Addgene; <http://n2t.net/addgene:74710>) were transfected by using the Neon™ electroporation system (1650 V, 20 ms, 1 pulse; Thermo Fisher Scientific) followed by selection of GFP-positive cells with G418 (0.25 mg/mL, Merck) and FACS sorting (BD FACSAria Fusion, BD Biosciences)(186). The success of the KO was determined via Western blot and further confirmed by immunostainings.

Drug Treatments

For actin depolymerization studies, Cytochalasin D (cat # 11330, Caymen Chemical) was used at 10 µg/mL for 1 h. To inhibit Rho A kinase, 50 µM Y-27632 (cat #72302, Stem Cell Technologies) was used for 1 hour prior to FRET imaging to reduce myosin activity. For EMT induction, recombinant human TGF-β1 (R&D systems) was used to induce EMT at a concentration

of 2 ng/mL for 24 h. Modifications in DNA ultrastructure were done to condense or decondense chromatin with the use of 600nM trichostatin A (TSA) for 4 h (Cayman Chemical Company), to increase euchromatin, and 2.5 μ M methylstat (Sigma Aldrich) for 48 h, to increase heterochromatin. For the cell cycle synchronization assay, Aphidicolin (cat #57-361, Thermo Fisher Scientific) was used to block the cells in early S-phase, at 3 μ g/mL for 24 h.

Immunofluorescence Staining of Lamins and Histones

For fixed-cell experiments, cells were washed with PBS and fixed for 10 min at room temperature with 4 % paraformaldehyde in PBS. After three washes with PBS, the cells were permeabilized for 10 min at room temperature with 0.2 % Triton X-100 in PBS and blocked with 5 % BSA for 1 h at room temperature. Cells were then incubated overnight at 4 °C or in room temperature with the primary Ab diluted in blocking solution. The following primary antibodies were used: anti-lamin A antibody (cat # sc-7292, Santa Cruz Biotechnology), anti-mouse LA/C-C (131C3, ab8984, Abcam) anti-rabbit LA/C-rod (EP4520-16, ab133256, Abcam), or anti-Rabbit Histone H2A (cat #12349, Cell Signaling Technology). Three more washes with PBS were then followed by incubation with the secondary Ab (Alexa Fluor 647-conjugated donkey anti-mouse IgG; Thermo Fisher) for 45 min followed by three additional PBS washes. Samples were stained with Hoechst 33342 (ThermoFisher) and mounted with ProLong Gold antifade mountant (P36930, Thermo Fisher Scientific).

Fluorescence Microscopy of Histones and Nuclear Lamina Organization

Confluent non-treated or either trichostatin A (TSA, 4h, 600 nM) or methylstat (48h, 2.5 μ M) -treated MDCKII wt, MDCK G2-TS or MDCK G2-truncated mutant cells were analyzed to

ensure the drug treatments used in FRET-experiments did not affect the nuclear lamina organization. To detect changes in nuclear lamina organization, ratiometric fluorescence immunoassay was performed on MDCKII wt, MDCK G2-TS or MDCK G2-truncated mutant cells immunostained against either lamin A/C N-terminus (LA/C-N, E1, sc-376248, Santa Cruz Biotechnology, Texas, USA) and histone H3 lysine 27 acetylation (H3K27ac, ab4729, Abcam), or lamin A/C C-terminal (anti-mouse LAC/C-C, 131C3, ab8984, Abcam, Cambridge, UK) and lamin A/C rod domain (anti-rabbit LA/C-rod, EP4520-16, ab133256, Abcam) as described above. Imaging was done on a Nikon A1R+ laser scanning confocal mounted in Nikon Eclipse Ti2-E inverted microscope (Nikon Instruments, Tokyo, Japan). Nikon 60X/1.40 Apo DIC N2 oil immersion objective was used in the experiments. Solid state lasers with excitation wavelengths 488 nm, 561 nm and 640 nm were used in excitation. The emissions were collected with 525/50, 540/30 and 595/50 bandpass filters, respectively. The laser intensities were adjusted to avoid photobleaching and the detector sensitivity was adjusted to optimize the image brightness and to avoid saturation. Laser powers and detector voltages were determined individually per treated antibody pair, and after the initial setting kept constant for each sample to allow ratiometric imaging and quantitative comparison of the fluorescence intensities within the drug-treated and non-treated control samples. The images were 1024x1024 pixels and the pixel size was 103.6 μm in x/y. The images were acquired without averaging and by first focusing on the bottom surface of the sample, where the position of the sample stage was set as $z_0=0$. The fluorescence signal intensities from all emission channels were then collected from bottom to top as optical z-series with 200 nm step size. The pinhole was set to 0.9 (physical pinhole size 34.76 μm). The analysis was done in ImageJ software by making maximum intensity projections from the acquired z-stacks, and by using the LA/C-rod channel to segment the nuclei which was then used as a mask

to measure the maximum signal intensities for all channels. The mean intensities of the nuclei, the background, and the total images were determined. To detect changes in the lamin organization the nuclear lamin intensity ratio (LA/C-C:LA/C-rod) was calculated from the nuclear intensities of which the detector noise was subtracted and which were normalized against their background. Number of replicates, n=3 for all treatments. Non-paired Student's t-test was used to test the statistical significance between treated and non-treated control samples. ns= non-significant, *p<0.05, **p<0.01, ***p<0.001.

Super-resolution Airy-scan Imaging

Zeiss LSM 980 laser scanning confocal microscope with airyscan was used for fixed-cell experiments. The system was mounted on Axio Observer.Z1 microscope body and Plan-Apochromat 63X/1.4 oil immersion objective was used in the imaging. The sensor and the immunolabelled lamin A/C were excited with 488 nm and 639 nm lasers using MDS488/561/639 triple dichroic and the emission was collected with band-pass 495-560 nm and long-pass 650 nm filters. The image size was set to 1032 x 1032 pixels, with pixel size of 43 nm and optical section collected with 170 nm intervals. Scanning was bidirectional with 2 μ s pixel dwell time and averaging of 4 was used. Data was analysed with ImageJ FIJI -distribution.

Fluorescence Recovery After Photobleaching (FRAP)-Experiments

Zeiss LMS780 laser scanning confocal microscope in inverted Cell observer microscope body was used in the experiments. MDCK cells stably expressing Lamin-SS or Lamin-SS-T were seeded on collagen-I-coated (50 μ g/mL in PBS, 45 min in RT) high performance coverslips (Zeiss, #474030-9020-000) 1 d before the experiments. Prior imaging, the coverslips were mounted on

imaging chamber (Aireka Cells, #SC15022, Aireka Scientific, HK, China) and placed in the microscope incubator (37 °C, 5% CO₂). Imaging was conducted by using 63X/1.2 WI C-Apochromat objective. Lamin-SS or Lamin-SS-T was excited with 514 nm laser line, pixel size was adjusted to 0.13 μm (zoom setting 4) and 256 x 256-pixel images were captured without averaging (195 ms scanning time per frame). In the FRAP experiment, images were collected with 250 ms intervals (249 images altogether), and a bleaching was conducted after 9 scans. In the bleaching phase, a pre-drawn rectangular area of 75 x 10 pixels in the nuclear lamina was scanned 25 times (iterations) with 100 % light intensity from 514 nm laser. The recovery was then followed for 240 frames.

FRAP Data Analysis and Simulations

FRAP recovery curves were measured by using ImageJ FIJI-distribution(187). The drift of the nucleus during the imaging was corrected by using StackReg-plugin(188). Next the fluorescence was measured from the lamina and from the whole nucleus. The data was then normalized in Microsoft Excel for Mac (version 16.55) according to Phair & Misteli(189):

$$I(t) = (lamina(t)/lamina(t = 0))/(nucleus(t)/nucleus(t = 0)) \quad (1)$$

Where lamina(t) is fluorescence in the lamina at time point t, lamina(t=0) is fluorescence in the lamina before the bleach phase, nucleus(t) is the fluorescence of the whole nucleus at time point t and nucleus(t=0) is the fluorescence of the nucleus before the the bleach phase. Finally, the normalized recoveries were averaged.

Virtual Cell software(190, 191)was used to simulate the FRAP experiment and fluorescence recovery. The model contains a free Lamin-SS sensor which can bind to an immobile binding site in the lamina (single bound sensor), this binding can then lead into release of the

sensor or tighter binding, simulating the situation where the sensor is engaged from both nanobodies (dual bound sensor). The release of the dual bound sensor was assumed to happen via single bound-state. The Lamin-SS-T sensor behavior was assumed to behave otherwise similarly, only the dual binding opportunity was missing. The reaction network schematic is visualized in Supplementary Figure 2. The Virtual Cell Models, “Lamin-SS_dual_binding” and “Lamin-SS-T_single_binding” by user “teihalai”, can be freely accessed within the VCell software (available at <https://vcell.org>).

SensorFRET Imaging and Analysis

Live cells were seeded on glass-bottom slides coated with 20 μ g/mL fibronectin. DMEM was replaced with live cell imaging solution (cat #: A14291DJ, Thermo Fisher) supplemented with 10% FBS. Images were acquired using an inverted Zeiss LSM 710 (Oberkochen, Germany) confocal microscope using both 405 nm or 458 nm excitation wavelengths from an argon laser source. A 40x water immersion objective lens (NA = 1.1) was used for all imaging. Live cells were imaged in spectral mode using a 32-channel spectral META detector to record spectra of each pixel spanning wavelengths from 416 to 718 nm (*with 9.7 nm spectral steps*). Images were captured in 16-bit mode, scanned bi-directionally, and averaged 4 times. For sensorFRET based efficiency imaging, spectral images at both 405 and 458 nm excitation wavelengths were acquired. The normalized emission shape of the mTFP and mVenus fluorophores as well as the calibration parameter c (= 0.101) required for the sensorFRET analysis were experimentally determined from control cells expressing single fluorophores(192). Intensity images were further processed and analyzed using a custom Python code, which involves background subtraction and removal of saturated pixels. For each data set, the data was acquired for at least 5 images per condition per experiment. Images were masked manually on Fiji Image J.

Paired FRET Measurements and Analysis

Ratiometric FRET imaging was used for FRET measurements involving paired FRET samples. Cell seeding and mounting was performed with similar protocol as in FRAP experiments. For live cell imaging cells were placed in the microscope incubator (37 °C, 5% CO₂). Zeiss LSM 780 laser scanning confocal microscope equipped with Plan Apochromat 63x/1.4 oil immersion objective was used for ratiometric FRET approach. FRET imaging and analysis was done by RiFRET method described previously(193). Briefly, the donor and acceptor were excited with a 458 nm line and a 514 nm line, respectively, from a multiline argon laser. The resulting fluorescence was acquired between 465–500 nm for donor emission and 535–650 nm for acceptor emission with a 32-channel QUASAR GaAsP PMT array detector. FRET channel emission was obtained with donor excitation (458 nm) and detected through the acceptor emission channel. Cells stably expressing either donor or acceptor probes alone was used to determine the spectral cross-talk. RiFRET plugin. for ImageJ was used for cross-talk correction of each channel and to calculate pixel by pixel-based apparent FRET efficiency. The apparent FRET efficiency from individual cells prior to and after treatment was used for analysis.

Fluorescence Lifetime Imaging Microscopy (FLIM) -FRET analysis

For FLIM, cells cultured in coverslips were fixed with 4% PFA for 10 mins, washed and stored in PBS at 4°C in dark before imaging. Prior imaging, the coverslips were mounted on imaging chamber and PBS was added to the chamber. Fluorescence lifetime imaging was performed using Leica STELLARIS FALCON confocal microscope equipped with Plan Apochromat 40x/1.25 motCORR glycerol immersion objective. Cells were excited with White Light Laser Stellaris 8 at 450 nm, and fluorescence lifetime times were recorded with HyD X detector, in the range 455 to 495 nm to obtain the photon arrival times specific to donor emission.

The pixel-by-pixel photon arrival times were fitted for bi-exponential decay components using n-Exponential Reconvolution fitting model of Leica LAS X software to obtain mean lifetimes from individual cells.

Statistical Analysis

Statistical significance was measured using an unpaired, two-tailed Student's t-test for data containing two groups. For data involving more than two groups, the Ordinary One-way Analysis of Variance (ANOVA) test was performed in order to obtain the statistical analysis for the data sets concerned. A further comparison of the groups was conducted using the Tukey (HSD) test so as to obtain significant differences between multiple groups. All statistical tests were conducted at a 5% significance level. Prism Graphpad was used for statistical analyses.

6.3. RESULTS

We developed a lamin A strain sensor (Lamin-SS), which consists of an existing FRET force module, known as TSmod(49) with N- and C-terminal lamin A nanobodies(52) (**Figure 26a**). A strain-insensitive truncated control sensor (Lamin SS-T), containing only an N-terminal lamin A nanobody, was also developed (**Figure 26a**). The fluorescence of both sensors was strongly correlated to lamin A/C immunostaining (**Figure 26b**), indicating strong localization to the nuclear lamina. Fluorescence recovery after photobleaching (FRAP) experiments showed that both nanobodies of Lamin-SS can simultaneously bind the nuclear lamina and the dual nanobody binding extends the sensor residence time in the lamina when compared to single nanobody (**Figure 27, 28**). Lamin-SS exhibited a large FRET decrease as compared to Lamin SS-T (**Figure 26c**) indicating an increased distance (strain) between the FRET pair for Lamin-SS. Fluorescence-lifetime imaging microscopy (FLIM) also showed reduced FRET (measured

as increased lifetime) for Lamin-SS, as compared to Lamin-SS-T (**Figure 26d**). Intriguingly both methods showed similar levels of FRET at the nuclear perimeter and in the nucleoplasm, suggesting similar levels of strain for lamin A in each region of the nucleus. Higher FRET for Lamin-SS was observed in lamin KO cells (**Figure 29**), showing that changes in Lamin-SS FRET are dependent on A-type lamins. Additionally, we observed a rapid increase in Lamin-SS FRET ratio during nuclear strain relaxation induced by higher osmolarity of the medium (**Figure 26e and Figure 30**). This data demonstrates that Lamin-SS FRET is inversely related to lamin A strain.

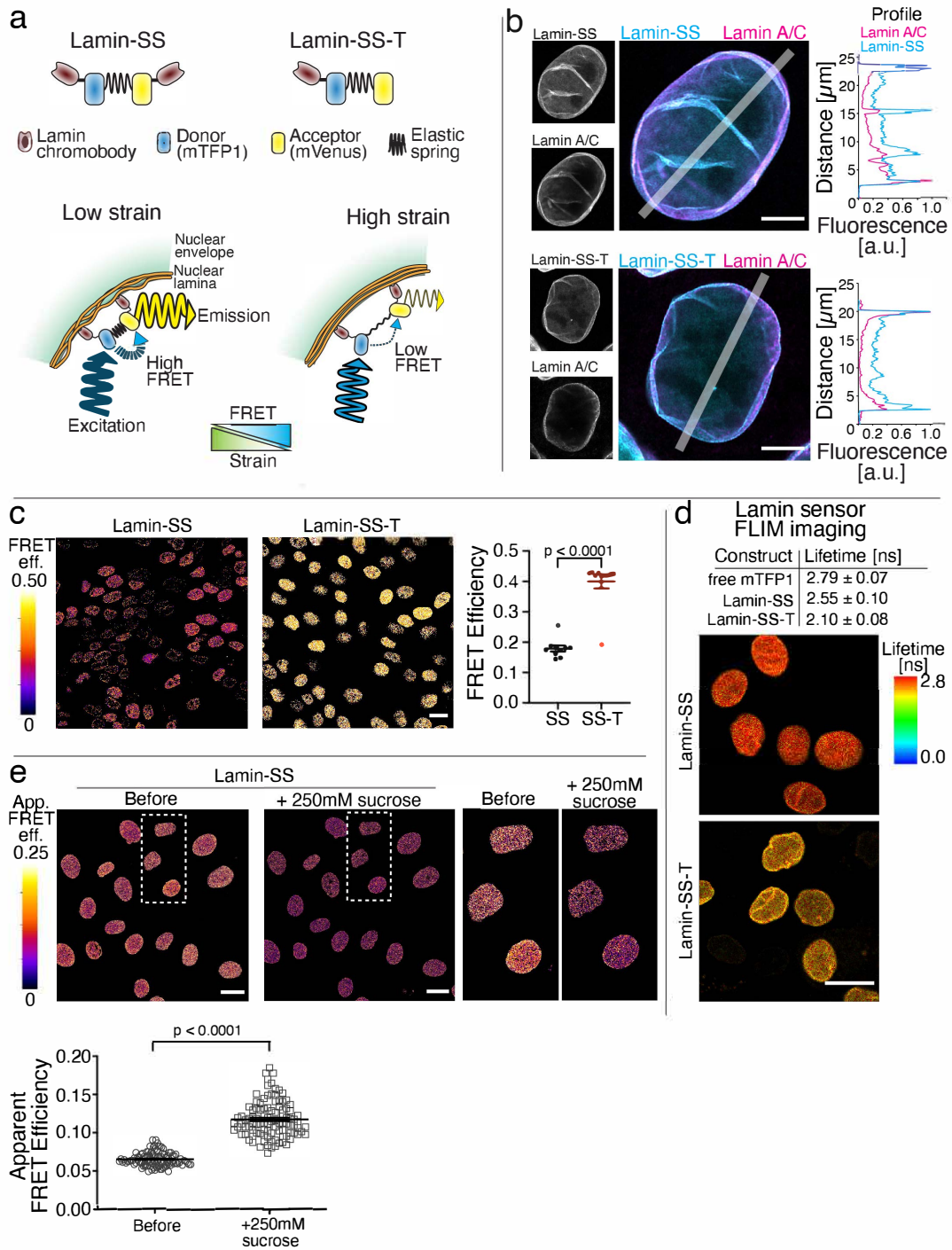


Figure 26: Development and characterization of the FRET based lamin A/C strain sensor.

a, Schematic representation of the FRET based lamin A/C strain sensor (Lamin-SS), truncated control sensor (Lamin-SS-T) and the working mechanism of the strain sensing. **b**, Laser scanning confocal microscopy images (Airy-scan, single sections) of immunolabeled lamin A/C together

with the expressed Lamin-SS or Lamin-SS-T sensor along with corresponding fluorescence line-profiles. Scale bars, 5 μm . **c**, FRET efficiency images and quantified FRET efficiency of Lamin-SS and Lamin-SS-T sensors. The plots represent the median \pm SEM of individual image fields. Lamin-SS had a median FRET efficiency of 17 % compared to Lamin SS-T with 40%. (total n = 10 fields from 3 replicates) Scale bar 20 μm . Unpaired Student's t-tests ($p < 0.0001$). **d**, Donor fluorescence lifetimes of free donor (mTFP1), Lamin-SS and Lamin-SS-T along with FLIM images of Lamin-SS and Lamin-SS-T expressing cells (n=36, n=43 and n=42 cells from 2 replicates). Scale bar 20 μm . **e**, Apparent FRET efficiency images of osmotically stressed Lamin-SS expressing cells together with quantified apparent FRET efficiency. Plot represents the data from a single measurement (total n=304 cells from 3 replicates). Lamin-SS had a mean FRET ratio of 6.4 % in MEM compared to 11.4 % in hyperosmotic conditions (MEM + 250 mM sucrose, 15 min). Paired Student's t-test ($p < 0.0001$). Scale bars, 20 μm .

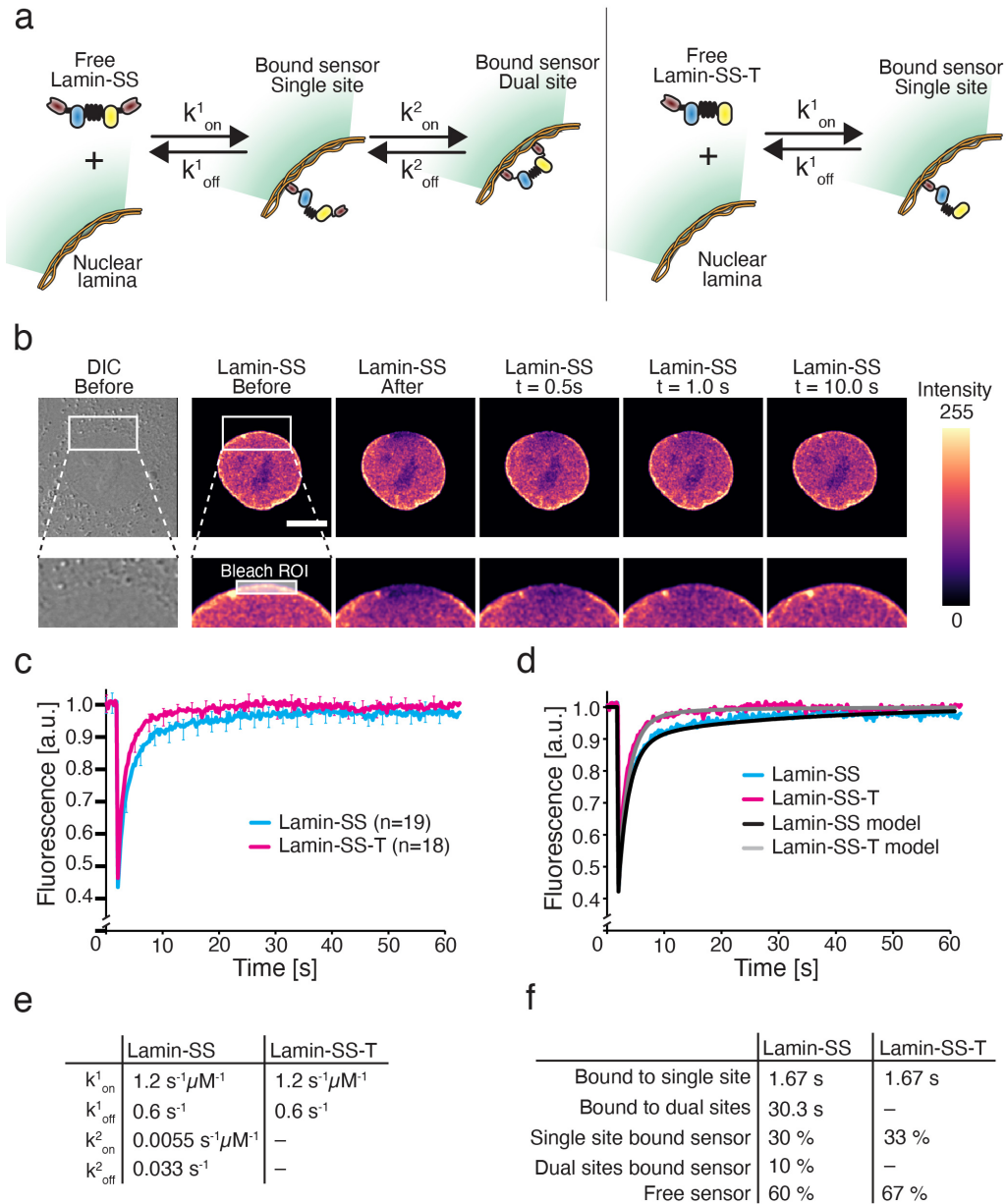


Figure 27: Fluorescence recovery after photobleaching (FRAP) experiments of Lamin-SS and Lamin-SS-T binding to nuclear lamina.

a, Model of the Lamin-SS and Lamin-SS-T binding to nuclear lamina. Binding of Lamin-SS is assumed to proceed sequentially, from the binding of the first nanobody (single site) to the binding of the other (dual site). The release of the sensor from the lamina is modeled to proceed in reverse. Lamin-SS-T binding is limited to single site binding. **b**, FRAP experiment with Lamin-SS

expressing cell. Bleached region of interest (ROI) is marked in the blowup image. The initial recovery is rapid, indicating fast binding dynamics. Scale bar 5 μm . **c**, Quantified and normalized fluorescence recoveries (mean \pm standard deviation) of Lamin-SS and Lamin-SS-T indicating difference in the recovery dynamics (n=19 and n= 18 cells, respectively, from 2 replicates). **d**, Simulated recovery data together with the measured recoveries, see also supplemental figure 2. **e**, Binding pseudo on-rate and off-rate of Lamin-SS and Lamin-SS-T used in the simulations shown in d. **f**, Lamin-SS and Lamin-SS-T binding times and corresponding fractions based on the simulated recoveries.

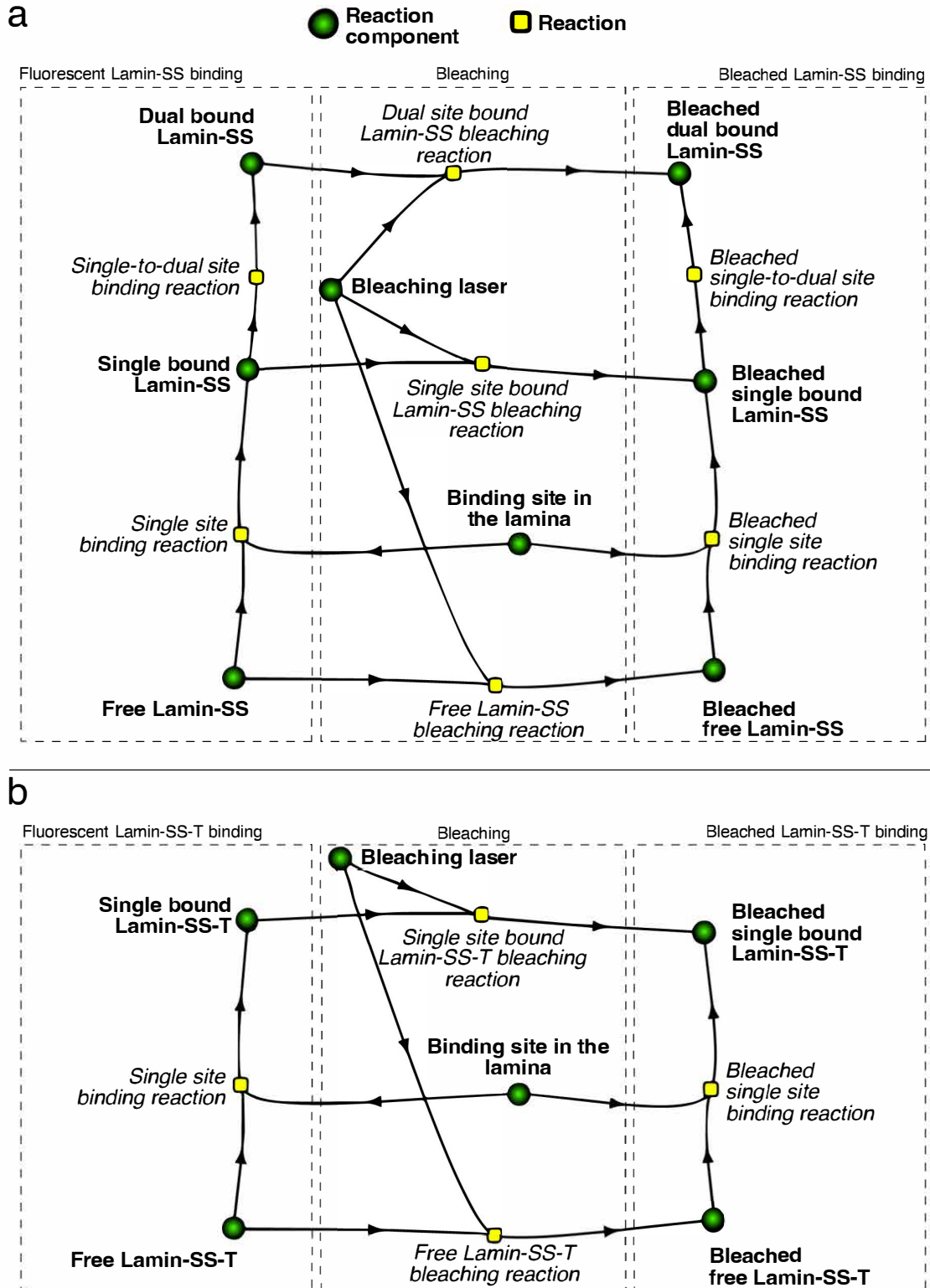


Figure 28: Schematic representation of the simulated FRAP experiment and reactions.

a, Reactions of Lamins-SS during FRAP experiment. Freely diffusing Lamin-SS interacts with a binding site in the nuclear lamina (single site binding reaction) yielding Single bound Lamin-SS. This can further lead into Dual bound Lamin-SS (single-to-dual site binding reaction) or release of the sensor and binding site (reverse of single site binding reaction). Dual bound Lamin-SS can be released by reverse reaction leading into single bound Lamin-SS (reverse of single-to-dual site binding reaction). Bleaching is simulated by a local reaction between Bleaching laser, and free Lamin-SS, Single bound Lamin-SS and Dual bound Lamin-SS. The bleaching leads into appearance of bleached species of Lamin-SS. **b**, Reactions of Lamins-SS-T during FRAP experiment. Truncated sensor binding is limited to the reaction between free Lamin-SS-T and binding site in the lamina, yielding Single bound Lamin-SS-T (single site binding reaction). Similarly, as Lamin-SS, truncated Lamin-SS-T sensor is released, leading to Free Lamin-SS-T and Binding site in the lamina (reverse of Single site binding reaction). Fluorescent Lamin-SS-T molecules are bleached in the Bleaching reactions with Bleaching laser, yielding Bleached single bound Lamin-SS-T and Bleached free Lamin-SS-T.

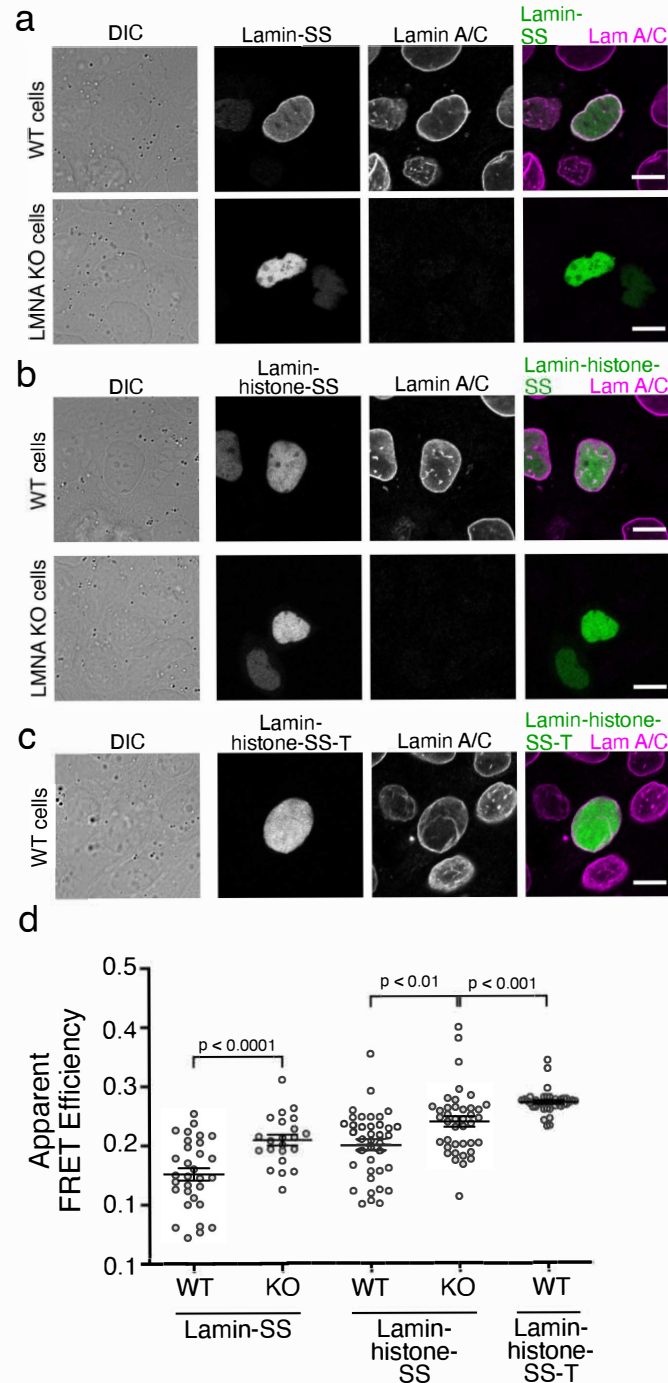


Figure 29: Lamin-SS, Lamin-histone-SS and Lamin-histone-SS-T sensor distribution and apparent FRET efficiency in LMNA KO cells.

a, Wild-type (WT) and LMNA KO cells transiently transfected with Lamin-SS. In LMNA KO cells Lamin-SS localization to nuclear lamina is lost. **b**, WT and LMNA KO cells transiently

transfected with Lamin-histone-SS. **c**, WT cells transiently transfected with Lamin-histone-SS-T. Scale bars 10 μm . **d**, Quantified apparent FRET efficiency (mean \pm SEM) of Lamin-SS and Lamin-histone-SS in WT and LMNA KO cells, and apparent FRET efficiency of Lamin-histone-SS-T in WT cells. Lamin-SS FRET was 0.151 ± 0.010 in WT and 0.209 ± 0.009 in LMNA KO cells (n=31 and n=22, respectively, 2 replicates) (p=0.0001). Lamin-histone-SS FRET was 0.200 ± 0.009 in WT and 0.239 ± 0.008 in LMNA KO cells (n=38 and n=40, respectively, 1 replicate) (p=0.003). Lamin-histone-SS-T FRET was 0.272 ± 0.003 in WT cells (n=38, 1 replicate) (p=0.0008, when compared to Lamin-histone-SS in KO cells). Unpaired Student's t-test.

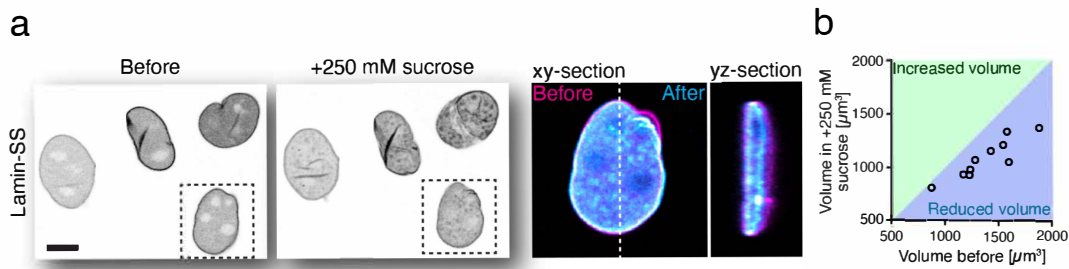


Figure 30: Effect of hyper-osmotic conditions on nuclear morphology and volume.

a, Lamin-SS expressing cells (left) were subjected to hyper-osmotic conditions by adding media containing 250 mM concentration of sucrose for 15 min (middle). Single cell blow-up indicated the change in nuclear morphology before and after the osmotic shock (right). Scale bar 10 μm . **b**, Scatterplot of quantified nuclei volumes indicating clear reduction of the nuclear volume.

As an additional measure of lamin A forces, as well as a proof of concept for the utility of other nanobody based intermolecular sensors, we developed a second sensor to measure

mechanical tension between histone 2A/2B and lamin A (**Figure 31**). This sensor exhibited reduced FRET as compared to a histone 2 truncated sensor and FRET was affected by depletion of A-type lamins (**Figure 29, 31**). This result indicates that mechanical forces can be transduced between chromatin and lamin A.

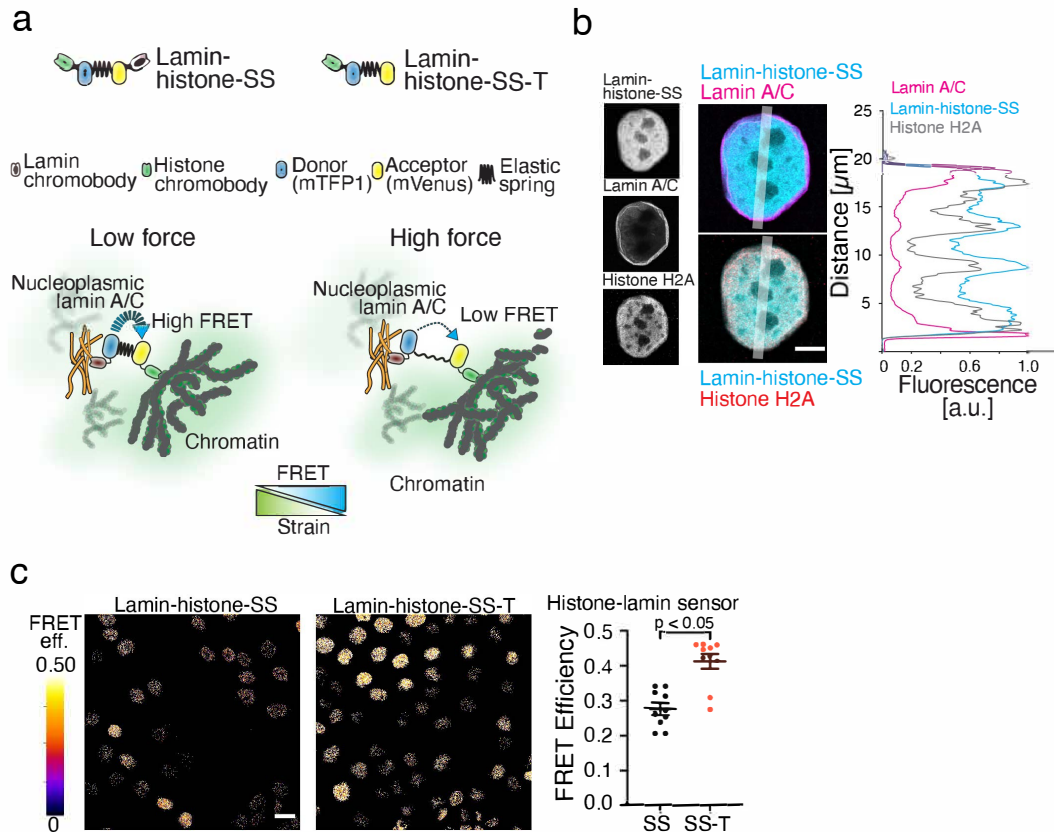


Figure 31: Development and characterization of the FRET based lamin A/C - histone H2A strain sensor.

a, Schematic representation of the FRET based lamin A/C - histone H2A strain sensor (Lamin-histone-SS), truncated control sensor (Lamin-histone-SS-T) and the working mechanism of the force sensing between lamina and chromatin. **b**, Laser scanning confocal microscopy images (Airy-scan, single sections) of immunolabeled lamin A/C, histone H2A and the expressed Lamin-histone-SS sensor along with corresponding fluorescence line-profiles. Scale bar 5 μm . **c**, FRET efficiency images and quantified FRET efficiency of Lamin-histone-SS and Lamin-histone-SS-T sensors. The plots represent the median \pm SEM of individual image fields. Lamin-histone-SS had a median FRET efficiency of 17 % compared to Lamin-histone-SS-T with 40 % (total $n = 10$ from 3 replicates). Scale bar 20 μm . Unpaired Student's t-test ($p < 0.05$).

Next, we sought to identify key cytosolic components which regulate lamin A strain. Using Lamin-SS we observed that actomyosin inhibition with Rock-pathway inhibitor (Y-27632) resulted in decreased strain (increased FRET) (**Figure 32a, b**). Additionally, the sensor was successfully used to temporally analyze lamin A strain changes during actomyosin inhibition (**Figure 32c, d**). Treatment with actin fiber depolymerizing agent (cytochalasin D) also reduced lamin A strain (**Figure 33**). Thus, the intact actin cytoskeleton and myosin contractility regulate lamin A strain. Next, we sought to understand the role of the LINC complex in lamin strains. Disruption of the LINC complex using a dominant negative nesprin construct (DN-KASH) modestly reduced lamin A strain (**Figure 32e, f**).

Additionally, we sought to understand how changes in chromatin structure affect lamin A strain. When chromatin was decondensed by using a histone deacetylase inhibitor (TSA), we detected a significantly decreased Lamin A strain (**Figure 32g, h**). TSA was shown to significantly increase H3K27 acetylation without altering the organization of A-type lamins, detected by labeling specific lamin A/C epitopes (**Figure 34**). TSA treatment also did not affect Lamin-SS binding, as measured by FRAP (**Figure 35**). Chromatin condensation, achieved via histone trimethyl demethylase inhibitor (methylstat), exhibited a small, but non-significant increase in lamin A strain. Similarly, to TSA treatment, methylstat did not affect the A-type lamin organization (**Figure 36**).

Finally, we sought to examine how perturbations in the cell cycle and cell phenotype regulate lamin A strain. When cells were arrested to early S-phase by treatment with DNA polymerase α inhibitor (aphidicolin), we detected decreased lamin A strain (**Figure 32i**). Induction of epithelial to mesenchymal transition (EMT), using TGF- β , also resulted in decreased lamin A strain (**Figure 32j**).

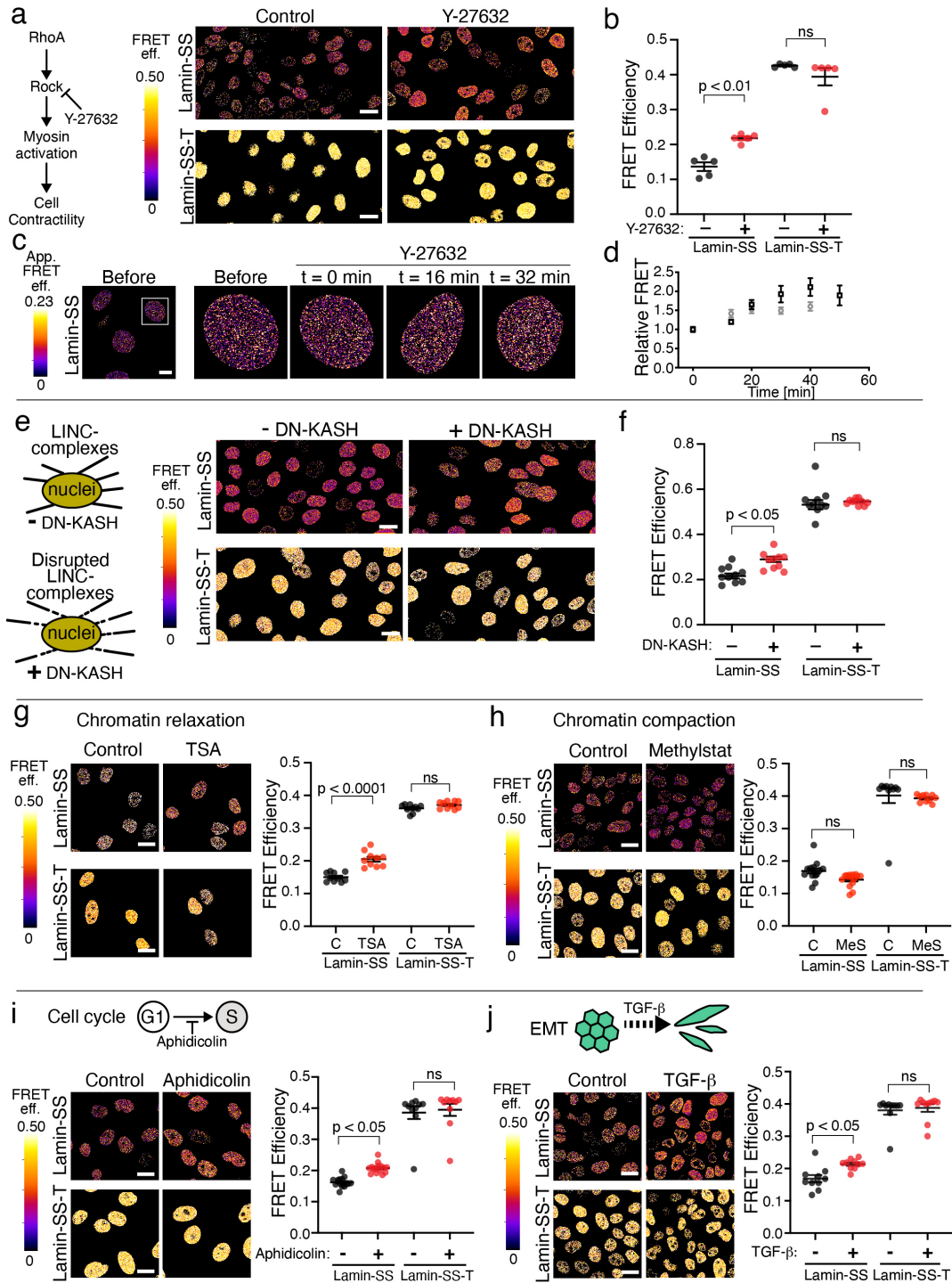


Figure 32: The effect of cellular force transduction and chromatin organization on lamin A/C strain.

a, Cellular contractility was reduced by ROCK-inhibition (Y-27632, 50 μ M, 1 h). FRET efficiency images of Lamin-SS and Lamin-SS-T after inhibition. Scale bars, 20 μ m. **b**, Quantified FRET

efficiency of Lamin-SS and Lamin-SS-T sensors after ROCK-inhibition. FRET efficiency of Lamin-SS was 22 % with Y-27632 and 14 % without treatment. In the same conditions FRET efficiencies were 39 % and 40 % with Lamin-SS-T, respectively. (n = 10 fields from 3 replicates) $p < 0.01$, Unpaired Student's t-test. **c**, Live-cell time lapse apparent FRET efficiency imaging of Lamin-SS during ROCK-inhibition (Y-27632, 50 μM). Scale bar 10 μm . **d**, Quantified relative change (mean \pm SEM) in Lamin-SS FRET ratio during ROCK-inhibition time lapse imaging (n= 152 cells from 2 replicates, black and grey). **e**, LINC-complexes were disrupted by expressing dominant-negative KASH construct (induction for 24h). FRET efficiency images of Lamin-SS and Lamin-SS-T after LINC disruption. Scale bars, 20 μm . **f**, Quantified FRET efficiency of Lamin-SS and Lamin-SS-T after LINC-complex disruption. FRET efficiency of Lamin-SS was 28 % with DN-KASH expression, 22 % without DN-KASH expression. The efficiencies were 53 % and 54 % with Lamin-SS-T, respectively (n =10 from 3 replicates). Unpaired Student's t-test ($p < 0.05$). **g**, Chromatin was relaxed by using histone deacetylase inhibitor (TSA, 200nM μM , 4 h). Images and quantification of Lamin-SS and Lamin-SS-T FRET efficiency after treatment of the cells. FRET efficiency of Lamin-SS was 21 % after TSA treatment, and 15 % without TSA. The efficiencies were 36 % and 37 % with Lamin-SS-T, respectively (n =10 from 3 replicates). Unpaired Student's t-test ($p < 0.0001$). Scale bars 20 μm . **h**, Chromatin was condensed by using histone demethylase inhibitor (methylStat, 2.5 μM , 48 h). Images and quantification of Lamin-SS and Lamin-SS-T FRET efficiency after treatment of the cells. FRET efficiency of Lamin-SS was 14.5 % after methylStat treatment, 18 % without methylstat. The efficiencies were 39 % and 40 % with Lamin-SS-T, respectively. (n = 10 from 3 replicates). Unpaired Student's t-test. Scale bars 20 μm . **i**, Cells were synchronized to early S-phase by blocking DNA polymerase (Aphidicolin, 3 $\mu\text{g}/\text{mL}$, 24 h). Images and quantification of Lamin-SS and Lamin-SS-T FRET efficiency after cell

cycle synchronization. FRET efficiency of Lamin-SS was 21 % after Aphidicolin treatment, 16 % without Aphidicolin. The efficiencies were 39 % and 40 % with Lamin-SS-T, respectively (n =10 from 3 replicates). Unpaired Student's t-test ($p < 0.05$). Scale bars, 20 μm . **j**, EMT was induced by treating cells with a growth factor (TGF- β 1, 2 ng/mL, 24 h). Images and quantification of Lamin-SS and Lamin-SS-T FRET efficiency after EMT induction. FRET efficiency of Lamin-SS was 22 % after TGF- β 1 treatment, 17 % without TGF- β 1. The efficiencies were 39 % and 39 % with Lamin-SS-T, respectively (n =10 from 3 replicates). Unpaired Student's t-test ($p < 0.05$). Scale bars, 20 μm .

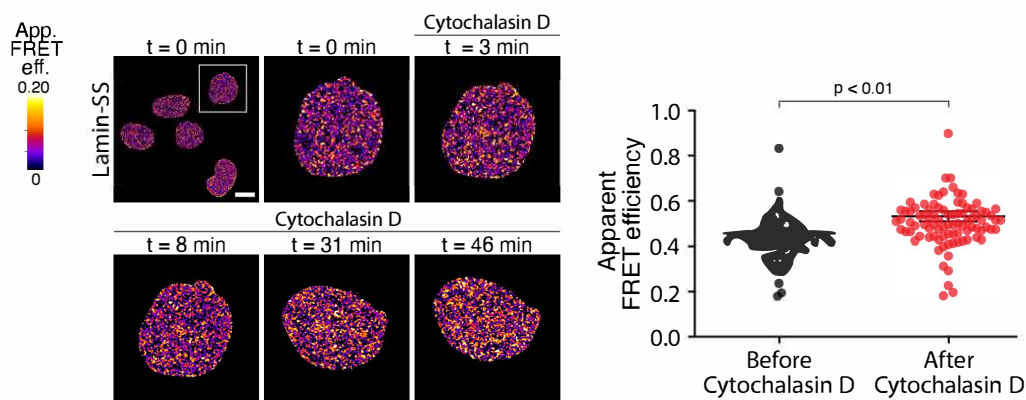


Figure 33: The effect of actin cytoskeleton disruption on Lamin-SS FRET

Live cell imaging of Lamin-SS apparent FRET ratio during actin cytoskeleton disruption by Cytochalasin D (10 $\mu\text{g}/\text{mL}$). Scale bar 5 μm . Blow-up images of single nucleus indicate increase in the FRET. Quantified apparent FRET ratio of the nuclei before and after Cytochalasin D treatment (left). The median FRET ratio increased from 4.3 % before to 5.1 % after the treatment. Student's paired t-test. (n= 92 cells, from 2 biological replicates).

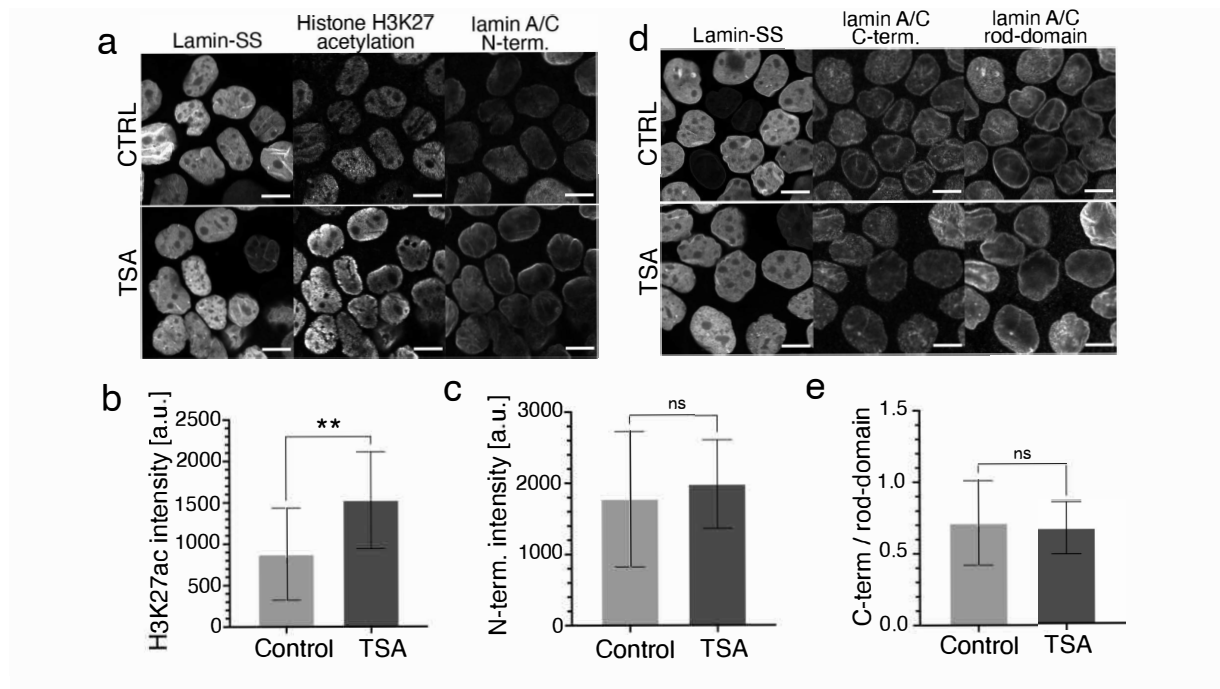


Figure 34: Nuclear lamina organization after chromatin relaxation

a, Laser scanning confocal microscopy maximum intensity projection images of control (upper panels) and trichostatin A (TSA) -treated (600 nM, 4 h, lower panels) Lamin-SS expressing cells, immunolabeled against histone H3 lysine 27 acetylation (H3K27) and N-terminal part of A-type lamins. Scale bars, 10 μ m. **b**, Quantification of nuclear fluorescence intensity of H3K27 acetylation labeling in control and TSA-treated cells (n=159 and n=151 cells, respectively, from 3 biological replicates). In control cells the fluorescence intensity was 877.62 ± 556.12 artificial units (a.u.) (mean \pm standard deviation) and after TSA treatment 1527.06 ± 584.22 a.u. Student's unpaired t-test, $**p=0.004$. **c**, Quantification of nuclear fluorescence intensity of N-terminal nuclear lamin A/C label in control and TSA-treated cells (n= 159 and n=151 cells, respectively, from 3 biological replicates). In control cells the fluorescence intensity was 1774.31 ± 951.68 a.u. and after the TSA treatment 1984.70 ± 621.638 a.u. Student's t-test, $p=0.5$, non-significant (ns). **d**, Laser scanning confocal microscopy maximum intensity projection images of control (upper panels) and TSA-treated (600 nM, 4 h, lower panels) Lamin-SS expressing cells, immunolabeled

against C-terminal part and rod-domain of A-type lamins. Scale bars, 10 μm . **e**, Quantified fluorescence intensity ratio of lamin A/C C-terminus and rod-domain labeling in control and TSA-treated cells ($n=291$ and $n=276$ cells, respectively, from, 3 biological replicates). In control cells the ratio was 0.72 ± 0.30 and in the TSA treated cells 0.69 ± 0.18 . Student's unpaired t-test, $p=0.6$, ns.

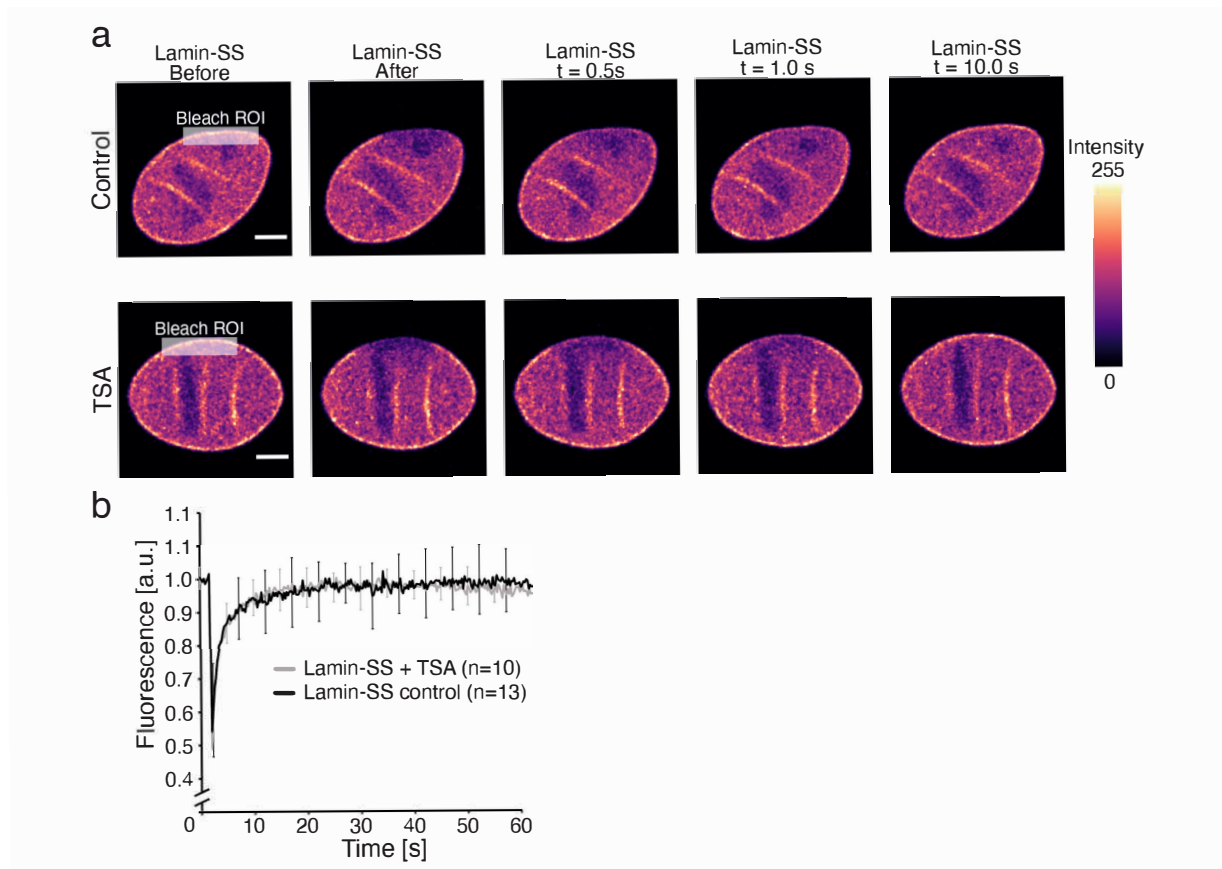


Figure 35: Fluorescence recovery after photobleaching (FRAP) experiments of Lamin-SS after TSA treatment.

a, FRAP experiment with Lamin-SS expressing cells in control (upper panel) and after TSA treatment (600 nM, 4h). Bleached region of interest (ROI) is marked in the image. Scale bar 5 μm .

b, Quantified and normalized fluorescence recoveries (mean \pm standard deviation) of Lamin-SS in control and TSA treated cells ($n=10$ and $n=13$, respectively, from 2 biological replicates).

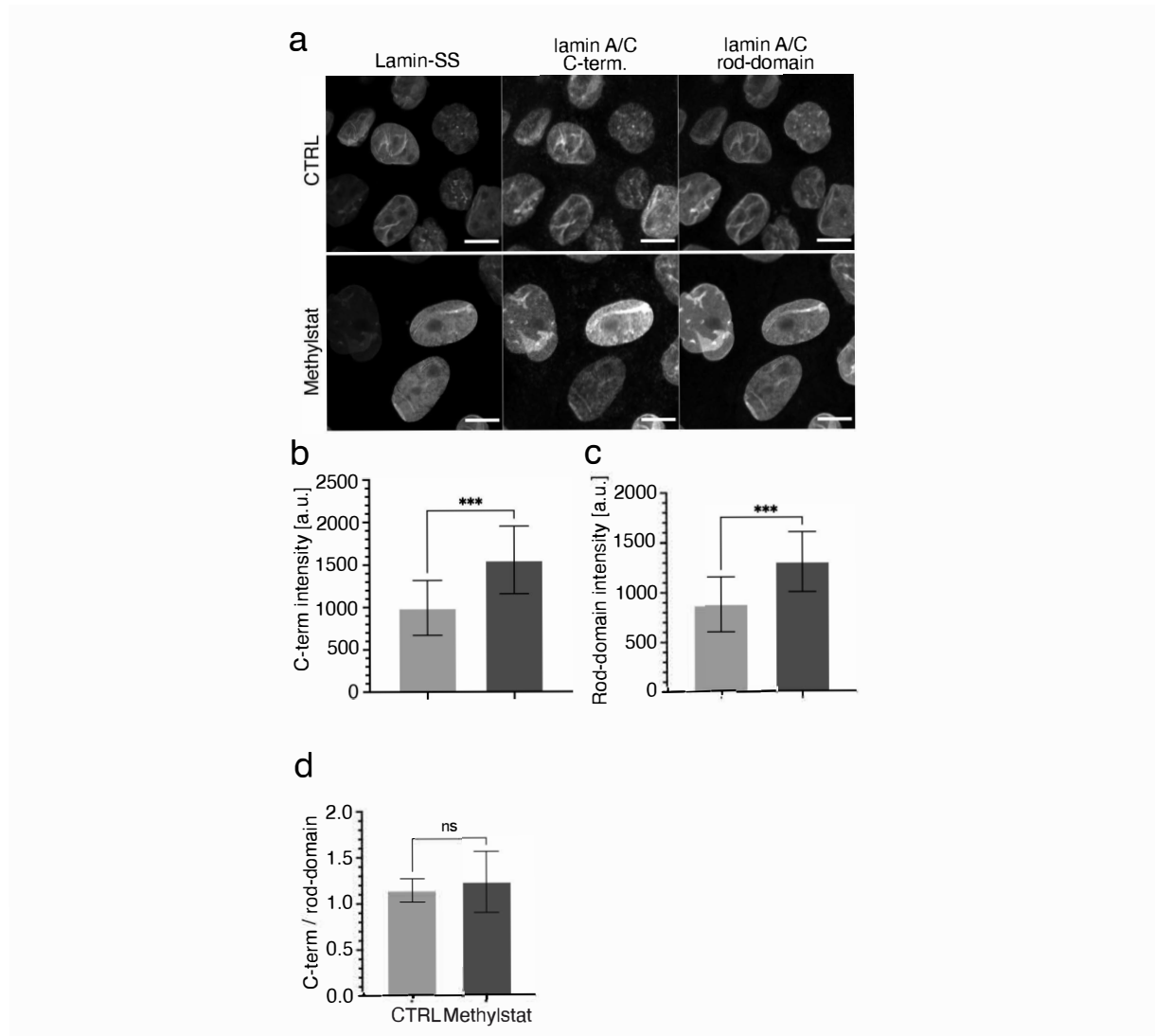


Figure 36: Nuclear lamina organization after chromatin condensation

a, Laser scanning confocal microscopy maximum intensity projection images of control (upper panels) and methylstat -treated (2.5 μ M, 48 h, lower panels) Lamin-SS expressing cells, immunolabeled against lamin A/C C-terminus and rod-domain Scale bars, 10 μ m. **b**, Quantification of nuclear fluorescence intensity of lamin A/C C-terminus labeling in control and methylstat-treated cells (n=244 and n=251 cells, respectively, from 3 biological replicates). In control cells the fluorescence intensity was 992.77 ± 324.17 a.u. and after methylstat treatment 1553.69 ± 397.16 a.u. Student's unpaired t-test, ***p=0.0002. **c**, Quantification of nuclear

fluorescence intensity of lamin A/C rod-domain labeling in control and methylstat-treated cells (n=244 and n=251 cells, respectively, from 3 biological replicates). In control cells the fluorescence intensity was 871.24 ± 275.77 a.u. and after methylstat treatment 1296.36 ± 299.66 a.u. Student's t-test, ***p=0.0004. **d**, Quantified fluorescence intensity ratio of lamin A/C C-terminus and rod-domain labeling (n=244 and n=251 cells, respectively, from 3 biological replicates). In control cells the ratio was 1.14 ± 0.13 and in the methylstat-treated cells 1.22 ± 0.33 . Student's unpaired t-test, p=0.37, ns.

This technical advancement provides significant insight into nuclear mechanics, by providing the first direct measurements of nuclear lamin strain. Lamin strain, presumably the result of tensile and compressive mechanical forces, is dynamic and influenced in both an outside-in (actomyosin, LINC complex) and inside-out (chromatin) manner. Additionally, we show that intranuclear lamins also experience significant levels of strain, providing additional evidence that nucleoplasmic lamins are an important structural element of the nucleus. This work demonstrates the potential for nanobody-based biosensors to be further utilized to measure mechanical strains between proteins.

CHAPTER 7: CONCLUSIONS

My PhD thesis work has contributed to the field of nuclear mechanobiology with several findings. I have provided a better understanding of how changes to structural components of the nucleus effects force transmission and cell response to physiological forces. Insights into how changes to the nucleus effect cell response and adaptation to force will help in studying diseases associated with altered nuclear mechanics including heart disease, muscle dystrophy, progeria, and cancer. In additional I have developed a new novel technique to measure nuclear lamina force and the factors that contribute to said forces. This innovative technological development will allow outstanding questions in the rapidly growing field of nuclear mechanotransduction to be answered.

In chapter 3 I show that the abnormal nuclear morphology observed in HGPS and progerin expression is a consequence of both structure and mechanics. Progerin microaggregate inclusions in the nuclear lamina lead to cellular and multicellular dysfunction. I also show mechanotransmission changes associated with progerin expression in cells under confinement (patterning) and as well as cells under external forces (cyclic stretch). Combined, these studies show that altered nuclear lamina mechanics and microstructure impacts cytoskeletal force transmission through the cell. This study highlights the need for the nuclear lamina to be at an equilibrium in order to sustain force.

In chapter 4 I examined how changes to the nuclear lamina effects endothelial cell adaptation to fluid shear stress. I developed an *in vitro* model of HGPS endothelium by 1) expressing progerin and 2) knockdown of ZMPSTE24 in HUVEC. The results showed that EC either overexpressing progerin or with ZMPSTE24 KD were unable to adapt to shear stress, experiencing significant cell loss. Endothelial cells overexpressing wild-type lamin A also

exhibited similar impairments in adaptation to shear stress, including similar levels of cell loss. Loss of endothelial cells is especially significant in the context of HGPS, as endothelial dysfunction and damage is considered an initial step in the onset of atherosclerosis. These results suggest that abnormal nuclear morphology, caused by a disrupted nuclear lamina, impairs EC adaptation to FSS. In order to improve HGPS nuclear morphology, we treated progerin-expressing cells and ZMPSTE24 KD cells with lonafarnib and Methylstat, which rescued cell loss and resulted in improvements in adaptation to FSS. Collectively this work highlights the nuclear lamina as a critical feature for endothelial adaptability to fluid shear stress.

In chapter 5 I show that changes in chromatin condensation is an important component for how EC adapt to FSS. Using both *in vitro* and *in vivo* models of EC adaptation to FSS, I observed an increase in histone acetylation and a decrease in histone methylation in EC adapted to flow as compared to static. Using small molecule drugs, as well as VEGF, to change chromatin condensation, I show that decreasing chromatin condensation enables cells to more quickly align to FSS, whereas increasing chromatin condensation inhibited alignment. Additionally, I show data that changes in chromatin condensation can also prevent or increase DNA damage, as measured by phosphorylation of γ H2AX. Taken together these results indicate that chromatin condensation is an important aspect of EC adaptation to FSS.

Chapter 6 explains the development of an intermolecular FRET-based biosensor using nanobodies capable of measuring the mechanical strain of nuclear lamin filaments. The innovation of the indirect, antibody-mediated biosensor removes the limitation of disrupting filamentous structures, such as the nuclear lamina. Using the sensor, I determine lamin A/C does experience strain and this strain is influenced by nuclear volume, actomyosin contractility, a functional LINC complex, chromatin condensation state, cell cycle, and EMT. In addition, I

show that lamin A at the nuclear envelope experiences similar strain as lamin A in the nucleoplasm, indicating that nuclearplasmic lamin A is not free floating.

In conclusion, my PhD work as identified two main nuclear structures (lamin a/c and chromatin) that aid in the adaptation and response to physiological levels of shear stress. In addition, I have developed a novel tool to study strain within the nucleus, as well as established the factors causing nuclear lamina strain. My work has contributed to HGPS research, specifically HGPS cardiovascular studies, as well as identified that nuclear shape directly effects nuclear function. I have shown that chromatin condensation plays an important part in endothelial cell adaptation to shear stress, in addition to lamin a/c. Lastly, the development of the lamin a/c strain sensor will aid several nuclear mechanobiology studies in the years to come.

REFERENCES

1. Dahl, K.N., A.J.S. Ribeiro, and J. Lammerding. 2008. Nuclear shape, mechanics, and mechanotransduction. *Circ. Res.* 102:1307–1318.
2. Isermann, P., and J. Lammerding. 2013. Nuclear mechanics and mechanotransduction in health and disease. *Curr. Biol.* 23:R1113–R1121.
3. Maurer, M., and J. Lammerding. 2019. The Driving Force: Nuclear Mechanotransduction in Cellular Function, Fate, and Disease. *Annu. Rev. Biomed. Eng.* 21:443–468.
4. Dreger, M., E. Madrazo, A. Hurlstone, and J. Redondo-Muñoz. 2019. Novel contribution of epigenetic changes to nuclear dynamics. *Nucleus.* 10:42–47.
5. Stephens, A.D., P.Z. Liu, E.J. Banigan, L.M. Almassalha, V. Backman, S.A. Adam, R.D. Goldman, and J.F. Marko. 2018. Chromatin histone modifications and rigidity affect nuclear morphology independent of lamins. *Mol. Biol. Cell.* 29:220–233.
6. Stephens, A.D., E.J. Banigan, S.A. Adam, R.D. Goldman, and J.F. Marko. 2017. Chromatin and lamin A determine two different mechanical response regimes of the cell nucleus. *Mol. Biol. Cell.* 28:1984–1996.
7. Stephens, A.D., E.J. Banigan, and J.F. Marko. 2019. Chromatin’s physical properties shape the nucleus and its functions. *Curr. Opin. Cell Biol.* 58:76–84.
8. Osmanagic-Myers, S., T. Dechat, and R. Foisner. 2015. Lamins at the crossroads of mechanosignaling. *Genes Dev.* 29:225–237.
9. Athirasala, A., N. Hirsch, and A. Buxboim. 2017. Nuclear mechanotransduction: sensing the force from within. *Curr. Opin. Cell Biol.* 46:119–127.
10. Szczesny, S.E., and R.L. Mauck. 2017. The Nuclear Option: Evidence Implicating the Cell Nucleus in Mechanotransduction. *J. Biomech. Eng.* 139:0210061.

11. Enyedi, B., and P. Niethammer. 2016. A Case for the Nuclear Membrane as a Mechanotransducer. *Cell. Mol. Bioeng.* 9:247–251.
12. Ingber, D.E. 2003. Tensegrity II. How structural networks influence cellular information processing networks. *J. Cell Sci.* 116:1397–1408.
13. Orr, A.W., B.P. Helmke, B.R. Blackman, and M.A. Schwartz. 2006. Mechanisms of mechanotransduction. *Dev. Cell.* 10:11–20.
14. Guilluy, C., L.D. Osborne, L. Van Landeghem, L. Sharek, R. Superfine, R. Garcia-Mata, and K. Burrige. 2014. Isolated nuclei adapt to force and reveal a mechanotransduction pathway in the nucleus. *Nat. Cell Biol.* 16:376–381.
15. Guilluy, C., and K. Burrige. 2015. Nuclear mechanotransduction: Forcing the nucleus to respond. *Nucleus.* 6:19–22.
16. Cho, S., J. Irianto, and D.E. Discher. 2017. Mechanosensing by the nucleus: From pathways to scaling relationships. *J. Cell Biol.* 216:305–315.
17. Szczesny, S.E., and R.L. Mauck. 2017. The Nuclear Option: Evidence Implicating the Cell Nucleus in Mechanotransduction. *J. Biomech. Eng.* 139.
18. Kirby, T.J., and J. Lammerding. 2018. Emerging views of the nucleus as a cellular mechanosensor. *Nat. Cell Biol.* 20:373–381.
19. Rowat, A.C., L.J. Foster, M.M. Nielsen, M. Weiss, and J.H. Ipsen. 2005. Characterization of the elastic properties of the nuclear envelope. *J. R. Soc. Interface.* 2:63–69.
20. Ungricht, R., and U. Kutay. 2017. Mechanisms and functions of nuclear envelope remodelling. *Nat. Rev. Mol. Cell Biol.* 18:229–245.
21. Bouzid, T., E. Kim, B.D. Riehl, A.M. Esfahani, J. Rosenbohm, R. Yang, B. Duan, and J.Y. Lim. 2019. The LINC complex, mechanotransduction, and mesenchymal stem cell

- function and fate. *J. Biol. Eng.* 13:1–12.
22. Buchwalter, A., J.M. Kaneshiro, and M.W. Hetzer. 2019. Coaching from the sidelines: the nuclear periphery in genome regulation. *Nat. Rev. Genet.* 20:39–50.
 23. Segura-Totten, M., A.K. Kowalski, R. Craigie, and K.L. Wilson. 2002. Barrier-to-autointegration factor: Major roles in chromatin decondensation and nuclear assembly. *J. Cell Biol.* 158:475–485.
 24. Constantinescu, D., H.L. Gray, P.J. Sammak, G.P. Schatten, and A.B. Csoka. 2006. Lamin A/C Expression Is a Marker of Mouse and Human Embryonic Stem Cell Differentiation. *Stem Cells.* 24:177–185.
 25. Krohne, G., and R. Benavente. 1986. The nuclear lamins. A multigene family of proteins in evolution and differentiation. *Exp. Cell Res.* 162:1–10.
 26. Hutchison, C.J., and H.J. Worman. 2004. A-type lamins: Guardians of the soma? *Nat. Cell Biol.* 6:1062–1067.
 27. Burke, B., and C.L. Stewart. 2014. Functional architecture of the cell's nucleus in development, aging, and disease. In: *Current Topics in Developmental Biology*. Academic Press Inc. pp. 1–52.
 28. Gruenbaum, Y., and O. Medalia. 2015. Lamins: The structure and protein complexes. *Curr. Opin. Cell Biol.* 32:7–12.
 29. Gruenbaum, Y., and R. Foisner. 2015. Lamins: Nuclear intermediate filament proteins with fundamental functions in nuclear mechanics and genome regulation. *Annu. Rev. Biochem.* 84:131–164.
 30. Gurudatta, B. V., L.S. Shashidhara, and V.K. Parnaik. 2010. Lamin C and chromatin organization in *Drosophila*. *J. Genet.* 89:37–49.

31. Kourmouli, N., G. Dialynas, C. Petraki, A. Pырpasopoulou, P.B. Singh, S.D. Georgatos, and P.A. Theodoropoulos. 2001. Binding of Heterochromatin Protein 1 to the Nuclear Envelope Is Regulated by a Soluble Form of Tubulin. *J. Biol. Chem.* 276:13007–13014.
32. Goldman, R.D., Y. Gruenbaum, R.D. Moir, D.K. Shumaker, and T.P. Spann. 2002. Nuclear lamins: Building blocks of nuclear architecture. *Genes Dev.* 16:533–547.
33. Holaska, J.M., K.K. Lee, A.K. Kowalski, and K.L. Wilson. 2003. Transcriptional repressor germ cell-less (GCL) and barrier to autointegration factor (BAF) compete for binding to emerin in vitro. *J. Biol. Chem.* 278:6969–6975.
34. van Steensel, B., and A.S. Belmont. 2017. Lamina-Associated Domains: Links with Chromosome Architecture, Heterochromatin, and Gene Repression. *Cell.* 169.
35. Butin-Israeli, V., S.A. Adam, A.E. Goldman, and R.D. Goldman. 2012. Nuclear lamin functions and disease. *Trends Genet.* 28:464–471.
36. Dreger, M., E. Madrazo, A. Hurlstone, and J. Redondo-Muñoz. 2019. Novel contribution of epigenetic changes to nuclear dynamics. *Nucleus.* 10:42–47.
37. Tamashunas, A.C., V.J. Tocco, J. Matthews, Q. Zhang, K.R. Atanasova, L. Paschall, S. Pathak, R. Ratnayake, A.D. Stephens, H. Luesch, J.D. Licht, and T.P. Lele. 2020. High-throughput gene screen reveals modulators of nuclear shape. *Mol. Biol. Cell.* 31:1392–1402.
38. Pajerowski JD, Dahl KN, Zhong FL, Sammak PJ, D.D. 2007. Physical plasticity of the nucleus in stem cell differentiation. *PNAS.*
39. Schreiner, S.M., P.K. Koo, Y. Zhao, S.G.J. Mochrie, and M.C. King. 2015. The tethering of chromatin to the nuclear envelope supports nuclear mechanics. *Nat. Commun.* 6:1–13.
40. Hobson, C.M., M. Kern, E. Timothy O'brien Iii, A.D. Stephens, M.R. Falvo, and R.

- Superfine. 2020. Correlating nuclear morphology and external force with combined atomic force microscopy and light sheet imaging separates roles of chromatin and lamin A/C in nuclear mechanics. *bioRxiv*. 2020.02.10.942581.
41. Dahl, K.N., P. Scaffidi, M.F. Islam, A.G. Yodh, K.L. Wilson, and T. Misteli. 2006. Distinct structural and mechanical properties of the nuclear lamina in Hutchinson-Gilford progeria syndrome. *Proc. Natl. Acad. Sci. U. S. A.* 103:10271–10276.
 42. Booth, E.A., S.T. Spagnol, T.A. Alcoser, and K.N. Dahl. 2015. Nuclear stiffening and chromatin softening with progerin expression leads to an attenuated nuclear response to force. *Soft Matter*. 11:6412–6418.
 43. Goldman, R.D., D.K. Shumaker, M.R. Erdos, M. Eriksson, A.E. Goldman, L.B. Gordon, Y. Gruenbaum, S. Khuon, M. Mendez, R. Varga, and F.S. Collins. 2004. Accumulation of mutant lamin A progressive changes in nuclear architecture in Hutchinson-Gilford progeria syndrome. *Proc. Natl. Acad. Sci. U. S. A.* 101:8963–8968.
 44. Valerie L.R.M. Verstraeten^{1,2,3,*}, Julie Y. Ji^{1,*}, Kiersten S. Cummings¹, Richard T. Lee¹, and J.L. 2008. Increased mechanosensitivity and nuclear stiffness in Hutchinson-Gilford progeria cells: Effects of farnesyltransferase inhibitors. *Aging Cell*. 383–393.
 45. Shumaker, D.K., T. Dechat, A. Kohlmaier, S.A. Adam, M.R. Bozovsky, M.R. Erdos, M. Eriksson, A.E. Goldman, S. Khuon, F.S. Collins, T. Jenuwein, and R.D. Goldman. 2006. Mutant nuclear lamin A leads to progressive alterations of epigenetic control in premature aging. *Proc. Natl. Acad. Sci. U. S. A.* 103:8703–8708.
 46. Pitrez, P.R., S.C. Rosa, C. Praça, and L. Ferreira. 2016. Vascular disease modeling using induced pluripotent stem cells: Focus in Hutchinson-Gilford Progeria Syndrome. *Biochem. Biophys. Res. Commun.* 473:710–718.

47. Fischer, L.S., S. Rangarajan, T. Sadhanasatish, and C. Grashoff. 2021. Molecular Force Measurement with Tension Sensors. <https://doi.org/10.1146/annurev-biophys-101920-064756>. 50:595–616.
48. Meng, F., and F. Sachs. 2011. Visualizing dynamic cytoplasmic forces with a compliance-matched FRET sensor. *J. Cell Sci.* 124:261–269.
49. Grashoff, C., B.D. Hoffman, M.D. Brenner, R. Zhou, M. Parsons, M.T. Yang, M.A. McLean, S.G. Sligar, C.S. Chen, T. Ha, and M.A. Schwartz. 2010. Measuring mechanical tension across vinculin reveals regulation of focal adhesion dynamics. *Nature*. 466:263–266.
50. Narayanan, V., L.E. Schappell, C.R. Mayer, A.A. Duke, T.J. Armiger, P.T. Arsenovic, A. Mohan, K.N. Dahl, J.P. Gleghorn, and D.E. Conway. 2020. Osmotic Gradients in Epithelial Acini Increase Mechanical Tension across E-cadherin, Drive Morphogenesis, and Maintain Homeostasis. *Curr. Biol.* 30:624-633.e4.
51. Mohan, A., K.T. Schlue, A.F. Kniffin, C.R. Mayer, A.A. Duke, V. Narayanan, P.T. Arsenovic, K. Bathula, B.E. Danielsson, S.P. Dumbali, V. Maruthamuthu, and D.E. Conway. 2018. Spatial Proliferation of Epithelial Cells Is Regulated by E-Cadherin Force. *Biophys. J.* 115:853–864.
52. Rothbauer, U., K. Zolghadr, S. Tillib, D. Nowak, L. Schermelleh, A. Gahl, N. Backmann, K. Conrath, S. Muyltermans, M.C. Cardoso, and H. Leonhardt. 2006. Targeting and tracing antigens in live cells with fluorescent nanobodies. *Nat. Methods*. 3:887–889.
53. Panza, P., J. Maier, C. Schmees, U. Rothbauer, and C. Söllner. 2015. Live imaging of endogenous protein dynamics in zebrafish using chromobodies. *Dev.* 142:1879–1884.
54. Shimia, T., M. Kittisopikul, J. Tran, A.E. Goldman, S.A. Adam, Y. Zheng, K. Jaqaman,

- and R.D. Goldman. 2015. Structural organization of nuclear lamins A, C, B1, and B2 revealed by superresolution microscopy. *Mol. Biol. Cell.* 26:4075–4086.
55. Turgay, Y., M. Eibauer, A.E. Goldman, T. Shimi, M. Khayat, K. Ben-Harush, A. Dubrovsky-Gaupp, K.T. Sapra, R.D. Goldman, and O. Medalia. 2017. The molecular architecture of lamins in somatic cells. *Nature.* 543:261–264.
56. Nmezi, B., J. Xu, R. Fu, T.J. Armiger, G. Rodriguez-Bey, J.S. Powell, H. Ma, M. Sullivan, Y. Tu, N.Y. Chen, S.G. Young, D.B. Stolz, K.N. Dahl, Y. Liu, and Q.S. Padiath. 2019. Concentric organization of A- and B-type lamins predicts their distinct roles in the spatial organization and stability of the nuclear lamina. *Proc. Natl. Acad. Sci.* 116:4307–4315.
57. Xie, W., A. Chojnowski, T. Boudier, J.Y. Lim, S. Ahmed, Z. Ser, C. Stewart, and B. Burke. 2016. A-type Lamins Form Distinct Filamentous Networks with Differential Nuclear Pore Complex Associations. *Curr. Biol.* 26:2651–2658.
58. A, D.S.-G., B. R, C. P, N. C, A. J, B. I, L. S, S. CL, M. A, L.M. M, and L. N. 2003. Lamin a truncation in Hutchinson-Gilford progeria. *Science.* 300:2055.
59. Scaffidi, P. 2006. Good news in the nuclear envelope: loss of lamin A might be a gain. *J. Clin. Invest.* 116:632–634.
60. DAHL, K.N., A. KALINOWSKI, and K. PEKKAN. 2010. Mechanobiology and the Microcirculation: Cellular, Nuclear and Fluid Mechanics. *Microcirculation.* 17:179–191.
61. Ferri, G., B. Storti, and R. Bizzarri. 2017. Nucleocytoplasmic transport in cells with progerin-induced defective nuclear lamina. *Biophys. Chem.* 229:77–83.
62. Choi, S., W. Wang, A.J.S. Ribeiro, A. Kalinowski, S.Q. Gregg, P.L. Opresko, L.J. Niedernhofer, G.K. Rohde, and K.N. Dahl. 2011. Computational image analysis of

- nuclear morphology associated with various nuclear-specific aging disorders. *Nucleus*. 2:570–579.
63. Scaffidi, P., and T. Misteli. 2005. Reversal of the cellular phenotype in the premature aging disease Hutchinson-Gilford progeria syndrome. *Nat. Med.* 11:440–445.
 64. Cao, K., B.C. Capell, M.R. Erdos, K. Djabali, and F.S. Collins. 2007. A lamin A protein isoform overexpressed in Hutchinson-Gilford progeria syndrome interferes with mitosis in progeria and normal cells. *Proc. Natl. Acad. Sci.* 104:4949–4954.
 65. Eisch, V., X. Lu, D. Gabriel, and K. Djabali. 2016. Progerin impairs chromosome maintenance by depleting {CENP}-F from metaphase kinetochores in Hutchinson-Gilford progeria fibroblasts. *Oncotarget*. 7:24700–24718.
 66. Capell, B.C., M.R. Erdos, J.P. Madigan, J.J. Fiordalisi, R. Varga, K.N. Conneely, L.B. Gordon, C.J. Der, A.D. Cox, and F.S. Collins. 2005. Inhibiting farnesylation of progerin prevents the characteristic nuclear blebbing of Hutchinson-Gilford progeria syndrome. *Proc. Natl. Acad. Sci. U. S. A.* 102:12879–12884.
 67. Datta, S., C.J. Snow, and B.M. Paschal. 2014. A pathway linking oxidative stress and the Ran GTPase system in progeria. *Mol. Biol. Cell.* 25:1202–1215.
 68. Arsenovic, P.T., I. Ramachandran, K. Bathula, R. Zhu, J.D. Narang, N.A. Noll, C.A. Lemmon, G.G. Gundersen, and D.E. Conway. 2016. Nesprin-2G, a Component of the Nuclear LINC Complex, Is Subject to Myosin-Dependent Tension. *Biophys. J.* 110:34–43.
 69. Vaziri, A., and M.R.K. Mofrad. 2007. Mechanics and deformation of the nucleus in micropipette aspiration experiment. *J. Biomech.* 40:2053–2062.
 70. Qin, Z., A. Kalinowski, K.N. Dahl, and M.J. Buehler. 2011. Structure and stability of the lamin A tail domain and {HGPS} mutant. *J. Struct. Biol.* 175:425–433.

71. Kalinowski, A., Z. Qin, K. Coffey, R. Kodali, M. Buehler, M. Lösche, and K. Dahl. 2013. Calcium Causes a Conformational Change in Lamin A Tail Domain that Promotes Farnesyl-Mediated Membrane Association. *Biophys. J.* 104:2246–2253.
72. Versaevel, M., T. Grevesse, and S. Gabriele. 2012. Spatial coordination between cell and nuclear shape within micropatterned endothelial cells. *Nat. Commun.* 3.
73. Hale, C.M., A.L. Shrestha, S.B. Khatau, P.J. Stewart-Hutchinson, L. Hernandez, C.L. Stewart, D. Hodzic, and D. Wirtz. 2008. Dysfunctional Connections Between the Nucleus and the Actin and Microtubule Networks in Laminopathic Models. *Biophys. J.* 95:5462–5475.
74. Steward, R.L., C.-M. Cheng, D.L. Wang, and P.R. LeDuc. 2009. Probing Cell Structure Responses Through a Shear and Stretching Mechanical Stimulation Technique. *Cell Biochem. Biophys.* 56:115–124.
75. Lee, C.-F., C. Haase, S. Deguchi, and R. Kaunas. 2010. Cyclic stretch-induced stress fiber dynamics {textendash} Dependence on strain rate, Rho-kinase and {MLCK}. *Biochem. Biophys. Res. Commun.* 401:344–349.
76. Dreesen, O., P.F. Ong, A. Chojnowski, and A. Colman. 2013. The contrasting roles of lamin B1 in cellular aging and human disease. *Nucleus.* 4:283–290.
77. Bruston, F., E. Delbarre, C. Östlund, H.J. Worman, B. Buendia, and I. Duband-Goulet. 2010. Loss of a {DNA} binding site within the tail of prelamin A contributes to altered heterochromatin anchorage by progerin. *{FEBS} Lett.* 584:2999–3004.
78. Chojnowski, A., P.F. Ong, E.S.M. Wong, J.S.Y. Lim, R.A. Mutalif, R. Navasankari, B. Dutta, H. Yang, Y.Y. Liow, S.K. Sze, T. Boudier, G.D. Wright, A. Colman, B. Burke, C.L. Stewart, and O. Dreesen. 2015. Progerin reduces {LAP}2^{upalpha}-telomere

- association in Hutchinson-Gilford progeria. *Elife*. 4.
79. Kelley, J.B., S. Datta, C.J. Snow, M. Chatterjee, L. Ni, A. Spencer, C.-S. Yang, C. Cubeñas-Potts, M.J. Matunis, and B.M. Paschal. 2011. The Defective Nuclear Lamina in Hutchinson-Gilford Progeria Syndrome Disrupts the Nucleocytoplasmic Ran Gradient and Inhibits Nuclear Localization of Ubc9. *Mol. Cell. Biol.* 31:3378–3395.
 80. Lüke, Y., H. Zaim, I. Karakesisoglou, V.M. Jaeger, L. Sellin, W. Lu, M. Schneider, S. Neumann, A. Beijer, M. Munck, V.C. Padmakumar, J. Gloy, G. Walz, and A.A. Noegel. 2008. Nesprin-2 Giant (NUANCE) maintains nuclear envelope architecture and composition in skin. *J. Cell Sci.* 121:1887–1898.
 81. Pflgebraar, K.B., P. Taimen, V. Butin-Israeli, T. Shimi, S. Langer-Freitag, Y. Markaki, A.E. Goldman, M. Wehnert, and R.D. Goldman. 2015. Gene-rich chromosomal regions are preferentially localized in the lamin B deficient nuclear blebs of atypical progeria cells. *Nucleus*. 6:66–76.
 82. Funkhouser, C.M., R. Sknepnek, T. Shimi, A.E. Goldman, R.D. Goldman, and M.O. de la Cruz. 2013. Mechanical model of blebbing in nuclear lamin meshworks. *Proc. Natl. Acad. Sci.* 110:3248–3253.
 83. NS, W., Z. Z, S. RS, and D. KN. 2012. Modeling nuclear blebs in a nucleoskeleton of independent filament networks. *Cell. Mol. Bioeng.* 5:73–81.
 84. Israelachvili, J.N. 2011. Strong Intermolecular Forces. In: Intermolecular and Surface Forces. Elsevier. pp. 53–70.
 85. Dahl, K.N., A.J. Engler, J.D. Pajerowski, and D.E. Discher. 2005. Power-Law Rheology of Isolated Nuclei with Deformation Mapping of Nuclear Substructures. *Biophys. J.* 89:2855–2864.

86. Dahl, K.N., S.M. Kahn, K.L. Wilson, and D.E. Discher. 2004. The nuclear envelope lamina network has elasticity and a compressibility limit suggestive of a molecular shock absorber. *J. Cell Sci.* 117:4779–4786.
87. Rowat, A.C., J. Lammerding, and J.H. Ipsen. 2006. Mechanical properties of the cell nucleus and the effect of emerin deficiency. *Biophys. J.* 91:4649–4664.
88. Kim, D.-H., B. Li, F. Si, J. Philips, D. Wirtz, and S.X. Sun. 2015. Volume regulation and shape bifurcation in the cell nucleus. *J. Cell Sci.*
89. Qin, Z., and M.J. Buehler. 2011. Flaw Tolerance of Nuclear Intermediate Filament Lamina under Extreme Mechanical Deformation. *{ACS} Nano.* 5:3034–3042.
90. Kaminski, A., G.R. Fedorchak, and J. Lammerding. 2014. The Cellular Mastermind(?)\textemdash}Mechanotransduction and the Nucleus. In: *Progress in Molecular Biology and Translational Science.* Elsevier. pp. 157–203.
91. Neelam, S., R.B. Dickinson, and T.P. Lele. 2016. New approaches for understanding the nuclear force balance in living, adherent cells. *Methods.* 94:27–32.
92. Spagnol, S.T., and K.N. Dahl. 2014. Active cytoskeletal force and chromatin condensation independently modulate intranuclear network fluctuations. *Integr. Biol. (United Kingdom).* 6:523–531.
93. Alam, S.G., D. Lovett, D.I. Kim, K.J. Roux, R.B. Dickinson, and T.P. Lele. 2015. The nucleus is an intracellular propagator of tensile forces in {NIH} 3T3 fibroblasts. *J. Cell Sci.* 128:1901–1911.
94. Scaffidi, P., and T. Misteli. 2006. Lamin A-Dependent Nuclear Defects in Human Aging. *Science (80-.).* 312:1059–1063.
95. Eriksson, M., W.T. Brown, L.B. Gordon, M.W. Glynn, J. Singer, L. Scott, M.R. Erdos,

- C.M. Robbins, T.Y. Moses, P. Berglund, A. Dutra, E. Pak, S. Durkin, A.B. Csoka, M. Boehnke, T.W. Glover, and F.S. Collins. 2003. Recurrent de novo point mutations in lamin A cause Hutchinson–Gilford progeria syndrome. *Nat.* 2003 4236937. 423:293–298.
96. MO, B., G. B, R. J, S. WK, H. C, K. LV, M. A, M. M, G. H, J. Y, W. ER, V.B. N, C. RA, M. S, G. SM, and Y. SG. 2002. Zmpste24 deficiency in mice causes spontaneous bone fractures, muscle weakness, and a prelamin A processing defect. *Proc. Natl. Acad. Sci. U. S. A.* 99:13049–13054.
97. LG, F., N. JK, M. M, C. N, Y. SH, S. CL, S. T, B. A, M. S, R. K, B. MO, and Y. SG. 2004. Heterozygosity for Lmna deficiency eliminates the progeria-like phenotypes in Zmpste24-deficient mice. *Proc. Natl. Acad. Sci. U. S. A.* 101:18111–18116.
98. Verstraeten, V.L.R.M., J.Y. Ji, K.S. Cummings, R.T. Lee, and J. Lammerding. 2008. Increased mechanosensitivity and nuclear stiffness in Hutchinson-Gilford progeria cells: Effects of farnesyltransferase inhibitors. *Aging Cell.* 7:383–393.
99. Baker, P.B., N. Baba, and C.P. Boesel. 1981. Cardiovascular abnormalities in progeria. Case report and review of the literature. *Arch. Pathol. Lab. Med.* 105:384–386.
100. M, O., H. I, M. R, B. JK, D. K, C. K, E. MR, B. C, F. B, S. L, G.-H. M, M. JT, K. R, V. R, C. FS, W. TN, N. EG, and G. LB. 2010. Cardiovascular pathology in Hutchinson-Gilford progeria: correlation with the vascular pathology of aging. *Arterioscler. Thromb. Vasc. Biol.* 30:2301–2309.
101. AM, A., C. AB, B. A, J. T, R. S, M. A, and Z. A. 2015. Signaling pathway activation drift during aging: Hutchinson-Gilford Progeria Syndrome fibroblasts are comparable to normal middle-age and old-age cells. *Aging (Albany. NY).* 7:26–37.
102. Gonzalo, S., R. Kreienkamp, and P. Askjaer. 2017. Hutchinson-Gilford Progeria

- Syndrome: A premature aging disease caused by LMNA gene mutations. *Ageing Res. Rev.* 33:18–29.
103. Gordon, L.B., I.A. Harten, M.E. Patti, and A.H. Lichtenstein. 2005. Reduced adiponectin and HDL cholesterol without elevated C-reactive protein: Clues to the biology of premature atherosclerosis in Hutchinson-Gilford Progeria Syndrome. *J. Pediatr.* 146:336–341.
104. Gerhard-herman, M., L.B. Smoot, N. Wake, M.W. Kieran, E. Monica, D.T. Miller, A. Schwartzman, A. Giobbie-hurder, D. Neuberg, and L.B. Gordon. 2012. Mechanisms of premature vascular aging in child. *Hypertension.* 59:92–97.
105. WE, S., D. B, S. T, and G.-B. E. 2001. Smooth muscle cell depletion and collagen types in progeric arteries. *Cardiovasc. Pathol.* 10:133–136.
106. Zhang, H., Z.M. Xiong, and K. Cao. 2014. Mechanisms controlling the smooth muscle cell death in progeria via down-regulation of poly(ADP-ribose) polymerase 1. *Proc. Natl. Acad. Sci. U. S. A.* 111.
107. Ribas, J., Y.S. Zhang, P.R. Pitrez, J. Leijten, M. Miscuglio, J. Rouwkema, M.R. Dokmeci, X. Nissan, L. Ferreira, and A. Khademhosseini. 2017. Biomechanical Strain Exacerbates Inflammation on a Progeria-on-a-Chip Model. *Small.* 13:1–13.
108. Kim, P.H., J. Luu, P. Heizer, Y. Tu, T.A. Weston, N. Chen, C. Lim, R.L. Li, P.Y. Lin, J.C.Y. Dunn, D. Hodzic, S.G. Young, and L.G. Fong. 2018. Disrupting the LINC complex in smooth muscle cells reduces aortic disease in a mouse model of Hutchinson-Gilford progeria syndrome. *Sci. Transl. Med.* 10:1–13.
109. Atchison, L., H. Zhang, K. Cao, and G.A. Truskey. 2017. A Tissue Engineered Blood Vessel Model of Hutchinson-Gilford Progeria Syndrome Using Human iPSC-derived

- Smooth Muscle Cells. *Sci. Rep.* 7:1–12.
110. Hamczyk, M.R., R. Villa-Bellosta, P. Gonzalo, M.J. Andrés-Manzano, P. Nogales, J.F. Bentzon, C. López-Otín, and V. Andrés. 2018. Vascular smooth muscle–specific progerin expression accelerates atherosclerosis and death in a mouse model of Hutchinson-Gilford progeria syndrome. *Circulation.* 138:266–282.
 111. Hamczyk, M.R., R. Villa-Bellosta, V. Quesada, P. Gonzalo, S. Vidak, R.M. Nevado, M.J. Andrés-Manzano, T. Misteli, C. López-Otín, and V. Andrés. 2019. Progerin accelerates atherosclerosis by inducing endoplasmic reticulum stress in vascular smooth muscle cells. *EMBO Mol. Med.* 11.
 112. Sun, S., W. Qin, X. Tang, Y. Meng, W. Hu, S. Zhang, M. Qian, Z. Liu, X. Cao, Q. Pang, B. Zhao, Z. Wang, Z. Zhou, and B. Liu. 2020. Vascular endothelium–targeted Sirt7 gene therapy rejuvenates blood vessels and extends life span in a Hutchinson-Gilford progeria model. *Sci. Adv.* 6:eaay5556.
 113. Osmanagic-Myers, S., A. Kiss, C. Manakanatas, O. Hamza, F. Sedlmayer, P.L. Szabo, I. Fischer, P. Fichtinger, B.K. Podesser, M. Eriksson, and R. Foisner. 2018. Endothelial progerin expression causes cardiovascular pathology through an impaired mechanoresponse. *J. Clin. Invest.* 129:531.
 114. Danielsson, B.E., K. V. Tieu, K. Bathula, T.J. Armiger, P.S. Vellala, R.E. Taylor, K.N. Dahl, and D.E. Conway. 2020. Lamin microaggregates lead to altered mechanotransmission in progerin-expressing cells. *Nucleus.* 11:194–204.
 115. Stephens, A.D., P.Z. Liu, E.J. Banigan, L.M. Almassalha, V. Backman, S.A. Adam, R.D. Goldman, and J.F. Marko. 2018. Chromatin histone modifications and rigidity affect nuclear morphology independent of lamins. *Mol. Biol. Cell.* 29:220–233.

116. Cao, K., C.D. Blair, D.A. Faddah, J.E. Kieckhaefer, M. Olive, M.R. Erdos, E.G. Nabel, and F.S. Collins. 2011. Progerin and telomere dysfunction collaborate to trigger cellular senescence in normal human fibroblasts. *J. Clin. Invest.* 121:2833–2844.
117. MR, H., V.-B. R, Q. V, G. P, V. S, N. RM, A.-M. MJ, M. T, L.-O. C, and A. V. 2019. Progerin accelerates atherosclerosis by inducing endoplasmic reticulum stress in vascular smooth muscle cells. *EMBO Mol. Med.* 11.
118. Gabriel, D., D.D. Shafry, L.B. Gordon, and K. Djabali. 2017. Intermittent treatment with farnesyltransferase inhibitor and sulforaphane improves cellular homeostasis in Hutchinson- Gilford progeria fibroblasts. *Oncotarget.* 8:64809–64826.
119. Bridger, J.M., and I.R. Kill. 2004. Aging of Hutchinson-Gilford progeria syndrome fibroblasts is characterised by hyperproliferation and increased apoptosis. *Exp. Gerontol.* 39:717–724.
120. Yang, S.H., M.O. Bergo, J.I. Toth, X. Qiao, Y. Hu, S. Sandoval, M. Meta, P. Bendale, M.H. Gelb, S.G. Young, and L.G. Fong. 2005. Blocking protein farnesyltransferase improves nuclear blebbing in mouse fibroblasts with a targeted Hutchinson-Gilford progeria syndrome mutation. *Proc. Natl. Acad. Sci. U. S. A.* 102:10291–10296.
121. Bidault, G., M. Garcia, J. Capeau, R. Morichon, C. Vigouroux, and V. Béréziat. 2020. Progerin Expression Induces Inflammation, Oxidative Stress and Senescence in Human Coronary Endothelial Cells. *Cells.* 9.
122. Atchison, L., N.O. Abutaleb, E. Snyder-Mounts, Y. Gete, A. Ladha, T. Ribar, K. Cao, and G.A. Truskey. 2020. iPSC-Derived Endothelial Cells Affect Vascular Function in a Tissue-Engineered Blood Vessel Model of Hutchinson-Gilford Progeria Syndrome. *Stem Cell Reports.* 14:325–337.

123. Rafieian-Kopaei, M., M. Setorki, M. Douidi, A. Baradaran, and H. Nasri. 2014. Atherosclerosis: Process, Indicators, Risk Factors and New Hopes. *Int. J. Prev. Med.* 5:927.
124. Pitrez, P.R., L. Estronca, L.M. Monteiro, G. Colell, H. Vazão, D. Santinha, K. Harhour, D. Thornton, C. Navarro, A.-L. Egesipe, T. Carvalho, R.L. Dos Santos, N. Lévy, J.C. Smith, J.P. de Magalhães, A. Ori, A. Bernardo, A. De Sandre-Giovannoli, X. Nissan, A. Rosell, and L. Ferreira. 2020. Vulnerability of progeroid smooth muscle cells to biomechanical forces is mediated by MMP13. *Nat. Commun.* 2020 111. 11:1–16.
125. Capell, B.C., M.R. Erdos, J.P. Madigan, J.J. Fiordalisi, R. Varga, K.N. Conneely, L.B. Gordon, C.J. Der, A.D. Cox, and F.S. Collins. 2005. Inhibiting farnesylation of progerin prevents the characteristic nuclear blebbing of Hutchinson-Gilford progeria syndrome. *Proc. Natl. Acad. Sci.* 102:12879–12884.
126. Cho, S., A. Abbas, J. Irianto, I.L. Ivanovska, Y. Xia, M. Tewari, and D.E. Discher. 2018. Progerin phosphorylation in interphase is lower and less mechanosensitive than lamin-a,c in ips-derived mesenchymal stem cells. *Nucleus.* 9:235–250.
127. Dechat, T., T. Shimi, S.A. Adam, A.E. Rusinol, D.A. Andres, H.P. Spielmann, M.S. Sinensky, and R.D. Goldman. 2007. Alterations in mitosis and cell cycle progression caused by a mutant lamin A known to accelerate human aging. *Proc. Natl. Acad. Sci.* 104:4955–4960.
128. Denis, K.B., J.I. Cabe, B.E. Danielsson, K. V. Tieu, C.R. Mayer, and D.E. Conway. 2021. The LINC complex is required for endothelial cell adhesion and adaptation to shear stress and cyclic stretch. <https://doi.org/10.1091/mbc.E20-11-0698>. mbc.E20-11-0698.
129. Harada, T., J. Swift, J. Irianto, J.-W. Shin, K.R. Spinler, A. Athirasala, R. Diegmiller,

- P.C.D.P. Dingal, I.L. Ivanovska, and D.E. Discher. 2014. Nuclear lamin stiffness is a barrier to 3D migration, but softness can limit survival. *J. Cell Biol.* 204:669–682.
130. Deguchi, S., K. Maeda, T. Ohashi, and M. Sato. 2005. Flow-induced hardening of endothelial nucleus as an intracellular stress-bearing organelle. *J. Biomech.* 38:1751–9.
131. Ashapkin, V. V., L.I. Kutueva, S.Y. Kurchashova, and I.I. Kireev. 2019. Are There Common Mechanisms Between the Hutchinson–Gilford Progeria Syndrome and Natural Aging? *Front. Genet.* 10.
132. Goldberg, A.D., C.D. Allis, and E. Bernstein. 2007. Epigenetics: A Landscape Takes Shape. *Cell.* 128:635–638.
133. Chubb, J.R., S. Boyle, P. Perry, and W.A. Bickmore. 2002. Chromatin Motion Is Constrained by Association with Nuclear Compartments in Human Cells. *Curr. Biol.* 12:439–445.
134. Mearini, G., and F.O. Fackelmayer. 2006. Local Chromatin Mobility is Independent of Transcriptional Activity. <http://dx.doi.org/10.4161/cc.5.17.3186>. 5:1989–1995.
135. Dahl, K.N., E.A. Booth-Gauthier, and B. Ladoux. 2010. In the middle of it all: Mutual mechanical regulation between the nucleus and the cytoskeleton. *J. Biomech.* 43:2–8.
136. Fedorova, E., and D. Zink. 2009. Nuclear genome organization: common themes and individual patterns. *Curr. Opin. Genet. Dev.* 19:166–171.
137. Geyer, P.K., M.W. Vitalini, and L.L. Wallrath. 2011. Nuclear organization: taking a position on gene expression. *Curr. Opin. Cell Biol.* 23:354–359.
138. Küpper, K., A. Kölbl, D. Biener, S. Dittrich, J. von Hase, T. Thormeyer, H. Fiegler, N.P. Carter, M.R. Speicher, T. Cremer, and M. Cremer. 2007. Radial chromatin positioning is shaped by local gene density, not by gene expression. *Chromosoma.* 116:285–306.

139. Damodaran, K., S. Venkatachalapathy, F. Alisafaei, A. V. Radhakrishnan, D.S. Jokhun, V.B. Shenoy, and G. V. Shivashankar. 2018. Compressive force induces reversible chromatin condensation and cell geometry–dependent transcriptional response. *Mol. Biol. Cell.* 29:3039–3051.
140. Furusawa, T., M. Rochman, L. Taher, E.K. Dimitriadis, K. Nagashima, S. Anderson, and M. Bustin. 2015. Chromatin decompaction by the nucleosomal binding protein HMGN5 impairs nuclear sturdiness. *Nat. Commun.* 6.
141. Pajerowski, J.D., K.N. Dahl, F.L. Zhong, P.J. Sammak, and D.E. Discher. 2007. Physical plasticity of the nucleus in stem cell differentiation. *Proc. Natl. Acad. Sci. U. S. A.* 104:15619–15624.
142. Spagnol, S.T., T.J. Armiger, and K.N. Dahl. 2016. Mechanobiology of Chromatin and the Nuclear Interior. *Cell. Mol. Bioeng.* 9:268–276.
143. Hahn, C., and M.A. Schwartz. 2009. Mechanotransduction in vascular physiology and atherogenesis. *Nat. Rev. Mol. Cell Biol.* 10:53–62.
144. Illi, B., S. Nanni, A. Scopece, A. Farsetti, P. Biglioli, M.C. Capogrossi, and C. Gaetano. 2003. Shear stress-mediated chromatin remodeling provides molecular basis for flow-dependent regulation of gene expression. *Circ. Res.* 93:155–161.
145. Dunn, J., H. Qiu, S. Kim, D. Jjingo, R. Hoffman, C.W. Kim, I. Jang, D.J. Son, D. Kim, C. Pan, Y. Fan, I.K. Jordan, and H. Jo. 2014. Flow-dependent epigenetic DNA methylation regulates endothelial gene expression and atherosclerosis. *J. Clin. Invest.* 124:3187–3199.
146. Jiang, Y.Z., E. Manduchi, J.M. Jiménez, and P.F. Davies. 2015. Endothelial Epigenetics in Biomechanical Stress: Disturbed Flow-Mediated Epigenomic Plasticity in Vivo and in Vitro. *Arterioscler. Thromb. Vasc. Biol.* 35:1317–1326.

147. Zhou, J., Y.S. Li, K.C. Wang, and S. Chien. 2014. Epigenetic mechanism in regulation of endothelial function by disturbed flow: Induction of DNA hypermethylation by DNMT1. *Cell. Mol. Bioeng.* 7:218–224.
148. Lee, D.Y., and J.J. Chiu. 2019. Atherosclerosis and flow: Roles of epigenetic modulation in vascular endothelium. *J. Biomed. Sci.* 26:1–17.
149. Lee, D.Y., T.E. Lin, C.I. Lee, J. Zhou, Y.H. Huang, P.L. Lee, Y.T. Shih, S. Chien, and J.J. Chiu. 2017. MicroRNA-10a is crucial for endothelial response to different flow patterns via interaction of retinoid acid receptors and histone deacetylases. *Proc. Natl. Acad. Sci. U. S. A.* 114:2072–2077.
150. Lee, D.Y., C.I. Lee, T.E. Lin, S.H. Lim, J. Zhou, Y.C. Tseng, S. Chien, and J.J. Chiu. 2012. Role of histone deacetylases in transcription factor regulation and cell cycle modulation in endothelial cells in response to disturbed flow. *Proc. Natl. Acad. Sci. U. S. A.* 109:1967–1972.
151. Ku, K.H., N. Subramaniam, and P.A. Marsden. 2019. Epigenetic determinants of flow-mediated vascular endothelial gene expression. *Hypertension.* 74:467–476.
152. Chen, W., M. Bacanamwo, and D.G. Harrison. 2008. Activation of p300 Histone Acetyltransferase Activity Is an Early Endothelial Response to Laminar Shear Stress and Is Essential for Stimulation of Endothelial Nitric-oxide Synthase mRNA Transcription. *J. Biol. Chem.* 283:16293–16298.
153. Dunn, J., R. Simmons, S. Thabet, and H. Jo. 2015. The role of epigenetics in the endothelial cell shear stress response and atherosclerosis. *Int. J. Biochem. Cell Biol.* 67:167–176.
154. Booth-Gauthier, E.A., T.A. Alcoser, G. Yang, and K.N. Dahl. 2012. Force-Induced

- Changes in Subnuclear Movement and Rheology. *Biophys. J.* 103:2423–2431.
155. Hampoelz, B., Y. Azou-Gros, R. Fabre, O. Markova, P.H. Puech, and T. Lecuit. 2011. Microtubule-induced nuclear envelope fluctuations control chromatin dynamics in *Drosophila* embryos. *Development.* 138:3377–3386.
156. Iyer, K.V., S. Pulford, A. Mogilner, and G. V. Shivashankar. 2012. Mechanical Activation of Cells Induces Chromatin Remodeling Preceding MKL Nuclear Transport. *Biophys. J.* 103:1416–1428.
157. Denais, C.M., R.M. Gilbert, P. Isermann, A.L. McGregor, M. Te Lindert, B. Weigel, P.M. Davidson, P. Friedl, K. Wolf, and J. Lammerding. 2016. Nuclear envelope rupture and repair during cancer cell migration. *Science (80-.).* 352:353–358.
158. Zink, D., A.H. Fischer, and J.A. Nickerson. 2004. Nuclear structure in cancer cells. *Nat. Rev. Cancer.* 4:677–687.
159. Nava, M.M., Y.A. Miroshnikova, L.C. Biggs, D.B. Whitefield, F. Metge, J. Boucas, H. Vihinen, E. Jokitalo, X. Li, J.M. García Arcos, B. Hoffmann, R. Merkel, C.M. Niessen, K.N. Dahl, and S.A. Wickström. 2020. Heterochromatin-Driven Nuclear Softening Protects the Genome against Mechanical Stress-Induced Damage. *Cell.* 181:800-817.e22.
160. Ko, K.A., K. Fujiwara, S. Krishnan, and J.I. Abe. 2017. En face preparation of mouse blood vessels. *J. Vis. Exp.* 2017:e55460.
161. Yaron, P.N., B.D. Holt, P.A. Short, M. Lösche, M.F. Islam, and K.N. Dahl. 2011. Single wall carbon nanotubes enter cells by endocytosis and not membrane penetration. *J. Nanobiotechnology.* 9:1–15.
162. Cunningham, K.S., and A.I. Gotlieb. 2004. The role of shear stress in the pathogenesis of atherosclerosis. *Lab. Investig. 2005 851.* 85:9–23.

163. Berger, L., T. Kolben, S. Meister, T.M. Kolben, E. Schmoeckel, D. Mayr, S. Mahner, U. Jeschke, N. Ditsch, and S. Beyer. 2020. Expression of H3K4me3 and H3K9ac in breast cancer. *J. Cancer Res. Clin. Oncol.* 146:2017–2027.
164. Igolkina, A.A., A. Zinkevich, K.O. Karandasheva, A.A. Popov, M. V. Selifanova, D. Nikolaeva, V. Tkachev, D. Penzar, D.M. Nikitin, and A. Buzdin. 2019. H3K4me3, H3K9ac, H3K27ac, H3K27me3 and H3K9me3 Histone Tags Suggest Distinct Regulatory Evolution of Open and Condensed Chromatin Landmarks. *Cells.* 8.
165. Dunn, J., S. Thabet, and H. Jo. 2015. Flow-dependent epigenetic DNA methylation in endothelial gene expression and atherosclerosis. *Arterioscler. Thromb. Vasc. Biol.* 35:1562–1569.
166. Suo, J., D.E. Ferrara, D. Sorescu, R.E. Guldberg, W.R. Taylor, and D.P. Giddens. 2007. Hemodynamic shear stresses in mouse aortas: implications for atherogenesis. *Arterioscler. Thromb. Vasc. Biol.* 27:346–351.
167. Fejes Tóth, K., T.A. Knoch, M. Wachsmuth, M. Frank-Stöhr, M. Stöhr, C.P. Bacher, G. Müller, and K. Rippe. 2004. Trichostatin A-induced histone acetylation causes decondensation of interphase chromatin. *J. Cell Sci.* 117:4277–4287.
168. Yoshida, M., M. Kijima, M. Akita, and T. Beppu. 1990. Potent and specific inhibition of mammalian histone deacetylase both in vivo and in vitro by trichostatin A. *J. Biol. Chem.* 265:17174–17179.
169. Luo, X., Y. Liu, S. Kubicek, J. Myllyharju, A. Tumber, S. Ng, K.H. Che, J. Podoll, T.D. Heightman, U. Oppermann, S.L. Schreiber, and X. Wang. 2011. A selective inhibitor and probe of the cellular functions of jumonji C domain-containing histone demethylases. *J. Am. Chem. Soc.* 133:9451–9456.

170. Spagnol, S.T., and K.N. Dahl. 2016. Spatially resolved quantification of chromatin condensation through differential local rheology in cell nuclei fluorescence lifetime imaging. *PLoS One*. 11.
171. Lin, K., P.P. Hsu, B.P. Chen, S. Yuan, S. Usami, J.Y.J. Shyy, Y.S. Li, and S. Chien. 2000. Molecular mechanism of endothelial growth arrest by laminar shear stress. *Proc. Natl. Acad. Sci.* 97:9385–9389.
172. Zhou, J., Y.S. Li, K.C. Wang, and S. Chien. 2014. Epigenetic mechanism in regulation of endothelial function by disturbed flow: Induction of DNA hypermethylation by DNMT1. *Cell. Mol. Bioeng.* 7:218–224.
173. Jiang, Y., and J.Y. Ji. 2018. Expression of Nuclear Lamin Proteins in Endothelial Cells is Sensitive to Cell Passage and Fluid Shear Stress. *Cell. Mol. Bioeng.* 11:53–64.
174. Danielsson, B.E., H.C. Peters, K. Bathula, L.M. Spear, N.A. Noll, K.N. Dahl, and D.E. Conway. 2022. Progerin-expressing endothelial cells are unable to adapt to shear stress. *Biophys. J.*
175. Krause, M., J. Te Riet, and K. Wolf. 2013. Probing the compressibility of tumor cell nuclei by combined atomic force–confocal microscopy. *Phys. Biol.* 10:065002.
176. Miroshnikova, Y.A., and S.A. Wickström. 2022. Mechanical Forces in Nuclear Organization. *Cold Spring Harb. Perspect. Biol.* 14.
177. Stephens, A.D. 2020. Chromatin rigidity provides mechanical and genome protection. *Mutat. Res. - Fundam. Mol. Mech. Mutagen.* 821:111712.
178. Roca-Cusachs, P., V. Conte, and X. Trepat. 2017. Quantifying forces in cell biology. *Nat. Cell Biol.* 2017 197. 19:742–751.
179. Tajik, A., Y. Zhang, F. Wei, J. Sun, Q. Jia, W. Zhou, R. Singh, N. Khanna, A.S. Belmont,

- and N. Wang. 2016. Transcription upregulation via force-induced direct stretching of chromatin. *Nat. Mater.* 15:1287–1296.
180. Dechat, T., K. Pflieger, K. Sengupta, T. Shimi, D.K. Shumaker, L. Solimando, and R.D. Goldman. 2008. Nuclear lamins: major factors in the structural organization and function of the nucleus and chromatin. *Genes Dev.* 22:832–853.
181. Naetar, N., S. Ferraioli, and R. Foisner. 2017. Lamins in the nuclear interior - life outside the lamina. *J. Cell Sci.* 130:2087–2096.
182. Sapra, K.T., Z. Qin, A. Dubrovsky-Gaup, U. Aebi, D.J. Müller, M.J. Buehler, and O. Medalia. 2020. Nonlinear mechanics of lamin filaments and the meshwork topology build an emergent nuclear lamina. *Nat. Commun.* 2020 111. 11:1–14.
183. Grashoff, C., B.D. Hoffman, M.D. Brenner, R. Zhou, M. Parsons, M.T. Yang, M.A. McLean, S.G. Sligar, C.S. Chen, T. Ha, and M.A. Schwartz. 2010. Measuring mechanical tension across vinculin reveals regulation of focal adhesion dynamics. *Nature.* 466:263–266.
184. Jullien, D., J. Vignard, Y. Fedor, N. Béry, A. Olichon, M. Crozatier, M. Erard, H. Cassard, B. Ducommun, B. Salles, and G. Mirey. 2016. Chromatibody, a novel non-invasive molecular tool to explore and manipulate chromatin in living cells. *J. Cell Sci.* 129:2673–2683.
185. Zhang, Q., V. Narayanan, K.L. Mui, C.S. O’Bryan, R.H. Anderson, B. KC, J.I. Cabe, K.B. Denis, S. Antoku, K.J. Roux, R.B. Dickinson, T.E. Angelini, G.G. Gundersen, D.E. Conway, and T.P. Lele. 2019. Mechanical Stabilization of the Glandular Acinus by Linker of Nucleoskeleton and Cytoskeleton Complex. *Curr. Biol.* 29:2826-2839.e4.
186. Nelles, D.A., M.Y. Fang, M.R. O’Connell, J.L. Xu, S.J. Markmiller, J.A. Doudna, and

- G.W. Yeo. 2016. Programmable RNA Tracking in Live Cells with CRISPR/Cas9. *Cell*. 165:488–496.
187. Schindelin, J., I. Arganda-Carreras, E. Frise, V. Kaynig, M. Longair, T. Pietzsch, S. Preibisch, C. Rueden, S. Saalfeld, B. Schmid, J.Y. Tinevez, D.J. White, V. Hartenstein, K. Eliceiri, P. Tomancak, and A. Cardona. 2012. Fiji: an open-source platform for biological-image analysis. *Nat. Methods* 2012 97. 9:676–682.
188. Thévenaz, P., U.E. Ruttimann, and M. Unser. 1998. A pyramid approach to subpixel registration based on intensity. *IEEE Trans. Image Process.* 7:27–41.
189. Phair, R.D., and T. Misteli. 2000. High mobility of proteins in the mammalian cell nucleus. *Nat.* 2000 4046778. 404:604–609.
190. Resasco, D.C., F. Gao, F. Morgan, I.L. Novak, J.C. Schaff, and B.M. Slepchenko. 2012. Virtual Cell: computational tools for modeling in cell biology. *Wiley Interdiscip. Rev. Syst. Biol. Med.* 4:129.
191. Schaff, J., C.C. Fink, B. Slepchenko, J.H. Carson, and L.M. Loew. 1997. A general computational framework for modeling cellular structure and function. *Biophys. J.* 73:1135.
192. Arsenovic, P.T., C.R. Mayer, and D.E. Conway. 2017. SensorFRET: A Standardless Approach to Measuring Pixel-based Spectral Bleed-through and FRET Efficiency using Spectral Imaging. *Sci. Rep.* 7:1–15.
193. Roszik, J., D. Lisboa, J. Szöllosi, and G. Vereb. 2009. Evaluation of intensity-based ratiometric FRET in image cytometry—Approaches and a software solution. *Cytom. Part A.* 75A:761–767.